Fully relativistic Green's functions method

Vishina, Alena

Awarding institution:
King's College London

Fully relativistic Green's functions method

Alena Vishina

Department of Physics

King's College London

A thesis submitted in partial fulfilment

of the requirements for the degree of

Doctor of Philosophy in Physics

August 2017

Acknowledgements

First, I would like to thank Prof. Mark van Schilfgaarde for guiding me throughout my PhD, supplying new ideas, sharing with me his enormous experience in the field of condensed matter physics, and helping me on every occasion when I got stuck. This thesis would not have been possible without him.

Second, I am grateful to King's College London for giving me the opportunity to work in this great educational institution. My heartfelt thanks go to all the members of staff who helped me one way or another.

I want to say a special 'thank you' to Pooya Azarhoosh, who, sitting next to me for four years, had to listen to my 'segmentation fault' complaints thousands of times. I am extremely grateful to Dimitar Pashov who always knows how it works and how to fix it, Marcello (Marce) Caio who never runs out of sarcasm, Thomas Helfer for keeping me company at the department on Sundays. I express my gratitude to all the PhD students and postdocs for making my life at King's so much easier: Lorenzo Sponza, Paolo Pisanti, Krzysiek (Krys) Bozek, Marco de Cesare, Dan Allen, Chiara Paris, Alix Le Marois, Yurema Teijeiro Gonzalez, Fedor Šimkovic, Soraya Caixeiro, Ankur Chaurasia, Max Fulford, Mateusz Bieniek, Federico Bianchini, Marco Caccin, Katy Clough, James Cook, Scott McKechnie, Leonardo Ruiz, Ekaterina Moskvitch, and Mattia Fiorentini.

I would never have got through my studies without the amazing team of our physics department office: Julia Kilpatrick, Megan Grace-Hughes, Rowena

Peake, Bonnie Parker, James French, Laurie van Schilfgaarde, and especially, Dr Paul Le Long with his magnificent sense of humour.

I am extremely grateful to Prof. Mark Green for supporting and cheering me up in my search for a postdoc. I remain indebted to Dr Eva Philippaki, Dr Shahriar Sajjadi, Dr Bozidar Butorac, Prof. Samjid Mannan, Christina Missirli, and David Parker for making my teaching duties so much more enjoyable.

Abstract

Relativistic effects, such as spin-orbit coupling, are important in heavier elements and trigger some interesting phenomena such as magnetic anisotropy, orbital magnetization, etc. For a careful treatment of these effects, we need to solve the Dirac equation. However, it is not a trivial problem and requires the use of some special techniques due to the complicated nature of the equation. We describe the implementation of this task and its effect on the results of electronic structure calculations, including magnetic susceptibilities and exchange interactions, computed relativistically.

The coherent potential approximation (CPA) is a convenient tool for treating alloys. It is applied here to $(Ni_{1-x}Fe_x)_{1-y}Z_y$ (Z=Cu, Cr, Mn, and Rh) alloys to calculate their magnetization, Curie temperatures, and other properties. Interest in these materials is due to the growing need for weak magnets with low-saturation magnetization and reduced Curie temperatures for some applications in microelectronics.

Table of contents

List of figures

List of tables

Abbreviations

ARPES – Angle-resolved photoemission spectroscopy

BZ – Brillouin zone

CPA – Coherent potential approximation

dHvA – de Haas-van Alphen

DMFT – Dynamical-mean field theory

FL – Fermi liquid and Fermi level

GF – Green's functions

KS – Kohn-Sham

KKR – Korringa-Kohn-Rostoker

LDA – Local density approximation

LMTO – Linear muffin tin orbital

MFP – Mean free path

MST – Multiple-scattering theory

QP – Quasiparticle

SP – Slater-Pauling

Preface

The thesis is divided into separate parts. Chapter 1 introduces the main methods and approximation of electronic structure calculations that are used in the following chapters, including the definition and applications of Green's functions (GF) mentioned throughout the thesis.

Chapter 2 describes the implementation of fully relativistic LMTO formalism based on the solution of the Dirac equation, important for treating heavier elements, magnetic anisotropy, spin-orbit coupling, etc. The chapter gives a brief insight into the various methods proposed by different authors and explains the method used to solve the Dirac equation for core and valence electron states within linear muffin tin orbital (LMTO) formalism. This chapter also presents the comparison between the fully relativistic and scalar-relativistic results for several materials.

The application of Green's function to alloys in the framework of coherent potential approximation (CPA) is presented in Chapter 3. The magnetization, Curie temperatures, spin mean free paths, and other properties of $(Ni_{1-x}Fe_x)_{1-y}Z_y$ (Z = *Cu, Cr, Mn, Rh*) alloys are calculated and compared to recent experimental results.

Chapter 4 presents the method of calculating the susceptibility and magnetic exchange interactions in the non-collinear case when the fully-

relativistic treatment is applied. The chapter compares between the values obtained in both relativistic and non-relativistic cases.

Chapter 5 focuses on calculating the spin-wave lifetime. The method proposed is also applied to the alloys introduced in Chapter 3.

Finally, Chapter 6 is a smaller section focused on the final-stage scattering effects in angle-resolved photoemission spectroscopy (ARPES). It compares the ARPES data with the results of quasiparticle self-consistent GW (QSGW) calculations for Fe, such as the Fermi surface and cyclotron masses. The method of taking those final effects into account is presented and then applied to correct the calculated band structure.

The conclusion summarizes the results and presents some ideas about further applications of the methods presented in the thesis.

Chapter 1. Introduction

Electronic structure calculations

Electrons and nuclei, deemed as building blocks of matter define the nature and properties of all materials. Electronic structure theory describes the state and motion of electrons around the nucleus; it is essential for understanding the materials and their electrical, optical, and magnetic properties. Many analytical and computational approaches have been developed over almost a century to accurately describe an interacting system of many electrons.

Ab initio calculations, or calculations 'from the first principles', are developed to predict the physical properties of materials, without using any experimental or empirical input, from the laws of quantum mechanics and the knowledge of constituent atoms [1,2]. Nowadays, *ab initio* methods are used in physics, chemistry, and other fields for calculating not only the properties of bulk materials, but also surface phenomena, catalysis, chemical reactions, molecular geometries and energies, molecular dynamics, defects, clusters, among others, in a broad range of materials. Electronic structure calculations that use Schrödinger's equation with the necessary approximations and do not include fitting the model to experimental data are called *ab initio* approach.

The Hamiltonian of a system of electrons and nuclei has the following form:

$$H = -\frac{\hbar^2}{2m_e}\sum_i \nabla_i^2 - \sum_{i,I}\frac{Z_I e}{|\mathbf{r}_i - \mathbf{R}_I|} + \frac{1}{2}\sum_{i\neq j}\frac{e^2}{|\mathbf{r}_i - \mathbf{r}_j|} - \frac{\hbar^2}{2M_I}\sum_I \nabla_I^2 + \frac{1}{2}\sum_{I\neq J}\frac{Z_I Z_J}{|\mathbf{R}_I - \mathbf{R}_J|}; \quad (1.1)$$

where the lower case ($i, j, \mathbf{r}$) refers to electrons and upper case ($I, J, \mathbf{R}$) denotes nuclei; Z and M are the charge and mass of the nuclei respectively. The Hamiltonian consists of the electrons' and nuclei's kinetic energy, electron-nuclei (second term), electron-electron (third term), and nuclei-nuclei (fifth term) interactions. The kinetic energy of the nuclei is usually neglected due to their comparatively large masses M_I; which is known as the Born-Oppenheimer approximation [11]. It assumes that the nuclei and electrons can be considered separately - this, in mathematical terms, means that the wave function can be written as a product of its electronic and nuclear components. In this way the electronic Schrödinger equation is solved for the wave function, depending only on electrons, with the nuclei fixed in a certain configuration. If the effects of nuclear motion are to be studied, the Schrödinger equation for the nuclei needs to be solved as the second step.

For a non-relativistic case, the next step after writing down the Hamiltonian would be to solve the following Schrödinger equation

$$i\hbar\frac{d\Psi\left(\{\mathbf{r}_i\};t\right)}{dt} = H\Psi\left(\{\mathbf{r}_i\};t\right) \quad (1.2)$$

in order to find the many-body wave function $\Psi\left(\{\mathbf{r}_i\};t\right)$ and the eigenstates of the equation. Here the many-body function $\Psi\left(\{\mathbf{r}_i\};t\right) \equiv \Psi\left(\mathbf{r}_1, \mathbf{r}_2, ..., \mathbf{r}_N; t\right)$ and the

spin is assumed to be included in the coordinate. Then for any observable, the expectation value of its operator can be as [12]:

$$\left\langle \hat{O} \right\rangle = \frac{\left\langle \Psi \middle| \hat{O} \middle| \Psi \right\rangle}{\left\langle \Psi \middle| \Psi \right\rangle}. \tag{1.3}$$

For example, the density of particles can be found as the expectation value of the density operator: $\hat{n}(\mathbf{r}) = \sum_i \delta(\mathbf{r} - \mathbf{r}_i)$ [7]. The total energy of a system is the expectation value of its Hamiltonian. The state with the lowest energy is called the ground state.

Unfortunately, the huge number of particles that must be considered in condensed matter physics (which is of the order of Avogadro's number) does not allow us to solve this equation directly.

The first quantitative calculations of electronic structure were developed in the 1930s by D. R. Hartree and V. Fock [1,4], and by Wigner and Seitz [5,6]. Hartree saw that an exact analytic solution of Schrödinger's equation for any atom with more than one electron is impossible because of the electron-electron repulsion term, which makes precludes factorization of the many-body wave function into products of one-particle functions.

In the last decades of the 20th century, a number of methods were developed for computational calculation of the electronic structure. The most common among these are density functional theory [7], quantum Monte-Carlo methods [8], many-body perturbation methods [9], and dynamical mean-field theory [10].

In this chapter, we will give some general background and the main building stones necessary for understanding the density functional *ab intio* calculations.

Density functional theory

The techniques used further in the thesis are based on density functional theory (DFT). The objective of DFT is to determine the ground state properties of an interacting many-body system, and its most important statement is that all ground state properties of the system are functionals of the ground state density $n_0(r)$. Hence, $n_0(r)$ provides all the necessary information to describe the many-body wavefunctions for the ground state. DFT was first formulated by P. Hohenberg and W. Kohn in 1964 [16], and then extended to finite temperatures by N. D. Mermin in 1965 [17]. DFT is now considered one of the main tools for the quantum mechanical simulation of periodic systems, and a number of books and reviews give a good detailed description of it [13-15].

To describe the basic concepts of DFT, one should start with a Hamiltonian of the system of electrons in the given external potential $V_{ext}(\mathbf{r})$:

$$H = -\frac{\hbar^2}{2m_e}\sum_i \nabla_i^2 + \frac{1}{2}\sum_{i\neq j}\frac{e^2}{|\mathbf{r}_i - \mathbf{r}_j|} + \sum_i V_{ext}(\mathbf{r}_i). \qquad (1.4)$$

The first term here is the electron kinetic energy, the second represents electron-electron interaction, while the third one includes the external potential electrons move in.

DFT is based on two theorems [16]. The first one states that for any system of interacting particles in the external potential $V_{ext}(\mathbf{r})$, the potential is determined uniquely (except for a constant) by the ground state particle density $n_0(\mathbf{r})$ of the system [7]. Since $V_{ext}(\mathbf{r})$ determines the Hamiltonian and hence the many-body wavefunctions, all the physical properties of the system can be obtained from its ground state density, $n_0(\mathbf{r})$.

According to the second theorem, there exists a universal functional $E[n]$ of the charge density $n(\mathbf{r})$ which can be defined for any external potential $V_{ext}(\mathbf{r})$. This functional attains its global minimum if and only if the charge density is the ground state density $n_0(\mathbf{r})$. It means that $E[n]$ alone is sufficient to determine the exact ground state energy and density [7]. Hence, the idea behind the method is described in the following: $E[n]$ can be determined for any density, the minimization of the functional gives the exact ground state density and energy of the interacting many-body system. Unfortunately, even though DFT provides the exact form of the density, it does not provide a way to extract any general set of properties just from the density itself. The properties of the excited states should also be determined in some other way.

Another difficulty is that DFT does not provide any method for constructing the functionals, so it would be practically useless if not for the ansatz made by Kohn and Sham [18]. It replaces the difficult interacting many-body system by a simplified one, assuming that the ground state density of the original

interacting system is equal to the density of some chosen auxiliary non-interacting system that, unlike the interacting system, can be solved.

Following Kohn and Sham [18], the auxiliary Hamiltonian is built in such a way that it consists of a kinetic part and the effective local potential $V_{eff}(\sigma,\mathbf{r})$. The density of such a system is the sum of the squares of the orbitals for each spin $n(\mathbf{r}) = \sum_{\sigma}\sum_{i=1}^{N^{\sigma}} \left|\psi_i^{\sigma}(\mathbf{r})\right|^2$. The ground state energy functional in the Kohn-Sham approach has the following form:

$$E_{KS} = T_S[n] + \int d\mathbf{r} V_{ext}(\mathbf{r}) n(\mathbf{r}) + E_{Hartree}[n] + E_{II} + E_{ex}[n], \tag{1.5}$$

where V_{ext} is the external potential due to the nuclei and other external fields, $T_S[n]$ is the kinetic energy of the non-interacting electrons that possess the same density as the real interacting system, E_{II} is the interaction between nuclei, and

$$E_{Hartree}[n] = \frac{1}{2}\int d^3r d^3r' \frac{n(\mathbf{r})n(\mathbf{r}')}{|\mathbf{r}-\mathbf{r}'|} \tag{1.6}$$

is the Coulomb electronic repulsion.

All exchange and correlation many-body effects are grouped into the exchange-correlation energy E_{ex}.

The problem of solving the Kohn-Sham system can be approached as the problem of minimization with respect to the density $n(\mathbf{r},\sigma)$. Since the kinetic term can be explicitly expressed as a functional of the orbitals

$T_s = 1/2 \sum_{\sigma} \sum_{i=1}^{N^\sigma} \int d^3 r \left| \nabla \psi_i^\sigma(\mathbf{r}) \right|^2$, while all other terms are the functionals of the density, using the chain rule one can obtain the variation equation [7]

$$\frac{\delta E_{KS}}{\delta \psi_i^{\sigma'}(\mathbf{r})} = \frac{\delta T_s}{\delta \psi_i^{\sigma'}(\mathbf{r})} + \left[\frac{\delta E_{ext}}{\delta n(\mathbf{r},\sigma)} + \frac{\delta E_{Hartree}}{\delta n(\mathbf{r},\sigma)} + \frac{\delta E_{xc}}{\delta n(\mathbf{r},\sigma)} \right] \frac{\delta n(\mathbf{r},\sigma)}{\delta \psi_i^{\sigma'}(\mathbf{r})} = 0.$$

Expressions for the kinetic term and the density give $\delta T_s / \delta \psi_i^\sigma(\mathbf{r}) = -1/2 \nabla^2 \psi_i^\sigma(\mathbf{r})$ and $\delta n^\sigma(\mathbf{r}) / \delta \psi_i^\sigma(\mathbf{r}) = \psi_i^\sigma(\mathbf{r})$. Hence, using the Lagrange multiplier method for handling the constrains [7], the minimization for a given number of particles leads to a system of Kohn-Sham Schrödinger-like equations of the following form:

$$\left(H_{KS}^\sigma - \varepsilon_i^\sigma \right) \psi_i^\sigma(\mathbf{r}) = 0, \tag{1.7}$$

with

$$\begin{aligned} H_{KS}^\sigma &= -\frac{1}{2}\nabla^2 + V_{KS}^\sigma(\mathbf{r}), \\ V_{KS}^\sigma(\mathbf{r}) &= V_{ext}(\mathbf{r}) + \frac{\delta E_{Hartree}}{\delta n(\mathbf{r},\sigma)} + \frac{\delta E_{ex}}{\delta n(\mathbf{r},\sigma)} = V_{ext}(\mathbf{r}) + V_{Hartree}(\mathbf{r}) + V_{xc}^\sigma(\mathbf{r}). \end{aligned} \tag{1.8}$$

Here ε_i are the eigenvalues and H_{KS} is the effective Kohn-Sham Hamiltonian. The Hamiltonian consists of the usual kinetic operator and an effective local potential, $V_{KS}^\sigma(\mathbf{r})$, acting on an electron of spin σ at point **r**. The total energy is given by (1.5). These equations describe a system of non-interacting particles in an external potential. The equations are independent of the form of E_{ex} and lead to the ground state density and the energy of the interacting system.

Since the effective potential V_{KS}^{σ} depends on the charge density, the system must be solved self-consistently. The actual numerical calculation comprises several steps, starting with the initial guess for the density and then calculating the effective potential, thereby solving the Kohn-Sham equation to obtain the wavefunctions and the new electron density. This procedure is repeated with the new density obtained until the self-consistent solution is reached (the output and input densities are the same to a certain chosen error). So, the iterative procedure looks like $V_i \to n_i \to V_{i+1} \to n_{i+1} \to \ldots$ and can be schematically drawn as Fig. 1 [7].

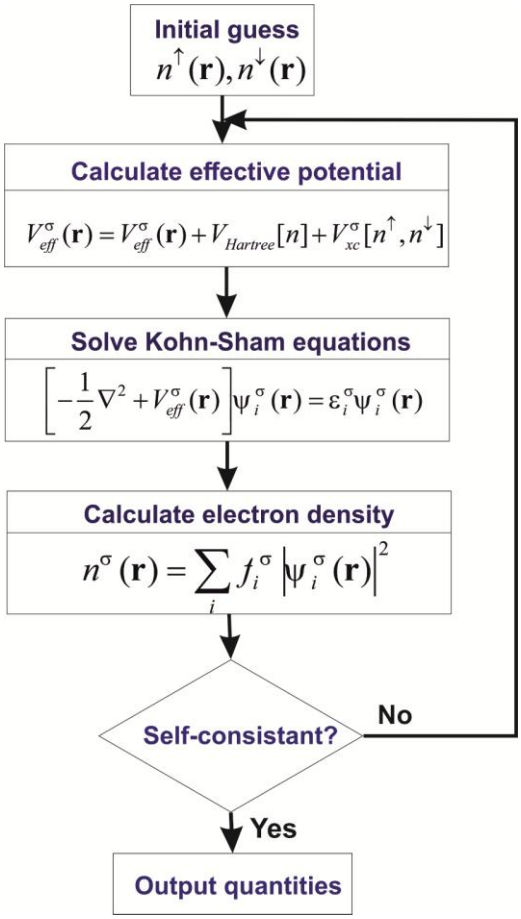

Fig. 1 A scheme of the self-consistent loop for solving Kohn–Sham equations [7]

Approximations in density functional theory

To solve the problem self-consistently, the exchange-correlation potential E_{ex} needs to be defined first, which can only be done approximately. The lLocal density approximation (LDA) is one of the most generally used methods in this regard.

LDA was introduced by Kohn and Sham [18] in their seminal paper, where solids were considered in the limit of homogeneous electron gas. In this approximation, the exchange and correlation energy is calculated as an integral over all space and the exchange-correlation energy at each point is replaced by the same of the homogeneous electron gas with the same density:

$$E_{xc}^{LSDA}\left[n^{\uparrow},n^{\downarrow}\right]=\int d^{3}rn(\mathbf{r})\varepsilon_{xc}^{\hom}\left(n^{\uparrow}(\mathbf{r}),n^{\downarrow}(\mathbf{r})\right). \tag{1.9}$$

Then, the only information needed is the exchange and the correlation energy of the homogeneous electron gas adding up to $\varepsilon_{xc}^{\hom}$. The first one is known in the analytical form:

$$\varepsilon_{x}[n(\mathbf{r})]=-\frac{3}{4}\left(\frac{3}{\pi}\right)^{\frac{1}{3}}n(\mathbf{r});$$

The values for the second have been calculated with the Monte-Carlo methods [7,68] and then interpolated to provide an analytical form [56,57].

The effective potential in LDA, therefore, takes the following form:

$$V_{eff}(\mathbf{r})=V_{ext}(\mathbf{r})+e^{2}\int dr'\frac{n(r')}{\left|r-r'\right|}+\varepsilon_{xc}^{\hom}(n(\mathbf{r})).$$

The procedure is exact if the density $n(\mathbf{r})$ is constant and works well while it varies slowly on the scale of the Fermi wavelength. It has been shown that for a large number of problems, including atoms, molecules, and bulk solids, even where the charge density is rapidly varying, LDA produces good results and is rather simple to implement [58]. It is known, however, that it tends to underestimate atomic ground state energies and ionization energies, and that it overestimates the binding energies [59]. Hence, there have been attempts to move beyond LDA.

To improve on the LDA, some kind of non-local exchange-correlation potential is required. The first step in this direction is the generalized gradient approximation (GGA) that parameterizes the functional using not only the charge density *n* but also its gradient [60]. By adding successively higher-order gradients, the gradient expansion is meant to correct the results of LDA when the density varies more and more rapidly. For many materials, GGA improves the LDA over-binding. However, both GGA and LDA are known to underestimate the band gap of semiconductors and inaccurately describe the band structure of strongly correlated materials.

Linear muffin tin orbital approximation

Augmented plane waves and muffin tins. Augmented-wave methods are based on the separation of the physical space into two parts: the spheres centered at the atoms and interstitial areas between them. When introduced, this kind of

potential was approximated to be spherically symmetric within the spheres and constant in the interstitial region:

$$V_{KS}(r) = \begin{cases} V_{KS}(r) & \text{inside the spheres} \\ V_0 & \text{interstitial region} \end{cases}.$$

This form of the potential is known as 'muffin-tin potential' and the approximation is called atomic-sphere approximation (ASA). It is especially useful for close-packed structures and allows the reduction of DFT equations to simpler forms. However, it is not sufficient for open structures or systems with arbitrary geometry [70]. The original approach is the augmented plane wave (APW) method suggested by Slater in 1937 [69].

The division of space in muffin-tin spheres does not put any restriction on the geometry of the system – it is a matter of computational convenience. The radii of muffin-tins are freely chosen parameters. However, if the basis set outside and inside the spheres is chosen wisely, the total energy is insensitive to the choice.

The eigenstates of the independent-particle Schrödinger-like equation, such as the Kohn-Sham equations, satisfy (1.7). In a solid, it is usually convenient to require the states to obey periodic boundary conditions in the large volume Ω. Since any periodic function can be expanded in the complete set of Fourier components, the eigenfunction can be written as an expansion in the basis set of orthonormal plane waves:

$$\psi_i(\mathbf{r}) = \sum_q c_{i,q} \exp(i\mathbf{q}\cdot\mathbf{r}),$$

where $c_{i,q}$ are the expansion coefficients and q is the wave number.

In the augmented functions methods, the basis set is constructed in such a way that the smoothly varying parts of the wavefunction (in the interstitial region) are represented by plane waves or other smoothly varying functions, while the rapidly varying parts in the spheres are represented as radial functions times spherical harmonics. In this way, the problem of solving the equations becomes the problem of matching the functions at the sphere boundary.

The wavefunctions can be represented in terms of spherical harmonics around the atoms (since the problem is 'spherical' [71,72,73]) and the plane waves in between. Each Bloch function $\psi_{i,k}(\mathbf{r})$ is expanded in a set of basis functions labelled by the reciprocal lattice vectors $\mathbf{G_m}$:

$$\psi_{i,k}(\mathbf{r}) = \sum_m c_{i,m}(\mathbf{k})\chi^{APW}_{k+G_m}(\mathbf{r}), \tag{1.10}$$

where $m = 1, 2, \ldots$ and

$$\chi^{APW}_{\mathbf{k}+\mathbf{G_m}}(\mathbf{r}) = \begin{cases} \exp\left(i(\mathbf{k}+\mathbf{G_m})\cdot\mathbf{r}\right), & r > S \\ \sum_{LS} C_{LS}(\mathbf{k}+\mathbf{G_m}) i^l Y_L(\hat{r})\psi_{ls}(\varepsilon, r), & r < S \end{cases}. \tag{1.11}$$

$\psi_{ls}(\varepsilon, r)$ is a solution of the radial Schrödinger equation at energy ε, S is the boundary of the spherical potential [7]

$$\left[\frac{\hbar^2}{2m_e}\left(-\frac{d^2}{dr^2} + \frac{l(l+1)}{r^2}\right) + V_s(r) - \varepsilon\right] r\psi_{ls}(r) = 0. \tag{1.12}$$

The coefficients $C_{LS}(\mathbf{k}+\mathbf{G_m})$ are obtained in such a way that the wavefunctions match at the muffin-tin spheres.

Spherical harmonics ($Y_l^m(\theta,\varphi)$ and $Y_l^m(\mathbf{r})$) are an infinite set of harmonic functions defined on the 2D space of surface of a sphere. When a differential equation has spherical symmetry, as in our case (assuming that the potential is spherically symmetric), it is easier to solve it in spherical coordinates.

In modern times, the MT potential is used to construct the basis set, but the potential to enter the Hamiltonian is not assumed to be spherical. The same is true with linear muffin tin orbital methods, excepting those that use the atomic spheres approximation.

The disadvantage of augmentation is that it leads to non-linear equations; hence linearized methods, such as the Korringa, Kohn, and Rostocker (KKR) method (which will be described further) or a muffin-tin orbital (MTO) approach, which reformulates the KKR, are often used.

Muffin-tin orbitals. Muffin-tin orbitals (MTO) form a basis of localized augmented orbitals introduced by O. K. Andersen in 1971 [19]. MTO is constructed as a single atomic sphere with flat potential outside [7]. Initially, these functions were constructed as atomic-like and can be enumerated with the angular quantum numbers *l* and *m*. Inside the muffin-tin sphere the basis function χ_L^{MTO} $(L=\{l,m\})$ is constructed of an angular part, expressed by the spherical harmonic Y_l^m and the radial part ψ_l, obtained by solving the radial Schrödinger equation (1.12) at a given energy, ε. If the potential is flat in the interstitial region, the radial functions there are solutions of the radial Helmholtz equation

$$\left[\left(\frac{d^2}{dr^2}-\frac{l(l+1)}{r^2}\right)-\kappa^2\right]rf_l(r)=0,$$

where $\kappa^2 \equiv \frac{2m_e}{\hbar^2}(\varepsilon - V_0)$. These solutions are spherical Bessel functions $j_l(\kappa r)$ and spherical Neumann functions $n_l(\kappa r)$ [19]. In this way, the functions inside and outside the muffin-tin spheres are defined separately with respect to two parameters, namely ε and κ. In KKR formalism, the matching conditions are applied at the muffin-tin boundaries between the wavefunction ψ_l and the asymptotic forms [29,30]

$$\begin{cases} -j_l(\kappa r) + \tan\eta_l(\varepsilon) n_l(\kappa r) & \kappa^2 > 0 \\ -j_l(\kappa r) + \tan\eta_l(\varepsilon) h_l(\kappa r) & \kappa^2 < 0 \end{cases};$$

here the phase shifts η_l are related to the scattering due to the potential, while $h_l = n_l - ij_l$ are spherical Hankel functions of the first kind [70]. However, since for the negative energies Bessel functions are unbounded and the orbital cannot be normalized, the solution is obtained by removing the Bessel functions inside and outside the muffin-tins. Hence, the localized basis functions continuous in value and slope at the sphere boundary are constructed in the following way [20]

$$\chi_L^{MTO}(\varepsilon, \kappa, \mathbf{r}) = i^l Y_L(\hat{r}) \begin{cases} \psi_l(\varepsilon, \mathbf{r}) + \kappa \cot\left(\eta_l(\varepsilon)\right) j_l(\kappa r), & r < S \\ \kappa n_l(\kappa r), & r > S \end{cases}, \qquad (1.13)$$

where $Y_L(\hat{r}) \equiv Y_l^m(\hat{r})$ are the spherical harmonics and S is the muffin-tin radius. So, each MTO basis function is well-defined both inside and outside the sphere. Later in this chapter we will explain how the neighbouring atoms are considered for each sphere and how they affect all the parameters. The part of the muffin-tin orbitals (localized basis functions) inside the muffin-tins is no longer radial as it has been modified by the 'tails' from the neighbouring atoms.

The main disadvantage of the MTO method is that the orbitals depend on the energy; the matching conditions, therefore, must be satisfied separately for each eigenstate at its eigenenergy and the application of the variational method would lead to the non-linear equations. To solve this problem, Andersen's linearization technique is used [22] which leads to the linear muffin-tin orbitals (LMTO) method. The differences between LMTO and MTO are: 1) inside the sphere, where a given LMTO is centred, the radial wavefunction is $\psi_l(\varepsilon,r)=\psi_l(E_\nu,r)+(\varepsilon-E_\nu)\dot{\psi}_l(E_\nu,r)$, where $\dot{\psi}_l$ denotes the first derivative with respect to *E*; and 2) the tail in other spheres is replaced by a combination of $\dot{\psi}_l(E_\nu,r)$ [7]. The localized basis functions here are constructed as:

$$\chi_L^{LMTO}(\varepsilon,\kappa,\mathbf{r})=i^l Y_L(\hat{r})\begin{cases}\psi_l(\varepsilon,\mathbf{r})+\kappa\cot\left(\eta_l(\varepsilon)\right)J_l(\kappa r), & r<S\\ \kappa N_l(\kappa r), & r>S\end{cases},$$
$$J_l(\kappa r)=-\frac{\dot{\psi}_l(E_\nu,r)}{\kappa\frac{d}{d\varepsilon}\cot\left(\eta_l(E_\nu)\right)}. \qquad (1.14)$$

The form of $J_l(\kappa r)$ is obtained from the requirement that the energy derivative of χ_L^{LMTO} vanishes at $\varepsilon=E_\nu$ for $r\le S$ [7]. The augmented Neumann functions N_l are defined as n_l in the interstitial, with the tails in other spheres being given by the following expansion:

$$N_L(\kappa,\mathbf{r}-\mathbf{R})=4\pi\sum_{L',L''}C_{LL'L''}n^*_{L''}(\kappa,\mathbf{R}-\mathbf{R}')J_{L'}(\kappa,\mathbf{r}-\mathbf{R}'), \qquad (1.15)$$

where $N_L(\kappa,\mathbf{r})\equiv i^l Y_L(\hat{\mathbf{r}})N_l(\kappa r)$ and $C_{LL'L''}=\sqrt{(2l''+1)/4\pi}\,c^{l''}(lm,l'm')$ are related Gaunt coefficients $c^{l''}(lm,l'm')$ [7,23,24]. With the linearization, the trial wavefunction is correct up to the first order in the energy difference. However, the

final total energy can be rewritten in the form that makes it correct up to the third order [25]. For the study of ground state properties, E_ν is usually chosen at the centre of the occupied part of the valence density of states.

LMTO potential parameters

An important advantage of the LMTO method is that it can naturally parameterize the potential in terms of simple numbers related to scattering phase shifts. The parameters obtained (traditionally called 'potential parameters') completely define the Hamiltonian. The two dominant parameters, C and Δ, control most of the physics of the density-functional Hamiltonian. They supply a great deal of physical insight, and the way to construct them is described in greater detail in [94,7].

As mentioned before, the LMTO basis is constructed in such a way that the wavefunction inside the spheres is modified to consider the presence of the neighbouring atoms. The Bessel function $j_l(\kappa r)$ in (1.13), added to the function inside the MTO, assists in incorporating the effects due to the neighbours so that the minimal basis of the muffin tin orbital functions can accurately describe the system. Equation (1.15) allows expansion of the tail of an MTO into another sphere in terms of the functions inside the MTO.

Unlike the KKR method that leads to a set of non-linear equations, the MTO approach suggests the treatment of $\chi_L^{LMTO}(\varepsilon,\kappa,\mathbf{r})$ orbitals as functions of ε and κ separately, with a fixed choice of κ that simplifies the problem while being accurate for many problems.

The simplest way to obtain the MTO equation to choose $\kappa = 0$. This choice has been shown to work well, especially for close-pack solids. The reason is that the value of κ represents the variation of the wavefunction in the interstitial region, and for the close-packed structures the distance between the spheres is not large on the scale of the relevant kinetic energy near the Fermi level. As $\kappa \to 0$, the Bessel and Neumann functions in Equation (1.13) $j_l \to (r/S)^l$ inside the spheres and $n_l \to (r/S)^{-l-1}$ in the interstitial region. We can rewrite the MTO [26,7] as the following:

$$\chi_L^{MTO}(\varepsilon, 0, \mathbf{r}) = i^l Y_L(\hat{r}) \psi_l(\varepsilon, S) \begin{cases} \dfrac{\psi_l(\varepsilon, r)}{\psi_l(\varepsilon, S)} - \dfrac{D_l(\varepsilon) + l + 1}{2l+1} \left(\dfrac{r}{S}\right)^l, & r < S \\ \dfrac{l - D_l(\varepsilon)}{2l+1} \left(\dfrac{S}{r}\right)^l, & r > S \end{cases}, \quad (1.16)$$

where D_l is a dimensionless logarithmic derivative of $\psi_l(\varepsilon, r)$ at the sphere boundary. As $\kappa \to 0$ (1.15) for the wavefunction outside the spheres (for the details see [25]), we can use the following Fourier transform:

$$\sum_{T \neq 0} e^{i\mathbf{kT}} \left[\frac{S}{|\mathbf{r} - \mathbf{T}|}\right]^{l+1} i^l Y_L(r - T) \equiv \sum_{L'} \frac{-1}{2(2l'+1)} \left[\frac{r}{S}\right]^{l'} i^{l'} Y_{L'}(\mathbf{r}) S_{L'L}(\mathbf{k}),$$

where the structure factors

$$S_{L'L}(\mathbf{k}) = g_{l'm',lm} \sum_{\mathbf{T} \neq 0} e^{i\mathbf{kT}} \left[\frac{S}{|\mathbf{T}|}\right]^{l''+1} \left[\sqrt{4\pi} i^{l''} Y_{L''}(\mathbf{T})\right]^*;$$

where $g_{l'm',lm}$ can be expressed in terms of Gaunt coefficients [25]. The MTO basis is constructed by placing a localized MTO on each lattice site with the Bloch factor. The wavefunction in each sphere is the superposition of the 'head function'

belonging to the site and the 'tails' from the neighbouring spheres (Equation (1.16) for $r > S$):

$$\chi^{MTO}_{L,k}(\varepsilon,0,\mathbf{r}) = \psi_l(\varepsilon,r) i^l Y_L(\hat{r}) - \frac{D_l(\varepsilon)+l+1}{2l+1}\psi_l(\varepsilon,S)\left(\frac{r}{S}\right)^l i^l Y_L(\hat{r}) + \frac{l-D_l(\varepsilon)}{2l+1}\psi_l(\varepsilon,S)\sum_{L'}\left(\frac{r}{S}\right)^{l'} \frac{1}{2(2l'+1)} i^{l'} Y_{L'}(\hat{r}) S_{LL'}(\mathbf{k}). \quad (1.17)$$

The solution can be found as a linear combination of Bloch MTOs:

$$\psi_{\mathbf{k}}(\varepsilon,\mathbf{r}) = \sum_L a_L(\mathbf{k})\chi^{MTO}_{L,k}(\varepsilon,0,\mathbf{r}). \quad (1.18)$$

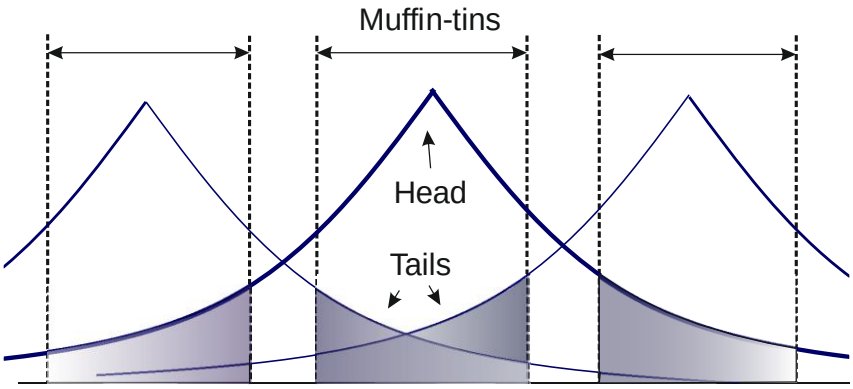

Fig. 2 Heads of MTOs and their tails in the neighbouring spheres, which must cancel each other in 'tail cancelation' scheme.

The linear combination of the second and the third terms in Equation (1.17) must vanish as the first term is already a solution inside the MTO; the procedure is called 'tail cancellation' (Fig. 2):

$$\sum_L \{S_{LL'}(\mathbf{k}) - P_l(\varepsilon)\delta_{LL'}\} a_L(\mathbf{k}) = 0. \quad (1.19)$$

$P_l(\varepsilon) = 2(2l+1)(D_l(\varepsilon)+l+1)/(D_l(\varepsilon)-l)$ are called 'potential functions'. Equation (1.19) is a set of linear homogeneous equations for the eigenvectors $a_L(\mathbf{k})$ in such a way that the determinant should vanish:

$$\det\left[S_{LL'}(\mathbf{k}) - P_l(\varepsilon)\delta_{LL'}\right] = 0. \tag{1.20}$$

All information about $P_l(\varepsilon)$ can be encapsulated in a small number of parameters (for details, see [27])

$$P_l(\varepsilon) = \frac{\varepsilon - C_l}{\Delta_l + \gamma_l(\varepsilon - C_l)}. \tag{1.21}$$

C_l, Δ_l, and γ_l are referred to as the centre, width, and distortion of the pure l^{th} band respectively. There is one value of γ_l, C_l, and Δ_l for each atom, orbital quantum number l, and spin. The relation between the parameters and the functions ψ_l and $\dot{\psi}_l$ is obtained by the requirement of the exact and parameterized forms of $P_l(\varepsilon)$ to coincide at $\varepsilon = \varepsilon_v$ up to the second derivative. Equation (1.21) leads to the following:

$$\varepsilon(P_l) = C_l + \frac{P_l\Delta_l}{1-\gamma P_l}. \tag{1.22}$$

The LMTO Hamiltonian can be expressed in terms of the diagonal matrices C, Δ, and γ corresponding to the potential parameters C_l, Δ_l, and γ_l [28]:

$$H_{LMTO}\psi = \varepsilon\psi, \quad \text{with } H_{LMTO} = C + \sqrt{\Delta}\left(S^{-1} - \gamma\right)^{-1}\sqrt{\Delta}. \tag{1.23}$$

This form is now called the γ-representation.

As mentioned before, potential parameters supply a great deal of physical insight. Combining Equation (1.22) with Equation (1.20) leads to the band structure:

$$\varepsilon(P_l) = C_l + \frac{\Delta_l S_{l,i}(\mathbf{k})}{1 - \gamma_l S_{l,i}(\mathbf{k})}, \tag{1.24}$$

where i numbers a solution of Equation (1.20) and $S_{l,i}(\mathbf{k})$ are the eigenvalues of the block of the structure constant matrix $S_{l'm',lm}$, for the angular moment l (the blocks can be separated if for the sake of simplicity one neglects hybridization – i.e. if the elements of $S_{l',l}$ with $l \neq l'$ are equal to zero) [7]. This construction leads to a simple formulation of the energy bands with the centre fixed by C_l, the width scaled by Δ_l, and the distortion parameter γ_l.

Green's function method

The Korringa-Kohn-Rostoker (KKR) method, also known as the multiple scattering theory (MST) or Green's function (GF) method, was suggested independently by Korringa [29] and Kohn and Rostoker [30]. In this method, the multiple scattering theory is used for solving the Schrödinger equation. KKR works well when dealing with solids with reduced symmetry, such as the ordered crystals with impurities, surfaces, layered systems, etc. Another application of the method is the investigation of randomly disordered alloys by the coherent potential approximation (CPA), which will be discussed later in more detail. The

KKR method and the Green functions are described in many books and reviews [31-34].

The Green's function G corresponding to the Hamiltonian H is defined as:

$$(E-H)G(E)=1, \text{ and } G(E)=(E-H)^{-1}. \tag{1.25}$$

When the GF of a system is determined, all physical properties of the system can be calculated. For the inverse of a differential operator to be defined uniquely, its boundary conditions must be specified. To do so an infinitesimal imaginary part, ξ, must be added to energy

$$G(E)=(E-H+i\xi)^{-1}, \text{ where } \xi \to 0.$$

In a complete orthonormal basis, the GF may be expressed in terms of the eigenfunctions of the Hamiltonian in an abstract vector space:

$$G(E)=\sum_i |\psi_i\rangle \frac{1}{E-\varepsilon_i+i\xi}\langle\psi_i|, \tag{1.26}$$

where ε_i are the eigenvalues. The Sokhotski-Plemelj theorem is used to calculate the physical observables using GF:

$$\lim_{\delta\to 0^+}\left[\frac{1}{E-\varepsilon_i+i\xi}\right]=P\left(\frac{1}{E-\varepsilon_i}\right)-i\pi\delta(E-\varepsilon_i), \tag{1.27}$$

where P is the Cauchy principal value of the integral and $\delta(E-\varepsilon_i)$ is the Dirac δ-function.

In KKR, the muffin-tin orbital on each site is considered as a spherical scatterer, and electrons propagate between them, as described by the Green's function G [36] ($G(\varepsilon,\mathbf{r},\mathbf{r}')\equiv\langle\mathbf{r}|G(E)|\mathbf{r}'\rangle$ describes propagation of a particle with

energy ε from point $\mathbf{r}$ to $\mathbf{r}'$). Through direct calculation of the Green's function we can avoid the calculation of the eigenvalues and eigenstates of the Hamiltonian. This is particularly useful when the potential becomes energy-dependent, as it does in the CPA. In Kohn-Sham formalism, Equation (1.25) corresponding to Hamiltonian (1.7) becomes in the coordinate representation:

$$\left[E + \frac{1}{2}\nabla^2 - V_{KS}^{\sigma}(\mathbf{r}) + i\xi \right] G(\mathbf{r}, \mathbf{r}', E) = \delta(\mathbf{r} - \mathbf{r}'). \tag{1.28}$$

If the eigenvalues ε_i correspond to the eigenfunctions $\psi_i(\mathbf{r})$, satisfying the completeness and orthonormality conditions

$$\int \psi_i^*(\mathbf{r})\psi_j(\mathbf{r}) d^3\mathbf{r} = \delta_{ij}, \quad \sum_i \psi_i^*(\mathbf{r})\psi_j(\mathbf{r}') = \delta(\mathbf{r} - \mathbf{r}'),$$

the Green's function can be written in the spectral representation Equation (1.26). Writing in the coordinate representation:

$$G(\mathbf{r}, \mathbf{r}', E) = \sum_i \frac{\psi_i(\mathbf{r})\psi_i^*(\mathbf{r}')}{E - \varepsilon_i + i\xi}. \tag{1.29}$$

Using Equation (1.27), one can see that when approaching the real axis ($\xi \to 0^+$) the imaginary part of the diagonal elements of G

$$\lim_{x \to 0^+} \left[-\frac{1}{\pi} \operatorname{Im} G(\mathbf{r}, \mathbf{r}, E) \right] = \sum_i |\psi_i(\mathbf{r})|^2 \, \delta(E - \varepsilon_i), \tag{1.30}$$

and the local density of states (DOS)

$$n(\mathbf{r}, E) = -\frac{1}{\pi} \operatorname{Im} G(\mathbf{r}, \mathbf{r}, E). \tag{1.31}$$

At equilibrium, the single-particle density $\rho(\mathbf{r})$ is obtained by integrating $n(\mathbf{r}, E)$ over all occupied one-electron states up to the Fermi energy:

$$\rho(\mathbf{r}) = -\frac{1}{\pi}\int_{-\infty}^{E_F} \mathrm{Im}\, G(\mathbf{r},\mathbf{r},E)dE, \tag{1.32}$$

while the total DOS

$$n(E) = \int n(\mathbf{r},E)d^3r = -\frac{1}{\pi}\mathrm{Tr}\left[\mathrm{Im}\, G(E)\right]. \tag{1.33}$$

The GF method can be implemented within LMTO formalism. Solving the one electron GF equation should be equivalent to solving the Schrödinger equation (1.7). In the operator form, the equation takes the following form:

$$LG = GL = 1,$$

where the operator L

$$L(\mathbf{r},\mathbf{r}',E) = \left[E + \nabla_{\mathbf{r}}^2 - V(\mathbf{r})\right]\delta(\mathbf{r}-\mathbf{r}').$$

The GF is usually determined by decomposing L into an unperturbed part, L_0, and a perturbation, U:

$$L = L_0 - U,$$

where the unperturbed part satisfies the relation $L_0 G_0 = G_0 L_0 = 1$, with G_0 being an unperturbed Green's function corresponding to independent-particle electronic structure problems. Hence, the equation on the perturbed GF G yields the form of the Dyson equation:

$$G = G_0 + G_0 V G = \left[1 - G_0 V\right]^{-1} G_0. \tag{1.34}$$

In case of muffin-tin potential, electrons are considered propagating with a free propagator (or a Green's function) between the muffin-tins that act as

spherical chatterers. In multiple scattering theory [7,32,33,35], Green's function is written in a mixed site-angular-momentum representation as the following:

$$G(\mathbf{r}+\mathbf{R}_i,\mathbf{r}'+\mathbf{R}_j;E)=\sum_{LL'}R_L^i(\mathbf{r};E)G_{LL'}^{ij}(E)R_{L'}^j(\mathbf{r}')$$
$$+\delta_{ij}\sum_L R_L^i(\mathbf{r}_<;E)H_L^i(\mathbf{r}_>;E),$$

where $L=(lm)$ (or $L=(\kappa\mu)$ in the fully relativistic case discussed in **Chapter** 2) are angular-momentum indices, and $R_L^i(\mathbf{r};E)$ and $H_L^i(\mathbf{r};E)$ are the regular and irregular scattering solutions corresponding to the potential centred at $\mathbf{R}_i$ [35]. The structural Green's function matrix $G(E)=\left\{G_{LL'}^{ij}(E)\right\}$ in multiple scattering theory is expressed in terms of the scattering matrix elements *t*, representing single scattering events from the muffin-tins as

$$G=G^0+G^0tG^0+G^0tG^0tG^0+...=G^0\left(I-tG^0\right)^{-1},$$

where $G^0(E)=\left\{G_{LL'}^{0,ij}(E)\right\}$ is the free-space counterpart of *G*, usually called bare structure constants, and $t(E)=\left\{t_{LL'}^i(E)\delta_{ij}\right\}$ are diagonal in the angular-momentum indices if the muffin-tin potentials are used.

Solving Equation (1.34) within the ASA and LMTO methods, which can be found in detail in [27,28], GF is expressed in terms of the same potential functions introduced in Equation (1.19):

$$G(E)=-\frac{1}{2}\frac{\ddot{P}(E)}{\dot{P}(E)}+\sqrt{\dot{P}(E)}\left[P(E)-S\right]^{-1}\sqrt{\dot{P}(E)}. \qquad (1.35)$$

The equation is sometimes rewritten as:

$$G(E)=\lambda(E)+\mu(E)g(E)\mu(E), \qquad (1.36)$$

where

$$g(E) = \left[P(E) - S\right]^{-1},$$
$$\mu(E) = \sqrt{\dot{P}(E)}, \qquad (1.37)$$
$$\lambda(E) = -\frac{1}{2}\frac{\ddot{P}(E)}{\dot{P}(E)}.$$

To distinguish between them, $G(E)$ is referred to as the physical GF, while $g(E)$ is referred to as the auxiliary GF.

Coherent potential approximation

There are two ways to analyse alloys. The first one is by using a supercell approach; the second one is through configurational averaging of physical observables over the disorder. The latter one, CPA is especially effective while using the Green's functions approach. It requires calculation of the configurational average of G, $\langle G \rangle$. Once it is known, the configurationally averaged observables can be calculated from it. The theoretical background of the method will be given here: **Chapter 3** presents the application of CPA to real materials like $(Ni_{1-x}Fe_x)_{1-y}Z_y$, *Z=Cu, Rh, Cr,* and *Mn* alloys; it also compares the computational results with experimental data. The CPA method has been initially formulated in the works of P. Soven [76] and B. Velicky *et al.* [77], M. Lax [78] and J. L. Beeby [79].

The idea of CPA is to create an average potential in such a way that if placed on a site, it should be able to approximate the potential created by an actual alloy in the best possible manner. The potential function *P* defined above is

replaced by the 'coherent potential' Ω, constructed by averaging the scattering properties of different atoms embedded in an effective potential, see [7]. This method has been formulated for KKR-CPA by Stocks et al. [80]. The method also includes building a configurationally averaged Green's function (which is also required for calculating the corresponding observables) as the averaging here is done over the scattering properties of different atoms in a system.

The formulation of CPA within the LMTO was introduced by J. Kudrnovsky, V. Drchal, and J. Mašek [81]. Detailed insights into CPA can be found in many books and reviews [82-84].

Let us consider a binary alloy comprising two components Q = A and B, distributed randomly over the lattice with the probabilities $c_{\mathbf{R}}^{A}$ and $c_{\mathbf{R}}^{B}$ ($c_{\mathbf{R}}^{A}+c_{\mathbf{R}}^{B}=1$) [75]. At each site **R,** we have two potentials $V_{\mathbf{R}}^{Q}$ with the probabilities $c_{\mathbf{R}}^{Q}$. Now, all the quantities, such as potential functions and potential parameters, take on two different values: $P_{\mathbf{R}}^{Q}(z)$, $C_{\mathbf{R}}^{Q}$, $\Delta_{\mathbf{R}}^{Q}$, $\gamma_{\mathbf{R}}^{Q}$ with the same probabilities and, in turn, define the LMTO Hamiltonian (1.23) and Green's functions (1.36), which are used to find the electronic structure of a system. For each alloy configuration and in an LMTO representation, the potential parameters are given by the formulas similar to Equation (1.37).

We assume a completely random system without any statistical correlation between atoms occupying different sites. Let $\eta_{\mathbf{R}}^{Q}$ be an occupational index: $\eta_{\mathbf{R}}^{Q}=1$ if atom of the type *Q* is at the site **R,** and 0 otherwise. The configurational average of an occupational index $\left\langle \eta_{\mathbf{R}}^{Q} \right\rangle = c_{\mathbf{R}}^{Q}$ and obeys the following relation

$$\left\langle \eta_{\mathbf{R}}^{Q}\eta_{\mathbf{R}'}^{Q'}\right\rangle = c_{\mathbf{R}}^{Q}\delta_{\mathbf{R},\mathbf{R}'}\delta_{Q,Q'} + c_{\mathbf{R}}^{Q}c_{\mathbf{R}'}^{Q'}\left(1-\delta_{\mathbf{R},\mathbf{R}'}\right), \tag{1.38}$$

where $\langle ... \rangle$ denotes the configurational averaging. A random site non-diagonal quantity, $X_{\mathbf{R},\mathbf{R}'}$, can be written as:

$$X_{\mathbf{R},\mathbf{R}'} = \sum_{Q,Q'} \eta_{\mathbf{R}}^{Q} X_{\mathbf{R},\mathbf{R}'}^{Q\,Q'} \eta_{\mathbf{R}'}^{Q'}. \tag{1.39}$$

The physical GF for one alloy concentration (A or B) has the form of Equation (1.36). For the alloy with two components, the Green's function matrix in LMTO representation becomes as the following:

$$G_{\mathbf{R},\mathbf{R}'}(E) = \sum_{Q} \lambda_{\mathbf{R}}^{Q}(E)\eta_{\mathbf{R}}^{Q}\delta_{\mathbf{R},\mathbf{R}'} + \sum_{Q}\sum_{Q'} \mu_{\mathbf{R}}^{Q}(E)\eta_{\mathbf{R}}^{Q} g_{\mathbf{R},\mathbf{R}'}(E)\eta_{\mathbf{R}'}^{Q'}\mu_{\mathbf{R}'}^{Q'}(E). \tag{1.40}$$

After performing the configurational averaging [75] for the site-diagonal elements, one obtains:

$$\begin{aligned} \left\langle G_{\mathbf{R},\mathbf{R}}(E)\right\rangle &= \sum_{Q} c_{\mathbf{R}}^{Q}\left\langle G_{\mathbf{R},\mathbf{R}}^{Q}(E)\right\rangle, \\ \left\langle G_{\mathbf{R},\mathbf{R}}^{Q}(E)\right\rangle &= \lambda_{\mathbf{R}}^{Q}(E) + \mu_{\mathbf{R}}^{Q}(E)\left\langle g_{\mathbf{R},\mathbf{R}}^{Q}\right\rangle \mu_{\mathbf{R}}^{Q}(E), \end{aligned} \tag{1.41}$$

where the auxiliary GF (introduced in Equation (1.37)) is defined as

$$\left\langle g_{\mathbf{R},\mathbf{R}}^{Q}(E)\right\rangle = \frac{1}{c_{\mathbf{R}}^{Q}}\left\langle \eta_{\mathbf{R}}^{Q} g_{\mathbf{R},\mathbf{R}}(E)\right\rangle, \tag{1.42}$$

and $\lambda_{\mathbf{R}}^{Q}(E)$ and $\mu_{\mathbf{R}}^{Q}(E)$ are the same parameters defined in (1.37), introduced for the alloy components *Q*.

Hence, the conditionally averaged GF (1.41) describes the decomposition of an averaged GF into contributions corresponding to the occupation of the site **R** by each of two atom types A and B. Similar equations can be obtained for the site non-diagonal elements of the configurationally averaged GF matrix [75]. In CPA,

the coherent potential function is defined similar to the one introduced in LMTO approximation (1.20):

$$\left\langle g_{\mathbf{R},\mathbf{R}'}(E)\right\rangle = \left[\left(P(E)-S\right)^{-1}\right]_{\mathbf{R},\mathbf{R}'}. \tag{1.43}$$

This function, as well as the physical GF $G_{\mathbf{R},\mathbf{R}}(E)$ after configurational averaging (1.41), describes the properties of the system of 'effective' atoms placed at the lattice sites. These atoms are described by the effective site-diagonal coherent potential functions $P_{\mathbf{R}}^{Q}(E)$. An atom of the type *Q* is considered to occupy a given site **R,** while all other sites are occupied by 'effective' atoms, characterized by the coherent potential functions $P_{\mathbf{R}}^{Q}(E)$.

The formulas obtained for the binary alloys can be generalized for the case of alloys with a larger number of components, since it only requires the sum over $Q = A, B$ to be replaced by the sum over a larger number of components.

A concept of self-energy (which will be used in Chapter 3) can be introduced within the LMTO method; its real and imaginary parts are interpreted as the energy shifts and lifetimes of electron bands:

$$\left\langle G(E)\right\rangle = \left[E - H^{0} - \Sigma(E)\right]^{-1}, \tag{1.44}$$

where H^{0} is the non-random reference Hamiltonian with respect to which self-energy is defined [75]. In the simple case of the 'diagonal' disorder ($\Delta^{A} = \Delta^{B} = \Delta,$ and $\gamma^{A} = \gamma^{B} = \gamma$), self-energy can be expressed in terms of the same potential parameters [75]:

$$\Sigma_{\mathbf{R}}(E) = E - \Delta_{\mathbf{R}} P_{\mathbf{R}}(E). \tag{1.45}$$

In the framework of the many-body theory, the lifetime of an excited electron in the state $\phi(\mathbf{r})$ with the energy E can be calculated from the imaginary part of electron self-energy as:

$$\tau^{-1} = -2\int dr \int dr' \phi^{*}(r)\,\mathrm{Im}\,\Sigma(r, r', E)\phi(r), \tag{1.46}$$

where τ is the electron lifetime. For more details regarding the lifetime, see [37].

CPA generally provides reliable concentration-dependent trends for the ground-state physical quantities. It is also known to give an accurate description of the electronic spectra and thermodynamic properties of real materials. The accuracy of CPA decreases with decreasing nearest-neighbour coordination.

As a single-site theory, CPA fails to take into account statistical fluctuations with respect to the chemical composition of an alloy. It also does not treat correctly off-diagonal disorder (as opposed to diagonal disorder, defined above). Another weakness of this method is that it cannot take into account the short-range ordering effects (such as chemical clustering).

Chapter 2. Relativistic LMTO

For the systems with heavy elements (5d-transition metals, actinides), relativistic effects become non-negligible. In magnetic solids, even with the light elements, the role of these effects is important. For instance, the spin-orbit interaction in 3d transition metals gives rise to a number of interesting phenomena such as magnetocrystalline anisotropy [38] and galvano-magnetic phenomena [39].

Spin-orbit coupling is the relativistic interaction between the spin magnetic moment of an electron and the magnetic field induced by its own orbital motion. It arises naturally in the relativistic Dirac equation of the electron [61], but can also be treated as a perturbation in the non-relativistic theory [40,41,22].

In such cases, the scalar relativistic (SR) method is often used which consists in adding modifications to the non-relativistic Schrödinger equation. Various non-relativistic techniques are, for example, removing the coupling between the large and small components of the Dirac equation [61], elimination techniques [42,43], ZORA-scheme that adds relativistic corrections to the Hamiltonian [44], and many others.

Nevertheless, more accurate treatment of relativistic phenomena requires the implementation of the fully relativistic theory, starting with the Dirac equation. Scalar-relativistic methods do not consider any lowering of the symmetry caused by the coupling of the spin and orbital degrees of freedom; they

cannot account for a number of physical phenomena caused by spin-orbit coupling.

The technical problems of dealing with the spin-polarized Dirac equation for a single-site problem were first solved by S. Doniach and C. Sommers, who derived the corresponding coupled radial Dirac equation [45] and then considered in more details by Feder et al. [46] and by Strange et al. [47]. This development has then been introduced to other band-structure schemes such as KKR [46,48], LMTO [21] and ASW [49]. Additional details can be found in the works of Solovyev et al. [50,51,52].

In this chapter, the modification of the scalar-relativistic code (using the modified Schrödinger equation) to the fully relativistic (FR) LMTO scheme (using the Dirac equation) will be described in application to the Questaal electronic structure code [53]. The procedure implemented is similar to that of Ebert [21].

For purposes of solving the Dirac equation, a spherical potential is assumed, since any dominant correction to the Schrodinger equation originates from regions near the nucleus where the kinetic energy is large. The Dirac equation for an electron moving in the potential field $V(r)$, which generalizes the Schrödinger equation in the relativistic form, is given by [75]

$$\begin{aligned} \hat{H}_0 \Psi_i &= E_i \Psi_i \\ \hat{H}_0 &= c\boldsymbol{\alpha} \cdot \mathbf{p} + (\beta - I_4)mc^2 + V(\mathbf{r})I_4, \end{aligned} \tag{2.1}$$

where $\mathbf{p} = -i\hbar\Delta$ is the momentum operator, and the four-component wave functions

$$\Psi_i = \begin{pmatrix} \phi \\ \chi \end{pmatrix}_i$$

are the bispinors comprising two components – the large component ϕ and the small component χ; and α and β are the Dirac matrices

$$\alpha = \begin{pmatrix} 0 & \sigma \\ \sigma & 0 \end{pmatrix}, \quad \beta = \begin{pmatrix} I_2 & 0 \\ 0 & -I_2 \end{pmatrix}.$$

Here σ are Pauli matrices and I_n denotes the $n \times n$ unit matrix. The effective potential had been introduced before within the LDA in terms of the particle density $\rho(\mathbf{r})$ in Equation (1.8):

$$V(\mathbf{r}) = V^{ext}(\mathbf{r}) + \int d^3\mathbf{r}' \frac{2\rho(\mathbf{r}')}{|\mathbf{r} - \mathbf{r}'|} + \frac{\delta E_{ex}[\rho]}{\delta\rho(\mathbf{r})}. \tag{2.2}$$

Within the ASA, the effective potential is a sum of spherically symmetric potentials placed at lattice sites. Equation (2.1) with the effective potential of Equation (2.2) is called the Kohn-Sham-Dirac equation and is the basic equation of relativistic density functional theory.

In a spherical potential, the Dirac Hamiltonian (2.1) has a set of mutually commuting constants of motion [75]:

$$\left[H_0, J^2\right] = 0, \quad \left[H_0, J_z\right] = 0, \quad \left[H_0, S^2\right] = 0, \quad \left[H_0, K\right] = 0,$$
$$\mathbf{J} = \mathbf{L} + \mathbf{S}, \quad K = \beta(1 + \boldsymbol{\Sigma} \cdot \mathbf{L}),$$

where $\boldsymbol{J}$ is the total angular momentum operator, J^2 is its square, J_z is its z-projection, $\boldsymbol{L}$ is the orbital angular momentum operator, and $\mathbf{S} = 1/2\boldsymbol{\Sigma}$ is the spin angular operator with

$$\boldsymbol{\Sigma} = \begin{pmatrix} \boldsymbol{\sigma} & 0 \\ 0 & \boldsymbol{\sigma} \end{pmatrix}.$$

So, the eigenstates of the Hamiltonian can be distinguished in accordance with the quantum numbers *j*, *m*, σ, and κ. But since not all of them are independent [75], it is sufficient to use only two quantum numbers, κ and μ:

$$\kappa = \begin{cases} -l-1 & \text{for } j = l+1/2 \\ l & \text{for } j = l-1/2 \end{cases}, \kappa = \pm 1, \pm 2, \pm 3, ..., \tag{2.3}$$

$$\mu = \pm\frac{1}{2}, \pm\frac{3}{2}, \pm\frac{4}{2}, \quad -j \le \mu \le j, \quad j = \frac{1}{2}, \frac{3}{2}, \frac{5}{2}, \ldots . \tag{2.4}$$

A solution of the single-site Dirac equation for spherically symmetric potential is given by [75]

$$\Phi_{\Lambda}(E, \mathbf{r}) = \begin{pmatrix} g_k(E,r)\Omega_{\kappa\mu}(\hat{\mathbf{r}}) \\ if_k(E,r)\Omega_{-\kappa\mu}(\hat{\mathbf{r}}) \end{pmatrix}, \quad \Lambda = (\kappa, \mu). \tag{2.5}$$

The radial amplitudes $g_k(E,r)$ and $f_k(E,r)$ are the regular solutions of the radial Dirac equations [21]

$$\left(\frac{\partial}{\partial r} + \frac{1+\kappa}{r}\right) g_k(E,r) - \left(\frac{E - V(r)}{c^2} + 1\right) c f_k(E,r) = 0, \tag{2.6}$$

$$\left(\frac{\partial}{\partial r} + \frac{1-\kappa}{r}\right) c f_k(E,r) + (E - V(r)) g_k(E,r) = 0. \tag{2.7}$$

They should be regular for $r \to 0$ and are normalized within the Wigner-Seitz sphere so that

$$\int_0^s dr\, r^2 \left[g_k^2(E,r) + f_k^2(E,r) \right] = 1. \tag{2.8}$$

It can be seen that the second term in Equations (2.6) and (2.7) depends on the quantum number κ and has no non-relativistic counterpart compared to the Schrödinger equation. Hence, it can be identified with spin-orbit coupling.

The spin-spherical harmonics $\Omega_{\kappa\mu}(\hat{\mathbf{r}})$ are two-component spinors

$$\Omega_{\kappa\mu}(\hat{\mathbf{r}}) = \sum_{\sigma=\pm\frac{1}{2}} c\left(lj\frac{1}{2};\mu-\sigma,\sigma\right) Y_{l,\mu-\sigma}(\hat{\mathbf{r}})\varphi_\sigma, \tag{2.9}$$

defined [54,61] in terms of the Clebsch-Gordan coefficients $c\left(lj\frac{1}{2};\mu-\sigma,\sigma\right)$, the spherical harmonics $Y_{l,\mu-\sigma}$, and the spin functions

$$\varphi_{\frac{1}{2}} = \begin{pmatrix}1\\0\end{pmatrix}, \varphi_{-\frac{1}{2}} = \begin{pmatrix}0\\1\end{pmatrix}.$$

For small *r*, the leading term of the potential $V(r) = -2Z/r$ and the large and small components behave like [75]

$$\begin{pmatrix} g_k(E,r)\\ f_k(E,r)\end{pmatrix} \cong Ar^a \begin{pmatrix}1\\q\end{pmatrix}, \quad a = -1+\left[\kappa^2-(2Z/c)^2\right]^{1/2}, \quad q = \frac{c}{2Z}(\kappa+1+a), \tag{2.10}$$

where *A* is a normalization constant; *a* and *q* are obtained by inserting the first equation of (2.10) into Equations (2.6) and (2.7).

Let us now consider the spin-polarized case. With the external magnetic field applied, the Dirac Hamiltonian has the form [75]

$$\hat{H}_0 = c\boldsymbol{\alpha}\cdot\left[\mathbf{p}-(e/c)\mathbf{A}(\mathbf{r})\right] + (\beta - I_4)mc^2 + V(\mathbf{r})I_4. \tag{2.11}$$

In the spherically symmetric scalar potential, when the magnetic field is directed along *z*, the solutions of the single-site Dirac equation for a given energy *E* are classified according to the eigenvalues μ and have the following form:

$$\Phi_\mu(E,\mathbf{r}) = \sum_\kappa \Phi_{\kappa\mu}(E,\mathbf{r}), \quad \Phi_\mu(E,\mathbf{r}) = \begin{pmatrix} g_{\kappa\mu}(E,r)\Omega_{\kappa\mu}(\hat{\mathbf{r}})\\ if_{\kappa\mu}(E,r)\Omega_{-\kappa\mu}(\hat{\mathbf{r}})\end{pmatrix}. \tag{2.12}$$

The radial amplitudes $g_{\kappa\mu}(E,r)$ and $f_{\kappa\mu}(E,r)$ satisfy the set of coupled radial Dirac equations [75]:

$$\left(\frac{d}{dr}+\frac{1+\kappa}{r}\right)g_{k\mu}(E,r)-\left(\frac{E-V(r)}{c^2}+1\right)cf_{\kappa\mu}(E,r)$$
$$-\frac{B(r)}{c^2}\sum_{\kappa'}\langle -\kappa\mu|\sigma_z|-\kappa'\mu\rangle cf_{\kappa'\mu}(E,r)=0, \tag{2.13}$$

$$\left(\frac{d}{dr}+\frac{1-\kappa}{r}\right)cf_{k\mu}(E,r)-(E-V(r))g_{\kappa\mu}(E,r)$$
$$-B(r)\sum_{\kappa'}\langle \kappa\mu|\sigma_z|\kappa'\mu\rangle g_{\kappa'\mu}(E,r)=0, \tag{2.14}$$

where the matrix element is

$$\langle \kappa\mu|\sigma_z|\kappa'\mu'\rangle=-\delta_{\mu\mu'}\left[\frac{2\mu}{2\kappa+1}\delta_{\kappa\kappa'}+\frac{\sqrt{(\kappa-\kappa')^2-4\mu^2}}{|\kappa-\kappa'|}\delta_{\kappa+\kappa',-1}\right], \tag{2.15}$$

and $B(\mathbf{r})=\nabla\times A(\mathbf{r})$ is the magnetic field defined via the potential vector $A(\mathbf{r})$ [21,55,75]. For spherically symmetric potential, the magnetic field can be assumed to be pointing in the z-direction so that $B(\mathbf{r})=B(r)\hat{\mathbf{z}}$, where $\hat{\mathbf{z}}$ is the unit vector parallel to the z-axis.

The infinite set of coupled Dirac equations is separated into coupled equation for each pair ($l\mu$). Two cases are to be distinguished:

- States with $|\mu|=l+1/2$. There is no coupling between the two equations and therefore there is only one regular solution with $\kappa\mu$ as in the non-magnetic case.

- States with $|\mu|<l+1/2$. There are four coupled equations (2.13), (2.14) for the four unknown functions $g_{\kappa\mu}(E,r)$, $f_{\kappa\mu}(E,r)$, $g_{\kappa'\mu}(E,r)$, and $f_{\kappa'\mu}(E,r)$, where $\kappa'=-\kappa-1$.

Solving the radial Dirac equation

A stiff system of equations

With a number of simplifications (for the radial case and neglecting the terms of the order of $1/c^2$), the Dirac equation's solution eventually comes down to solving the four radial differential equations of (2.13), (2.14) with two possible independent solutions.

The main difficulty here (if not for it, we would have been able to use one of the many ways of solving a system of differential equations) lies in the fact that (2.13)-(2.14) is a stiff system of equations. It means that the system includes a term that varying rapidly accumulates the error and pulls the solution off its track. The standard integration starting from the origin and moving outside, when consecutive integration points are not close enough, may lead to an admixture of numerical errors and the solution becomes unreliable at some point. The typical method of solving such systems is to integrate the equations both outwards and inwards. Both these become unreliable at some point. However, the stable portion of each is chosen, and the two solutions are matched at a convenient matching radius, hence dropping the unreliable parts for both (see Fig. 3). Unlike the scalar-relativistic case, where the wave function and its radial derivative are matched, here we get a mismatch of two solutions and need a way to vary and sew them together. And since we have to find all the eight functions ($g_{\kappa\mu}(E,r)$, $f_{\kappa\mu}(E,r)$, $g_{\kappa'\mu}(E,r)$, and $f_{\kappa'\mu}(E,r)$), all of them must be matched at the same time – this

makes the problem trickier. For integrating the system of differential equations, we used the Runge-Kutta method [63].

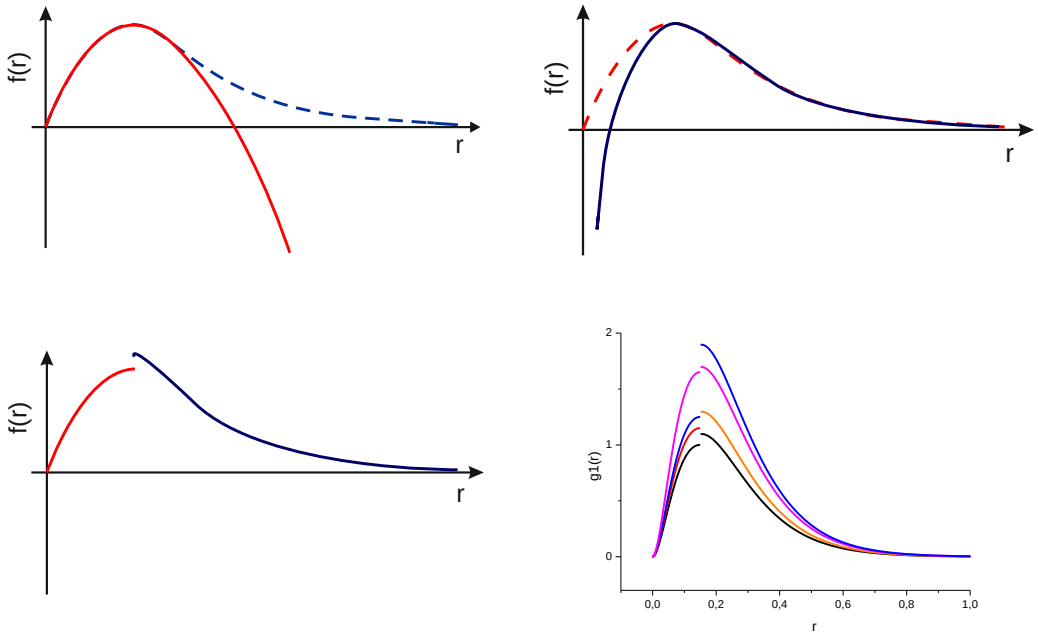

Fig. 3 Schematic matching of the Dirac equation solution. (top left) Integration outwards accumulating errors, (top right) integration inwards, (bottom left) matching the reliable parts, (bottom right) matching several functions at the same time.

The core state eigenvalue problem

The method of solving the Dirac equation numerically for the core states used here is described by Ebert [21]. The solution (for both core and valence states) should be regular at the origin. Hence, the initial point for outward integration at the origin for both large and small components is chosen as [55,75]

$$\begin{pmatrix} g_\kappa^{out}(E,r) \\ f_\kappa^{out}(E,r) \end{pmatrix} \cong Cr^a \begin{pmatrix} 1 \\ q \end{pmatrix}, \qquad (2.16)$$

$$a = -1 + \left[\kappa^2 - (2Z/c)^2\right]^{1/2}, \quad q = \frac{c}{2Z}\left(\kappa + 1 + a\right),$$

where C is the normalization constant.

In case of large distances, the solution for the core states should decay exponentially [11]. Two independent solutions for Equations (2.13) and (2.14) are distinguished by setting $\kappa_i = \kappa$ ($\kappa_i = -\kappa - 1$) and $g_{\bar{\Lambda},0}, f_{\bar{\Lambda},0} = 0$ ($g_{\Lambda,0}, f_{\Lambda,0} = 0$) [55].

The matching of the two solutions is possible only if the wavefunctions are evaluated for the correct energy eigenvalue. Since the wavefunction is to be normalized, there are only four parameters to vary for the matching: the relative scale factor *A*; the relative weights of the two solutions A^{out}, A^{in}; and the energy *E*. To find the energy eigenvalue, Ebert suggests constructing the four-component error function

$$F = \begin{bmatrix} \left(g_{\Lambda 1}^{out} + A^{out} g_{\Lambda 2}^{out}\right) - A\left(g_{\Lambda 1}^{in} + A^{in} g_{\Lambda 2}^{in}\right) \\ c\left(f_{\Lambda 1}^{out} + A^{out} f_{\Lambda 2}^{out}\right) - cA\left(f_{\Lambda 1}^{in} + A^{in} f_{\Lambda 2}^{in}\right) \\ \left(g_{\bar{\Lambda} 1}^{out} + A^{out} g_{\bar{\Lambda} 2}^{out}\right) - A\left(g_{\bar{\Lambda} 1}^{in} + A^{in} g_{\bar{\Lambda} 2}^{in}\right) \\ c\left(f_{\bar{\Lambda} 1}^{out} + A^{out} f_{\bar{\Lambda} 2}^{out}\right) - cA\left(f_{\bar{\Lambda} 1}^{in} + A^{in} f_{\bar{\Lambda} 2}^{in}\right) \end{bmatrix},$$

which is evaluated at the matching radius $r = r_m$ and is a function of the parameter vector $P = \left[E, A, A^{out}, A^{in}\right]$. The eigenvalue should be found by solving the equation $F(P) = 0$. For the initial guess, $A = g^{out} / g^{in}$ should be used, while A^{out} and A^{in} should be set to some percentage value, where energy is guessed from the scalar-relativistic case. Then, $F(P) = 0$ is solved iteratively. The matching point is usually chosen to be at the maximum/minimum of the function *g* (furthest from the origin) [64].

Valence states

After implementing a method similar to that of Ebert [21] to solve the Dirac equation for the core states, the same must be done for the valence states. The difference here lies primarily in the outer boundary conditions (the initial point for integration inwards). The asymptotic analytical form of the solution cannot be used to start the integration inwards. After trying different ways of setting the initial point, we decided that the values of the wavefunction obtained by the integration outwards should be used as a guess for the initial point of the inward integration. It was noted that during the integration out from the origin, the solution does not fall off its track dramatically and hence we can account for the accumulated errors further. For the correction function *F*, the difference (gap) between the values of the wavefunctions obtained by the integration inwards and outwards at the matching point will be used here:

$$F = \begin{bmatrix} g_{\Lambda}^{out}(r_m) - g_{\Lambda}^{in}(r_m) \\ f_{\Lambda}^{out}(r_m) - f_{\Lambda}^{in}(r_m) \\ g_{\bar{\Lambda}}^{out}(r_m) - g_{\bar{\Lambda}}^{in}(r_m) \\ f_{\bar{\Lambda}}^{out}(r_m) - f_{\bar{\Lambda}}^{in}(r_m) \end{bmatrix}. \tag{2.17}$$

Now the parameter vector *P* consists of the values of the wavefunctions' radial amplitudes at the outer boundary (initial point for the inward integration, which should be shifted around to match the solutions) $P = \left[g_{\Lambda}(r_{\max}), f_{\Lambda}(r_{\max}), g_{\bar{\Lambda}}(r_{\max}), f_{\bar{\Lambda}}(r_{\max}) \right]$. The eigenvalues are calculated by the scalar relativistic method, and the initial point for the inward integration is obtained iteratively by solving the equation $F(P) = 0$ with Newton's algorithm.

Charge density and density of states. When the Schrödinger equation is replaced by the Dirac equation, several changes must be made to the rest of the code: the wavefunctions become matrices in accordance with the new quantum numbers, potential parameters, Green's functions change, as well as some other quantities like charge and spin densities, etc. [62]. Expressions for these quantities have been derived for the relativistic LMTO method, both for the non-magnetic [65,66] and spin-polarized cases [21,50-52], as well as the fully relativistic treatment of CPA [62]. For the relativistic CPA case, the spherically averaged particle density for a site occupied by an atom of the type *Q* has the following form [62]:

$$\rho^{Q}(r)=\frac{1}{4\pi}\sum_{\kappa\mu}\left[\Re^{Q,(gg)}_{\kappa\mu\kappa\mu}(r,r)+\Re^{Q,(ff)}_{\kappa\mu\kappa\mu}(r,r)\right]+\rho^{Q,core}(r),\ \text{where}$$

$$\Re^{Q,(gg)}_{\kappa\mu\kappa\mu}(r,r')=\sum_{\lambda\lambda'}\int_{-\infty}^{E_F}dE\,g^{Q}_{\kappa\lambda\mu}(E,r)D^{Q}_{\lambda\mu\lambda'\mu'}(E)g^{Q}_{\kappa'\lambda'\mu'}(E,r'), \tag{2.18}$$

$$\Re^{Q,(ff)}_{\kappa\mu\kappa\mu}(r,r')=\sum_{\lambda\lambda'}\int_{-\infty}^{E_F}dE\,f^{Q}_{\kappa\lambda\mu}(E,r)D^{Q}_{\lambda\mu\lambda'\mu'}(E)\,f^{Q}_{\kappa'\lambda'\mu'}(E,r').$$

$D^{Q}_{\lambda\mu\lambda'\mu'}(E)$ are defined via the physical Green's functions [62]:

$$D^{Q}(E)=-\frac{1}{\pi}\operatorname{Im}\left\langle G\left(E+i0\right)\right\rangle^{Q}_{r'r},\quad D(E)=\sum_{Q}c^{Q}D^{Q}(E).$$

The spherical average of the spin density is given by

$$\begin{aligned}\tilde{\mathbf{m}}^{Q}(r)=\frac{1}{4\pi}\sum_{\kappa\mu}\sum_{\kappa'\mu'}\Big[&\Re^{Q,(gg)}_{\kappa\mu\kappa'\mu'}(r,r)\left\langle\kappa\mu\left|\boldsymbol{\sigma}\right|\kappa'\mu'\right\rangle\\ -&\Re^{Q,(ff)}_{\kappa\mu\kappa'\mu'}(r,r)\left\langle-\kappa\mu\left|\boldsymbol{\sigma}\right|-\kappa'\mu'\right\rangle\Big]+\tilde{\mathbf{m}}^{Q,core}(r).\end{aligned} \tag{2.19}$$

with $\langle \kappa\mu | \sigma_z | \kappa'\mu' \rangle$ defined in Equation (2.15). Potential functions, defined in (1.37), can also be rewritten in the framework of the fully relativistic CPA as potential matrices – for instance, the L^{th} block of γ and the C function are [62]

$$\begin{aligned}
&\gamma_L = \frac{1}{2(2l+1)}\left(\frac{s}{w}\right)^{2l+1}\left(D_L + A_L - l\right)\left(D_L + A_L + l + 1\right)^{-1},\\
&C_L = E_L I_2 + sg_L^{Tr} A_L g_L - sg_L^{Tr} A_L \left(D_L + A_L + l + 1\right)^{-1} A_L g_L^{Tr},\\
&D_L = scf_L g_L^{-1} - \kappa - I_2 \quad \text{with} \quad \kappa = \begin{pmatrix} \kappa_1 & 0 \\ 0 & \kappa_2 \end{pmatrix},\\
&\text{and } A_L = -\left(sg_L \dot{g}_L^{Tr}\right)^{-1},
\end{aligned} \tag{2.20}$$

where T denotes a transposed matrix, I_n is a $n \times n$ unit matrix, s is the muffin-tin radius. The global length scale w is usually taken to be an average MT radius, and therefore, if all the spheres are the same, $\frac{s}{w}$ equals to 1.

The changes explained here affect the dimensions and calculations of many functions and quantities throughout the calculation. For example, any change in Green's functions (new dimensions and hence additional terms while using them) affects the variables we calculate through them, such as susceptibility, magnetic exchange, etc. (which will be considered later in Chapter 4).

A linear augmented wave method has two parts: (1) an algorithm to calculate partial waves inside the augmentation spheres, and (2) a 'band' part that determines the charge density or some related quantity. Part (1) takes as its input a collection of moments of the charge density and boundary conditions (e.g. energies of the partial waves). In the linear method (which restricts the energy

dependence of partial waves to the solution ψ at some given energy and its energy derivative $\dot{\psi}$), the density is formed from the products of such waves. If one restricts the density to being spherical, there are only three possible products – $\psi\psi$, $\psi\dot{\psi}$, and $\dot{\psi}\dot{\psi}$ – for a given angular momentum. Thus, in the ASA which assumes a spherical potential, the knowledge of the zeroth, first, and second moments of the density is sufficient to self-consistently determine the potential inside the augmentation sphere. So, Part (1) takes as input these moments and generates as its output, the potential, partial waves, and parameters related to the scattering of these waves. Part (2), for a muffin-tin potential, requires only the information about the structure and the parameters related to the scattering of the partial waves at the MT boundary. It takes as input the output of Part (1) and generates as the output the moments that are the input of Part (1). The entire self-consistency cycle then alternates $1 \to 2 \to 1 \to ...$ Ref [51] provides all the changes to the parameters required in this process, as the Schrödinger equation is replaced with the Dirac equation.

The FR Dirac solver and all the other changes described above have been implemented within the electronic structure code Questaal [53], specifically its LMTO-ASA- and ASA-based density-functional Green's function branches. The latter calculates Green's functions and uses them to determine a number of properties including the density of states, energy band structure, and the magnetic moment. It is also used to calculate the magnetic exchange interactions and other properties of the linear response. The code can include spin-orbit coupling

perturbatively, and it has a fully relativistic Dirac formulation. It also implements the CPA.

Relativistic vs. non-relativistic results

Table 1 shows the total magnetic and orbital moments for several materials. All the calculations were performed by using the Questaal electronic structure code within the ASA and by using LMTO method. The calculations were made in two ways – by using the fully relativistic treatment and the scalar-relativistic method, including spin-orbit coupling. $(Ni_{80}Fe_{20})_{80}Cu_{20}$ and $(Ni_{80}Fe_{20})_{60}Cu_{40}$ occupying the last two lines are alloys and were calculated in CPA with the fully relativistic treatment.

Table 1 Orbital and magnetic moments calculated with the Dirac solver compared to the scalar-relativistic method, including spin-orbit coupling**.**

Material	$\mathbf{M_{Dirac}}$	$\mathbf{M_{nonrel}}$	$\mathbf{L_{Dirac}}$	$\mathbf{L_{nonrel}}$
Ni	0.6470	0.6070	-0.0587	-0.055
Fe	2.197	2.226	0.0467	0.0483
Co	1.6996	1.679	0.0961	0.0840
FePt	2.6019	2.588	**Fe** 0.0656 **Pt** -0.0421	**Fe** -0.084 **Pt** 0.0627
$\mathbf{(Ni_{80}Fe_{20})_{80}Cu_{20}}$	0.8313	0.7486		
$\mathbf{(Ni_{80}Fe_{20})_{60}Cu_{40}}$	0.5977	0.5421		

Table 2 shows the comparison between the SR and FR magnetic moments (total and orbital) of the transition metals bcc Fe, fcc Co, and fcc Ni, calculated in this thesis, and the moments for the same metals calculated within the FR generalization of the tight-binding LMTO [62], spin-polarized relativistic KKR [21], spin-polarized LMTO [52], and experiment values for the total moment [67].

Table 2 Magnetic moment (M) and orbital moment (M_l) for Ni, Fe, and Co (in μ_B per unit cell) from the present thesis (FR and SR), FR generalization of the tight-binding LMTO (FRTBLMTO) [62], spin-polarized relativistic KKR (SPRKKR) [21], spin-polarized LMTO (SPRLMTO) [52], and the experiment [67]

Transition metal	**Present thesis (FR)**	**Present thesis (SR)**	**FRTBLMTO [62]**	**SPRKKR [21]**	**SPRLMTO [52]**	**Exp. total moment [67]**
Ni (M)	0.647	0.607	0.689	0.619	0.616	0.616
Ni (M_l)	-0.059	-0.055	0.049	0.049	0.050	
Fe (M)	2.197	2.226	2.273	2.161	2.260	2.26
Fe (M_l)	0.047	0.048	0.043	0.069	0.049	
Co (M)	1.70	1.679	1.699	1.608	1.690	1.751
Co (M_l)	0.096	0.084	0.069	0.068	0.08	

The results of our calculations, performed with Questaal, agree quite well with those in Refs 21, 62, and 52. The differences may be due to the different types of exchange-correlation potentials used and other computational details.

The values for the moments do not change dramatically when treated within the fully relativistic approach in Questaal in comparison with those of the

scalar-relativistic calculations performed with the same code (up to 1-2% for Fe and Co, about 6% for Ni, 10% for the alloys [CPA]). The difference itself, when compared to the results obtained by other authors (Table 2), seems to be within the numerical error and numerical differences in implementation. In particular the linearization is carried out differently in the FR case. That the FR and SR moments are slightly different for these relatively light atoms is likely an artefact of the different treatment of the linearisation than has to do with errors in the scalar relativistic theory.

Conclusions

In order to account for the relativistic effects in crystals, we implemented the method proposed and developed by different authors [21, 48,51, 62] to solve the Dirac equation for the core and valence states' wavefunctions in the ASA-LMTO code Questaal. For the materials the fully-relativistic treatment was tested on, it did not lead to any considerable change in spin and orbital magnetic moments in comparison with the scalar relativistic case. The change observed can be attributed to the numerical differences in implementation, since it is similar to the discrepancies in the results obtained in the comparable implementations by other authors.

Following the examiners' remarks Table 1 has been amended when revisiting the issue after the dissertation was completed. The details and new values can be found in the Appendix and Table 14.

Chapter 3. Analysing $(Ni_{1-x}Fe_x)_{1-y}Z_y$, *Z=Cu, Cr, Mn,* and *Rh* materials with CPA

Experimental reasoning

Materials produced by doping and alloying are often used as magnets. Many of them are based on Cr, Mn, Fe, Co, and Ni as they exhibit characteristically large saturation magnetization values at room temperature [87].

However, there is a growing need for weak magnets with low saturation magnetization and a reduced Curie temperature for some applications in microelectronics, such as reducing the switching fields of the spin-toggle MRAM (where current I_c scales roughly proportional to M_s^2 [88]), or the development of a fast, dense, low-power cryogenic memory that uses Cooper pair transport though ferromagnetic free and fixed layers cladded by superconducting electrodes [87,89-91]. Hence, the reduction of the magnetic moment is also important to reduce the power consumption during the low temperature operation. It can also help to minimize the current-induced damage to the tunnel barriers that can limit the lifetime of today's room temperature spin torque MRAM devices [87].

It is possible to decrease the saturation magnetization and Curie temperature by diluting the magnetic elements with non-magnetic hosts. We use CPA calculations to investigate the change in the T_c and M_s of permalloy doped

with Cu, Cr, Mn, and Rh ($(Ni_{80}Fe_{20})_yZ_{1-y}$, $Z=Cu, Cr, Mn, Rh$) as well as changing the concentration of iron, trying to minimize the magnetization and Curie temperature while keeping the CPA-lifetime maximum, which is also important for its microelectronics applications. Here M_s can be tuned from 700 emu/cm^3 to 0, and the T_c can be adjusted from 900 K to 0 K by varying the alloy composition. The change in these values will be compared to the experimental data.

Apart from the Curie temperature and magnetization, we will try to decide on the best material by analysing the band structure (C-parameter, see (1.21), Chapter 1) that affects the alloy scattering and hence the lifetime. The reason for looking into it is the possible application of the materials we analyse in spintronic devices. For normal MRAM [93], just states at the Fermi level are important (minority spin). For JMRAM [89-91], Cooper pairs involve both majority and minority spin, so scattering in both channels must be considered.

It has been mentioned in Chapter 1 that the imaginary part of self-energy, introduced in (1.44) using the Green's functions, corresponds to the electron lifetime. The CPA method is a powerful technique for density-functional calculations in alloys, and it is based on using the configurationally averaged Green's functions (see Chapter 1). The Self-energy determines to what extent an electron 'feels' that configurationally averaged medium.

Calculational details

We have carried out electronic structure calculations for $(Ni_{80}Fe_{20})_yZ_{1-y}$, Z=Cu, Cr, Rh, and Mn alloys within the local density approximation using the

tight-binding linear muffin tin orbital basis and atomic sphere approximation [92]. To treat disorder, the Green's function approach was used in CPA. We adopt an approach similar to that of Turek et al. [75], except that we combine CPA with third-order potential functions [94].

The lattice constant used for the Cu-doped alloys was 3.57Å, taken from [95], reduced by 0.2%; the valence basis consisted of s-, p-, and d-orbitals. For the Rh- and Co-doped alloys, we used Vegard's law:

$$x_{NiFeRh} = 3.52 \cdot x_{Ni} + 3.62 \cdot x_{Fe} + 3.8 \cdot x_{Rh}$$
$$x_{NiFeCo} = 3.52 \cdot x_{Ni} + 3.62 \cdot x_{Fe} + 3.8 \cdot x_{Co}$$

CPA electronic band structure in doped permalloy

Electronic band structure calculations using CPA provide information about the electrical and magnetic properties of the permalloy-based alloys. Alloy scattering broadens the sharp quasiparticle levels; their width at the Fermi level is a direct measure of the alloy contribution to the scattering of states. In CPA, the broadening of a band by alloy scattering is given by the imaginary part of the self-energy at the quasiparticle peak (see (1.44)). Fig. 4 shows the broadening of the imaginary part of CPA self-energy for several concentrations of Cu (0%, 20%, and 40%) – one can see an apparent increase in scattering with increase in x. Below we will demonstrate that increase quantitatively based on the values of CPA-lifetime.

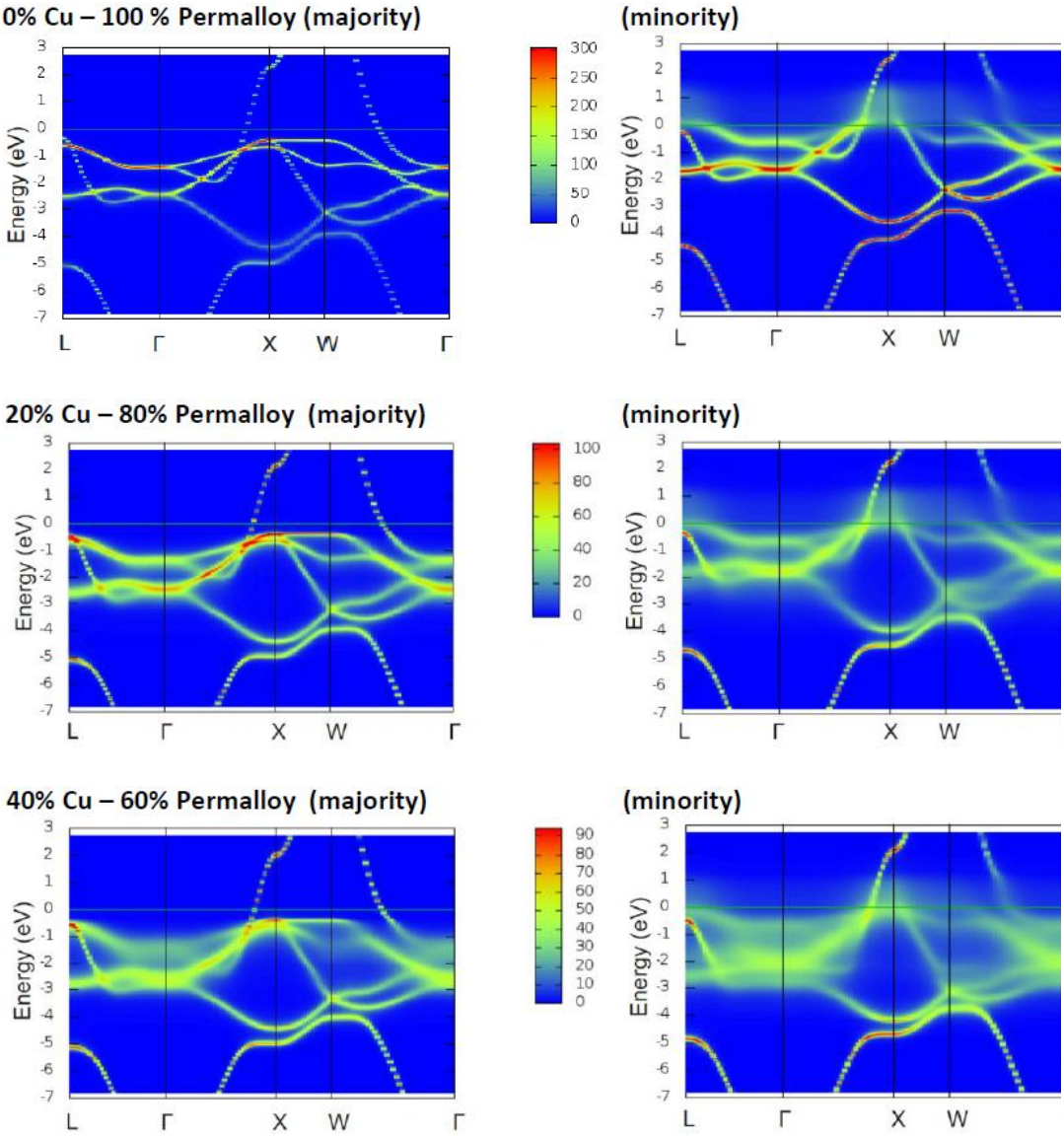

Fig. 4 Broadening of the imaginary part of CPA self-energy (colour bar, Ry) of majority (left) and minority (right) bands due to the alloy scattering for $(Ni_{80}Fe_{20})_xCu_{1-x}$. The width of the lines at the Fermi level (E = 0) is inversely proportional to the lifetimes of electron bands.

A number of studies show the band structure of pure permalloy [96-101]. Our results for the zero concentration of Cu are in good agreement with those studies. For pure permalloy, we see that the scattering in the majority channel is significantly smaller than in the minority channel. The weak scattering of the

majority carriers explains the small resistivity of the permalloy material. The presence of the strong scattering of minority carriers at and near the Fermi level has important implications for spintronic devices, as mentioned before.

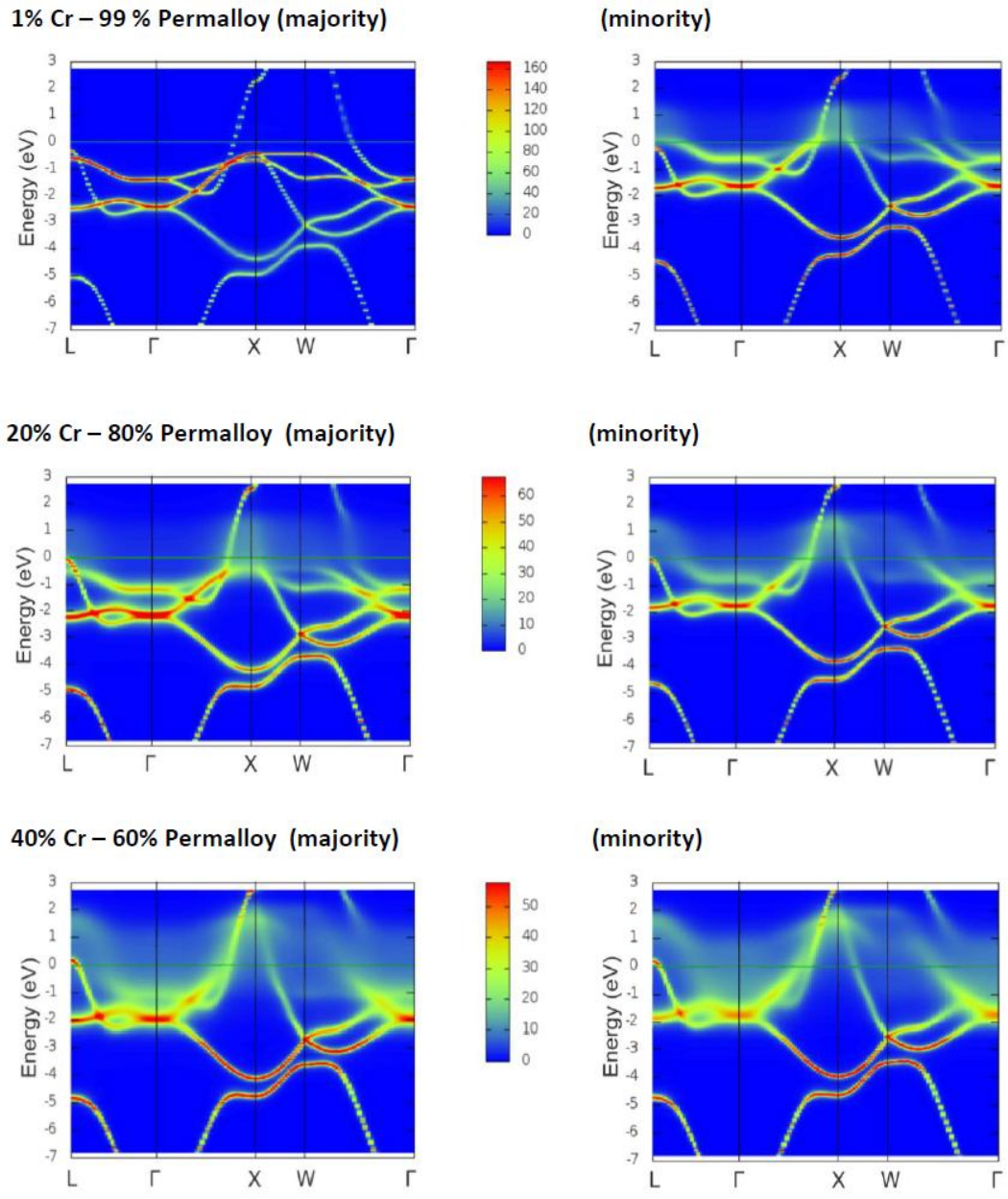

Fig. 5 Broadening of the imaginary part of CPA self-energy (colour bar, Ry) of majority (left) and minority (right) bands due to the alloy scattering for $(Ni_{80}Fe_{20})_xCr_{1-x}$. The width of the lines at the Fermi level (E = 0) is inversely proportional to the lifetimes of electron bands.

Fig. 5 shows the same calculations for the Cr-permalloy alloy. One can see from the figure in the case of Cr-doping that the minority as well as the majority channel gets noticeably distorted by the scattering. At the same time, the minority channel, even though broadened by the scattering even for the low concentrations of Cr, does not seem to be especially affected by the change in the dopant's concentration unlike the case of $(Ni_{80}Fe_{20})_xCu_{1-x}$ depicted in Fig. 4. This will be discussed further when the results obtained are compared to the experimental data.

The same calculations were performed for permalloy doped with Mn and Rh (see Fig. 6 and Fig. 7). Two cases were considered for Mn: permalloy alloyed with Mn, and the permalloy with the half of its iron replaced with Co in an attempt to lower the scattering (since Co is situated between Fe and Ni in the periodic table). Adding Mn instead of Cu/Cr by itself seems to decrease the scattering, while replacing some of the iron with Co improves it even more (though only for the minority channel).

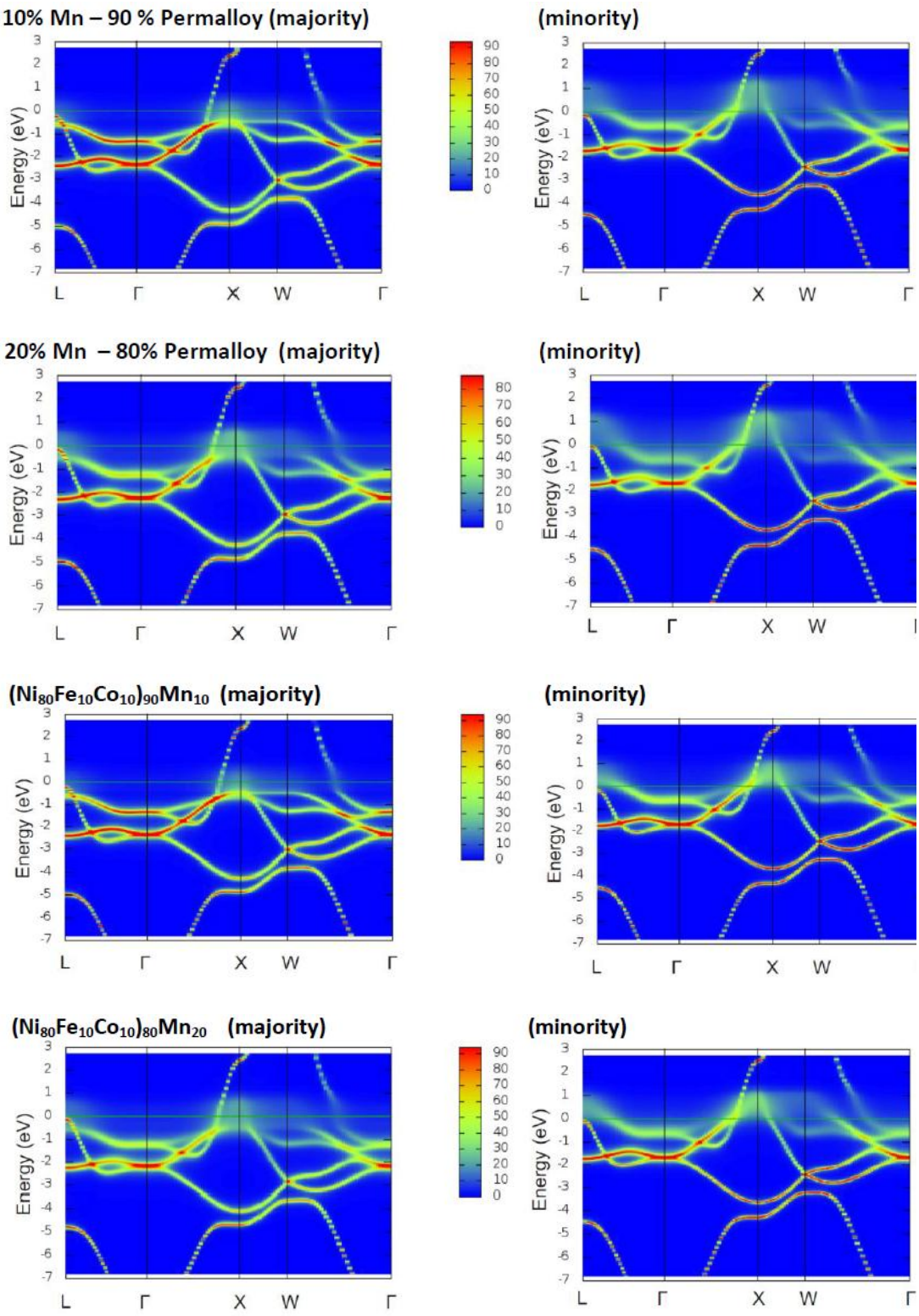

Fig. 6 Broadening of the imaginary part of the CPA self-energy (colour bar, Ry) of majority (left) and minority (right) bands due to the alloy scattering for $(Ni_{80}Fe_{20})_xMn_{1-x}$ and $(Ni_{80}Fe_{10}Co_{10})_xMn_{1-x}$ for *x=10* and *20%*.

Rh, on the other hand, seems to improve the scattering in the majority channel, even though the minority does not seem to improve much in comparison with Mn. It means that in terms of scattering, the best choice is to alloy permalloy with Rh to minimize the majority scattering and to replace some of the Fe with Co to do the same with the minority channel. The difference in scattering will be explained further with the analysis based on the so-called *C*-parameter.

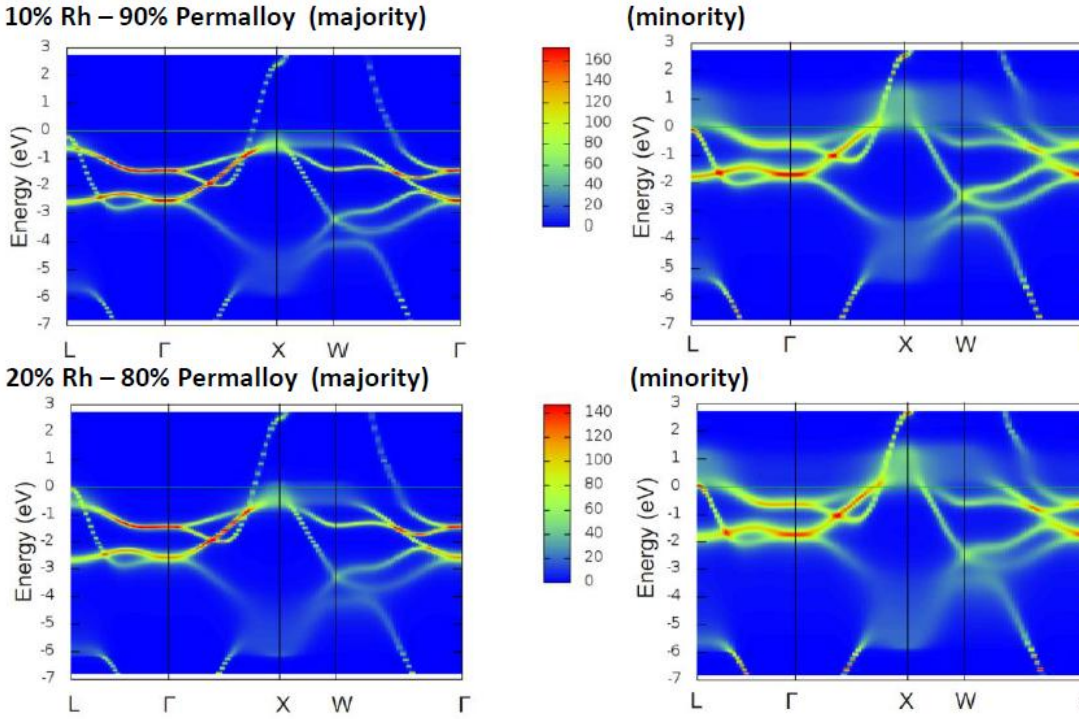

Fig. 7 Broadening of the imaginary part of the CPA self-energy (colour bar, Ry) of majority (left) and minority (right) bands due to the alloy scattering for $(Ni_{80}Fe_{20})_xRh_{1-x}$ for x=10 and 20%.

Analysis based on the *C*-parameter

As mentioned in Chapter 1, the *C* parameter, which we can extract from the CPA calculation, gives important information about the alloy scattering.

Potential parameters are introduced in detail in Chapter 1 for the C-parameter, see (1.21).

For example, looking at Fig. 8 with $C^{\uparrow}$ and $C^{\downarrow}$ for the $Cu_{1-x}(Ni_{80}Fe_{20})_x$ alloy's components, one can see that:

- The average value on a site, given by $(C^{\uparrow}-C^{\downarrow})/2$, is the deepest in Cu (*Z=29*), higher for Ni (*Z=28*), and considerably higher for Fe (*Z=26*). The average value of it on all sites is approximately independent of *x*.
- The spin splitting on the Fe site is robust and independent of *x,* since Fe has a strong local moment having only weak dependence on the environment.
- On the Ni site, the splitting depends on the Cu concentration. It is several times smaller than Fe-splitting because the local moment in Ni is smaller by a similar factor. Moreover, the splitting decreases with increase in x since adding Cu quenches the moment.
- On the Cu site, $(C^{\uparrow}-C^{\downarrow})/2$ is very small. Cu, with its filled *d*-shell, has almost no local moment.

The misalignment in *C* among the alloy constituents is the main source of scattering. Since it is strong, the other sources of scattering, such as spin-orbit coupling, are much weaker (the size of spin-orbit corrections to Hamiltonian shows that as well) and we can consider the spin channels to be almost independent. If we compare the mismatch in $C^{\uparrow}$ in the series Fe-Ni-Cu, we can

see that Ni is higher than both Fe and Cu. However, the mismatch is not as large as the one in the minority channel. For this reason, we expect the minority-channel lifetime to be much smaller than the majority, as we can see in Fig. 4.

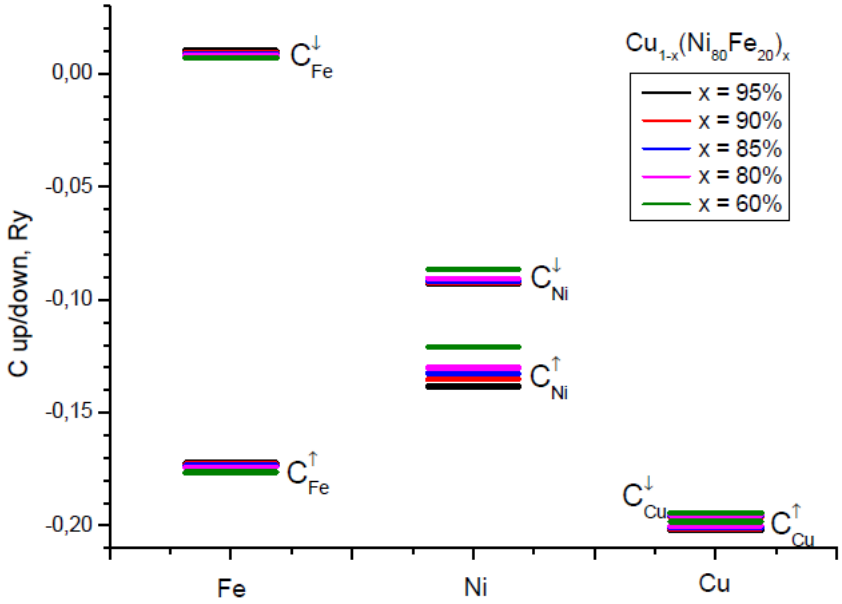

Fig. 8 Change with the doping of the potential parameter *C* representing the *d*-band centres of Fe, Ni, and Cu for majority (up) $C^{\uparrow}$ and minority (down) $C^{\downarrow}$ spin in permalloy-Cu alloys. The figure shows a large misalignment of the bands between alloy constituents causing strong scattering of the minority carriers at and near the Fermi level.

In Fig. 9 one can see almost the same mismatch in $(C^{\uparrow} - C^{\downarrow})/2$ between the alloy components. However, there is a smaller change in the $C^{\downarrow}$ - mismatch for Fe-Ni-Cr with the concentration of Cr in comparison with the majority spin (note that the mismatch for minority and majority spin between Ni and Cr is almost the same for *x=40%*, black arrows in **Fig. 9**). It explains the fact that the imaginary part of the CPA self-energy depicted in Fig. 5 does not broaden much for the minority spin (even though it looks much worse than the case of Cu even

for small concentrations of Cr) while showing a noticeable change in scattering for the majority spin.

Also, in contradistinction to the Cu-permalloy alloys, $(C^{\uparrow} - C^{\downarrow})/2$ is much larger on the Cr site, especially for low concentrations of Cr.

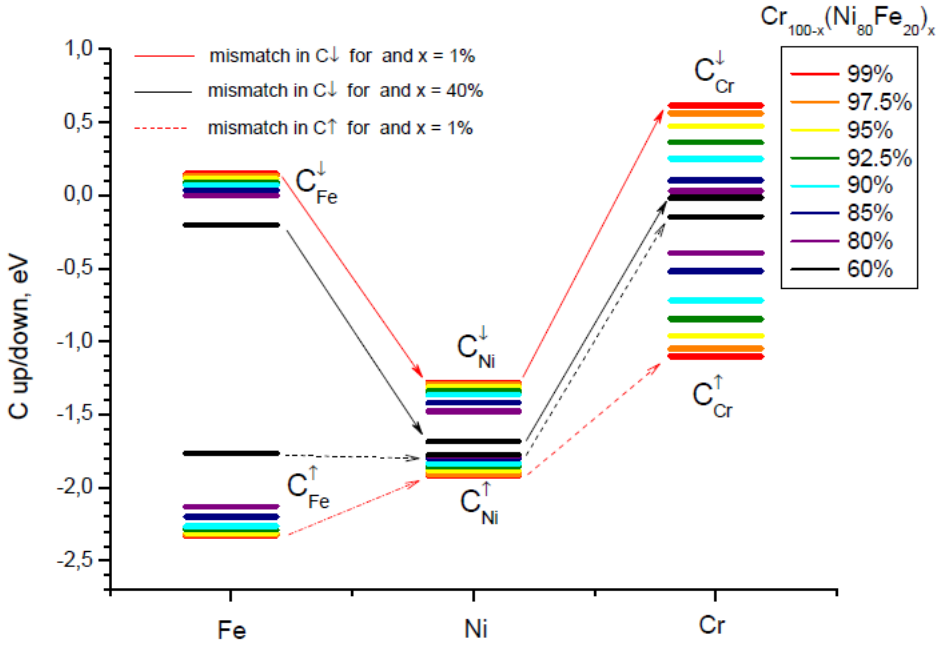

Fig. 9 Change of the potential parameter, C, representing the d band centres of Fe, Ni, and Cr for majority (up) and minority (down) spin with the concentration of Cr.

Fig. 10 shows the *C* parameter for permalloy-Mn alloys. Judging by the mismatch in the values of $C^{\uparrow}$ and $C^{\downarrow}$, we can see that the majority spin should not improve much over the Cr- and Cu-permalloy alloys, unlike the minority spin, which should show less scattering due to the lower-sitting Mn with $C^{\downarrow}_{Ni}$ much closer to $C^{\downarrow}_{Mn}$. Here we also replaced some of the Fe in the same with Co with the hope that Co, being closer to Ni in the periodic table would result in less alloy scattering (Fig. 11).

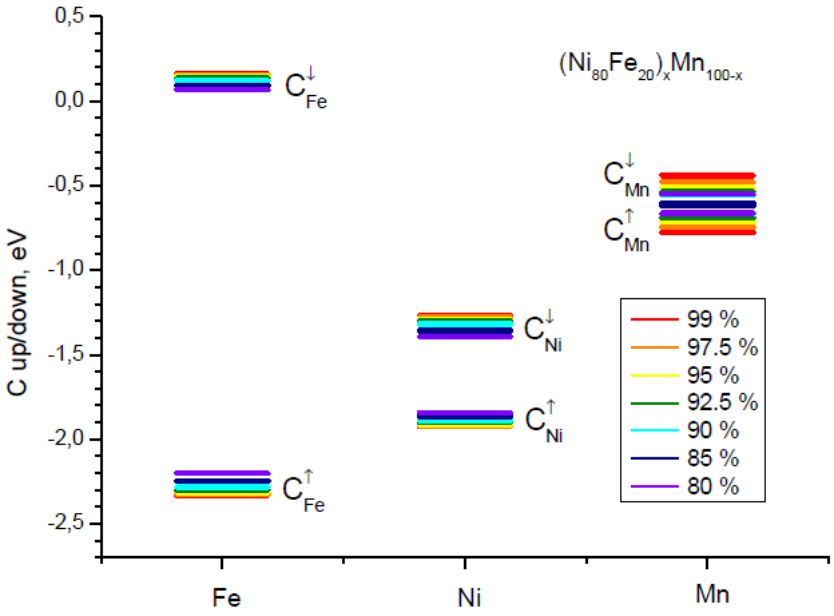

Fig. 10 Change of the potential parameter, C, representing the d band centres of Fe, Ni, and Mn for majority (up) and minority (down) spin with x in $(Ni_{80}Fe_{20})_xMn_{100-x}$.

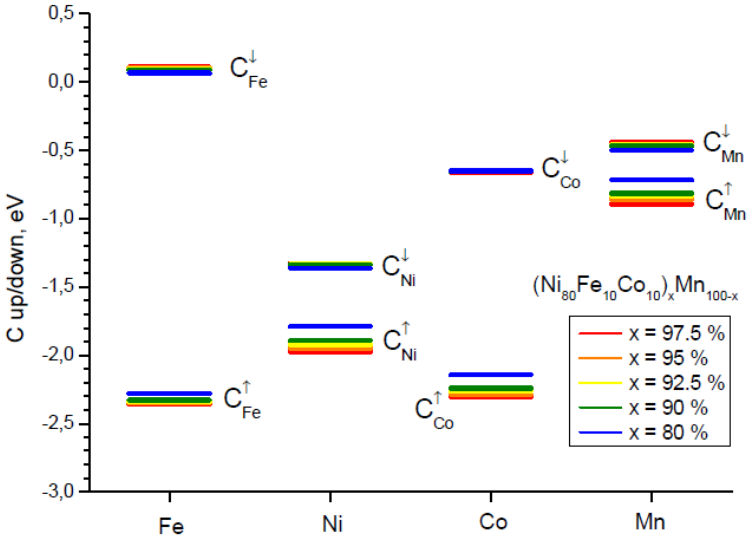

Fig. 11 Change of the potential parameter, C, representing the d band centres of Fe, Ni, Co and Mn for majority (up) and minority (down) spin with the concentration of Mn when Co is added to replace half of the iron in $(Ni_{80}Fe_{10}Co_{10})_xMn_{100-x}$.

The average value of C on a site, $(C^{\uparrow} - C^{\downarrow})/2$, in Co is much closer to Ni than the average value in Fe. It means that replacing as much of Fe with Co as

possible will minimize the scattering (experimentally, it has been proven to be technically difficult to replace all the Fe).

It looks like this change will especially improve the minority channel, which is the main problem in all the alloys we had looked into. Indeed, $C_{Co}^{\downarrow}$ is much closer to $C_{Ni}^{\downarrow}$ then the same parameter for the iron.

Finally, we tried another element – Rh in alloy with permalloy. The idea here was that even though it is situated in the next period of periodic table, its place is between Fe and Ni, and therefore, hopefully should be closer to them in terms of the average value of C.

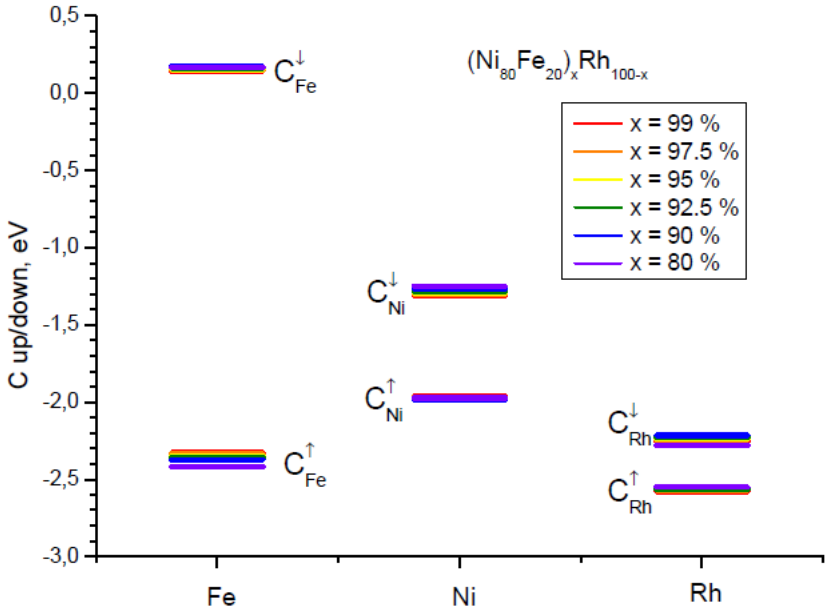

Fig. 12 Change of the potential parameter, C, representing the d band centres of Fe, Ni, and Rh for majority (up) and minority (down) spin with the concentration of Rh.

Fig. 12 shows that $(C^{\uparrow} - C^{\downarrow})/2$ in Rh is indeed closer to Ni than in all the elements considered previously. It is especially good in the case of $C^{\uparrow}$, and it

makes us hope that alloying permalloy with Rh should improve the lifetime and the MFP of the majority spin in the alloy.

CPA lifetime calculations

As we mentioned before, the imaginary part of the CPA self-energy Σ at the Fermi level gives us the spin lifetime due to alloy scattering (see Chapter 1, eq. (1.46)). To calculate the lifetime, the imaginary part of Σ is plotted as a function of energy at the line, perpendicular to the k-axis and crossing it where the pole in G crosses ε_F (see examples on **Fig. 13**. and **Fig. 14**). The peak width at the Fermi energy ($\varepsilon_F = 0$) is estimated by fitting the peaks and measuring the half-width (using **OriginPro**). The lifetime can be calculated by using the following formula $\tau = \frac{\hbar}{\Delta E}$.

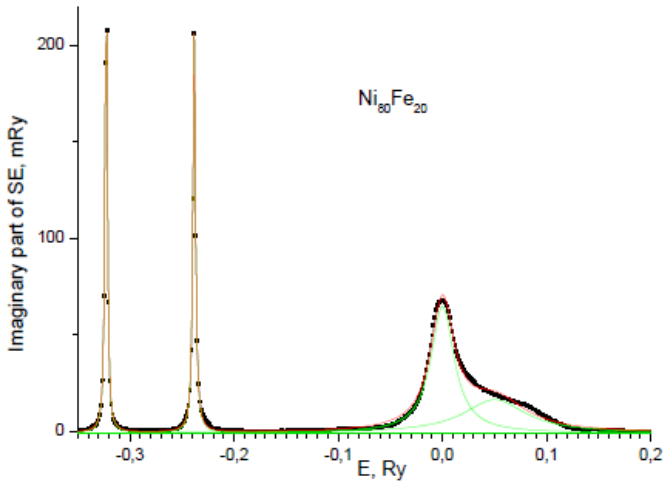

Fig. 13 Imaginary part of Σ vs energy for the k-point, where Σ crosses the Fermi energy for $Ni_{80}Fe_{20}$

We fitted the peaks with the Lorentzian shape as it seemed to reproduce the shape most closely, and there was some difficulty in distinguishing the peaks.

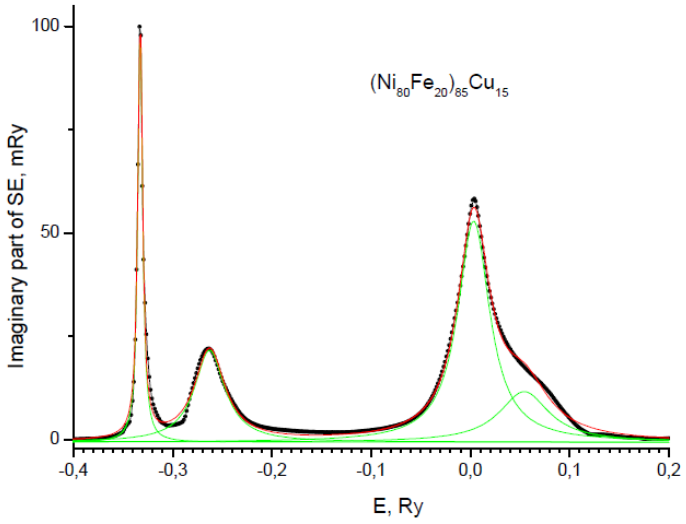

Fig. 14 Imaginary part of Σ vs energy for the k-point where Σ crosses the Fermi energy for $(Ni_{80}Fe_{20})_{85}Cu_{15}$

The procedure was repeated for different concentrations of Fe and Cu in $(Ni_{1-x}Fe_x)_{1-y}Cu_y$, and this allowed us to plot a graph showing the way the lifetime depends on x and y for both majority and minority spin (see Fig. 15).

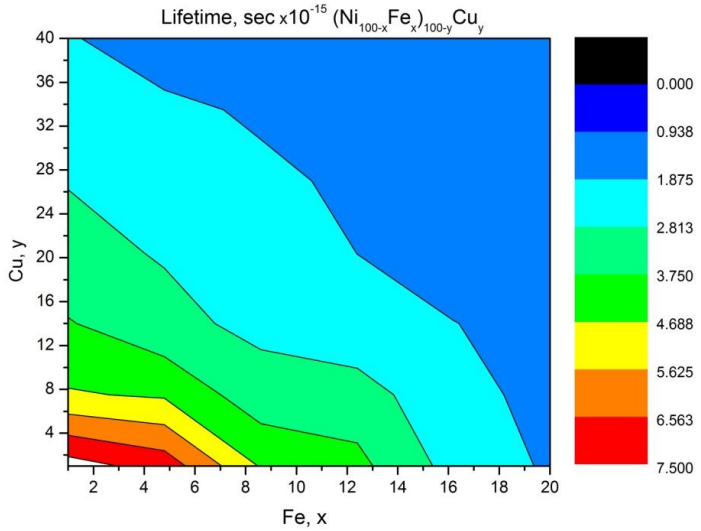

Fig. 15 Change in the CPA-lifetime (calculated for the points where Σ crosses the Fermi energy, see Fig. 4) of minority spin in $Cu_yNi_{1-x-y}Fe_x$

As one can see, the addition of Fe and Cu shortens the lifetime substantially, although the increase in the concentration of Fe (x-axis) seems to affect it faster than the increase in the concentration of Cu (y-axis). It means that to keep the scattering to a minimum, it would be a good idea to either decrease the concentration of iron or replace it with a more suitable element.

Table 3 shows us both lifetimes for spin up and spin down. The lifetime for the minority spin is considerably shorter and is more affected by the addition of Cu than the one for majority spin (it is also obvious from the width of the imaginary part of Σ (see Fig. 4)).

Table 3 The magnetization, lifetime (calculated for the points where Σ crosses the Fermi energy, see Fig. 4), and composition-weighted sum of exchange parameters determined from the LDA methods using LMTO and CPA formalisms [87].

Alloy	**M**	$\tau_{up} \times 10^{-15}$, sec	$\tau_{down} \times 10^{-15}$, sec	$\bar{J}_0$, mRy	J_0 Fe	J_0 Ni	J_0 Cu
$Ni_{99}Fe_1$	0.62	24.4	10.7	3.32	12.09	3.24	-
$Ni_{80}Fe_{20}$	1.00	23.5	1.78	5.28	11.19	3.80	-
$(Ni_{80}Fe_{20})_{80}Cu_{20}$	0.75	16.2	1.15	3.19	8.66	2.51	0.10
$(Ni_{80}Fe_{20})_{60}Cu_{40}$	0.54	13.0	0.97	2.00	6.73	1.86	0.06

Velocity at the Fermi surface

To determine the electron mean free path $\lambda = \upsilon_F \tau$, we need the velocity at the Fermi level which is defined as $\upsilon_F = \frac{1}{\hbar}\frac{dE}{dk}$, where $\frac{dE}{dk}$ is just a slope of the

band structure in Fig. 4-Fig. 7 where it crosses the Fermi energy. It is possible to find the slope from the spectral function data close to zero energy (Fermi energy). We can notice several things by looking at these figures. First, υ_F will be different for the minority and majority channels. Second, for the majority carriers, the line crosses ε_F twice, so we need to decide on the one to pick of the two. Third, for the minority carriers, several bands cross the Fermi energy at roughly the same place – this makes it difficult to decide on a single number for the velocity, especially with an increase in the dopant's concentration as the lines become wider.

For the majority carriers, we calculated the velocity at both points. After calculating the MFP, we have chosen the longest.

For the minority channel, we noticed that the shape of the bands (and hence the slope we are looking for) does not change with x (we also calculated the velocity for several concentrations to confirm it); it made us decide to find the slope for the low concentration (where the linewidth allows us to find the slope more precisely). Next, for the final number, we chose the average for all the three lines crossing the Fermi energy at the same point. The numbers we obtained and used further to find the MFP are: $\upsilon_F^{\uparrow} = 3.9\times10^5$ m/s, $\upsilon_F^{\downarrow} = 2.4\times10^5$ m/s (which is in reasonable agreement with dHvA data for pure permalloy [97]). These numbers may be used to obtain the spin mean free path.

Magnetization, lifetime, exchange interactions, and Curie temperature in $(Ni_{1-x}Fe_x)_{1-y}Z_y$, (Z=Cu, Cr, Mn, Rh)

Here we present the results obtained for the magnetization, Curie temperature, lifetime, and MFP due to layer-scattering for various dopants. Fig. 16 shows the change in the magnetization with concentrations of Cu, Mn, Rh, and Cr added to permalloy as well as for the Mn-permalloy alloy with half of the iron replaced by Co.

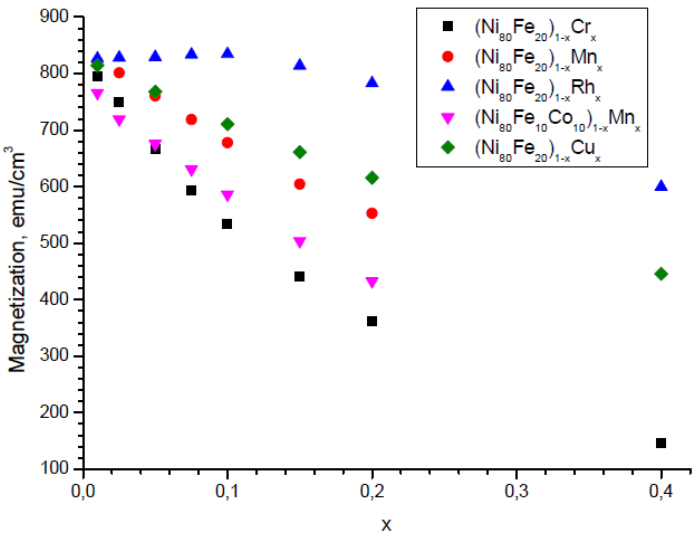

Fig. 16 Change in the magnetization of permalloy with the concentration of various dopants.

Keeping in mind that one of the main reasons for alloying permalloy with other elements was to decrease the magnetization, we can see that the best choice from this point of view will be Cr with Mn behind it. It is not surprising that replacing some of the Fe with Co quenches the moment as well, since iron is known to have a rather large magnetic moment. Adding Rh is the worst choice as it causes the increase magnetization for the concentration up to about 10% before leading to a decrease in it.

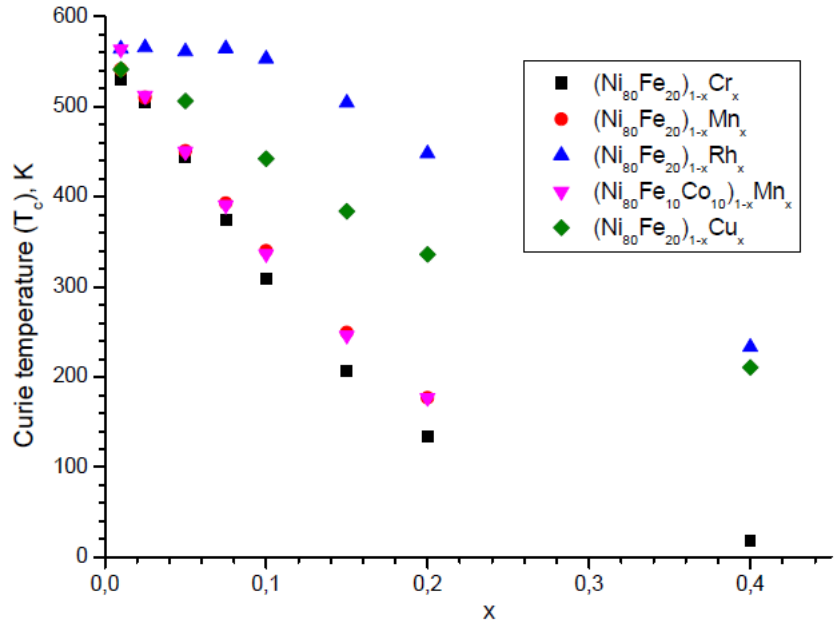

Fig. 17 Change in the magnetization of permalloy with the concentration of various dopants.

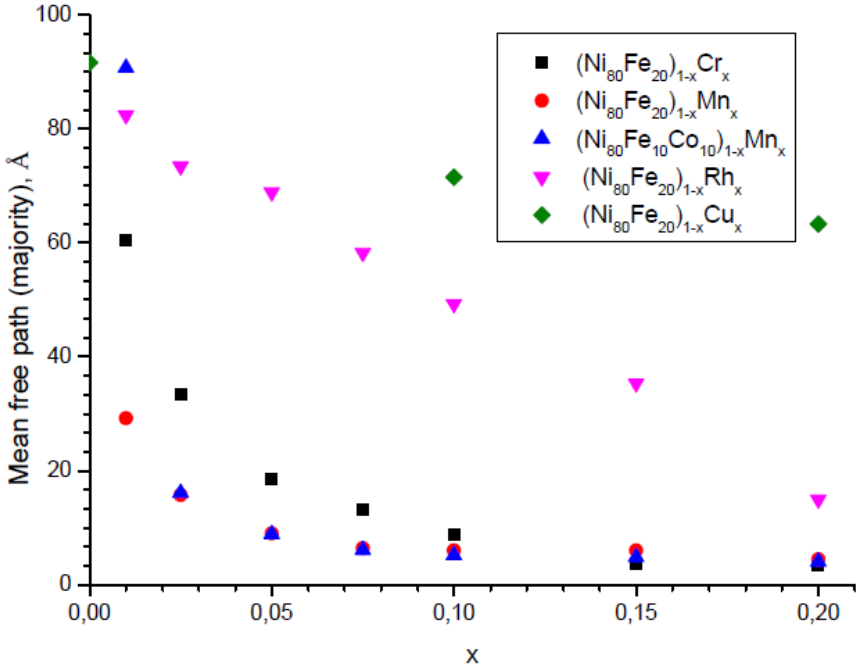

Fig. 18 Change in the MFP of majority carriers in permalloy with the concentration of various dopants (calculated for the two points where Σ crosses the Fermi energy, see Fig. 4).

Fig. 17 shows the change in the Curie temperature (obtained from the exchange J_0 as $2/3J_0$, where exchange interactions are calculated in accordance with the 'Lichtenstein formula' [98]) with the concentration of same dopants. To get the largest decrease in T_c with the dopant concentration, we need to choose Cr and Mn, while the Rh is again being the worst.

The width of the line at the Fermi surface for the majority carriers in Cu is lower than that in the rest of the alloys – this leads to a longer lifetime and longer MFT, which is why we do not include it in Fig. 18. Among the rest of the alloys, the longest MFP belongs to Rh, followed by Cr and Mn (addition of Co does not seem to affect it much).

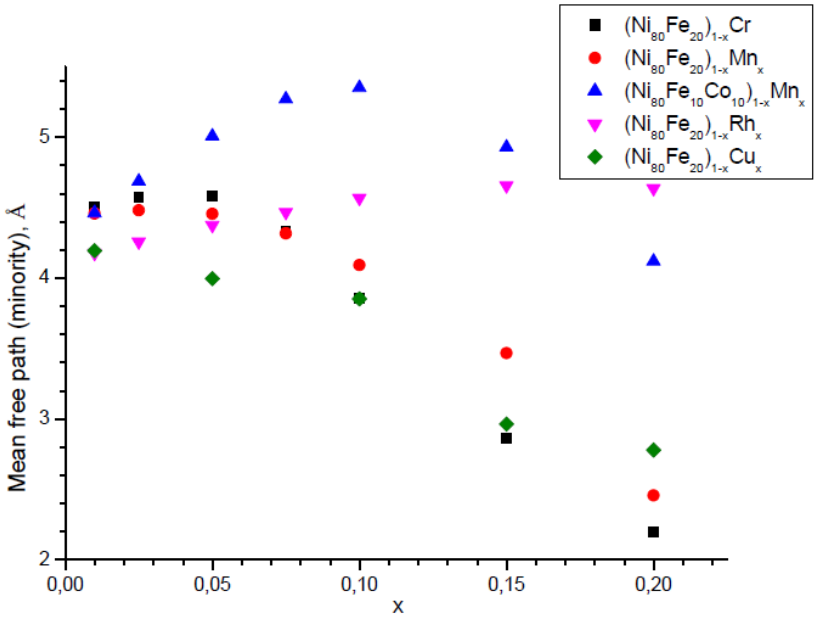

Fig. 19 Change in the MFP of minority carriers in permalloy with the concentration of various dopants (calculated for the two points where Σ crosses the Fermi energy, see Fig. 4).

Fig. 19 presents the same data for the minority carriers (here the situation with Cu is not that obvious which is why it is included in the presented data). Here the addition of Co obviously improves the MFP. The addition of Rh, even though it seems to be less fruitful for concentrations up to 5%, does not affect the minority MFP as much as the addition of Cu, Mn, and Cr.

Hence, based on the CPA calculations performed, we can conclude that to minimize the scattering, the best dopant choice is Rh. To minimize scattering in the minority channel, it is a good idea to replace some of the Fe with Co, though it does not really affect the majority channel. Cr seems to be a better choice than Cu, especially for the majority spin; it also does not shorten the MFP for the minority spin as much for higher concentrations of the dopant.

Unfortunately, from the point of view of maximum quenching of the magnetic moment, Rh is not as good as the rest of elements. The best choice here is Cr, which makes it the best addition all around. Replacing some of the Fe with Co (which is also possible with Cr as a dopant) should somehow improve the unfortunate scattering for the minority spin.

Since one can see that any decrease in the iron concentration seems to be fruitful, we decided to look into the properties of the $(Ni_{100-x}Fe_x)_{100-y}Cu_y$ alloys varying both *x* and *y*. Fig. 20 shows magnetization and Curie temperature variations with the concentrations of Cu and Fe. We can see that lowering the concentration of Fe not only improves the scattering, but also brings the moment down (which is not surprising knowing the large momentum of iron). This is very important in practical devices as the switching field scales approximately with the

total magnetic moment. We conclude that (1) substitution of Fe with Co is feasible to some extent and (2) reducing the total moment by adding Cr is the most efficient way to reach the desired total moment while minimizing the extra scattering included by the alloy elements.

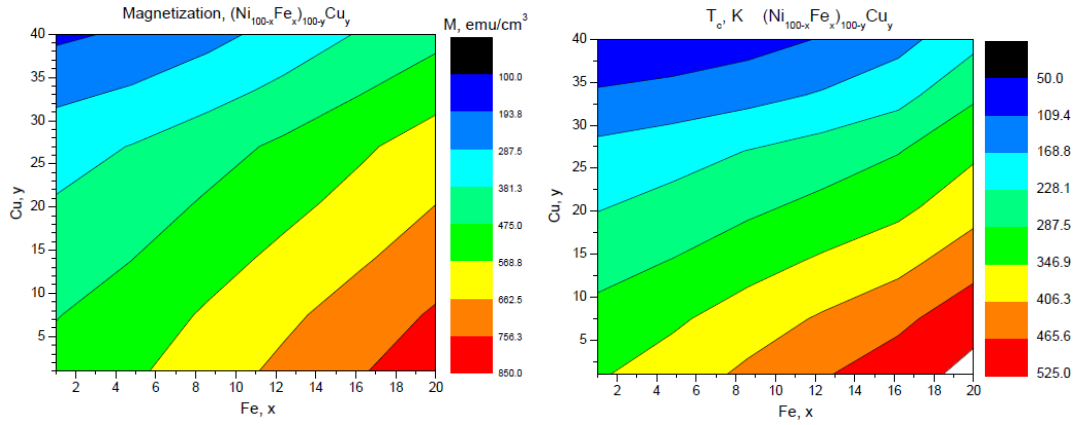

Fig. 20 Change in the a) magnetization, b) Curie temperature T_c with the variation in the Fe (x-axis) and the Cu (y-axis) content in $(Ni_{100-x}Fe_x)_{100-y}Cu_y$

Table 4 gives all available data for all the alloys with *x=10%* for the purpose of making comparisons. We highlighted the best (green) and the worst (red) result in each column (lowest M, longest MFP) for a better comparison. The second best is highlighted blue.

Table 4. The magnetization, Curie temperature, majority, and minority MFP for all the alloys with *x=10%*.

Alloy	M, emu/cm³	T_c, K	l_{maj}, Å	l_{min}, Å
$(Ni_{80}Fe_{20})_{90}Cu_{10}$	710.43	442.38	71.5	3.85
$(Ni_{80}Fe_{20})_{90}Cr_{10}$	534.00	309.52	8.74	3.85
$(Ni_{80}Fe_{20})_{90}Mn_{10}$	677.34	340.16	6.02	4.09
$(Ni_{80}Fe_{10}Co_{10})_{90}Mn_{10}$	585.96	336.35	5.14	5.35
$(Ni_{80}Fe_{20})_{90}Rh_{10}$	834.41	553.20	49.28	4.57

The table of the same data but for *x=20%* is also presented to show how all the numbers change with respect to each other if we increase the concentration (see **Table 5**). The best and the worst results are also highlighted (in green and red respectively).

Table 5. The magnetization, Curie temperature, majority, and minority MFP for all the alloys with *x=20%*.

Alloy	M, emu/cm³	T_c, K	l_{maj}, Å	l_{min}, Å
$(Ni_{80}Fe_{20})_{90}Cu_{10}$	615.49	336.04	63.3	2.78
$(Ni_{80}Fe_{20})_{90}Cr_{10}$	360.80	133.44	3.44	2.20
$(Ni_{80}Fe_{20})_{90}Mn_{10}$	552.45	176.96	4.43	2.46
$(Ni_{80}Fe_{10}Co_{10})_{90}Mn_{10}$	432.54	177.06	4.04	4.12
$(Ni_{80}Fe_{20})_{90}Rh_{10}$	782.69	447.98	14.97	4.64

Slater-Pauling curve

To look deeper into the magnetization results, the Slater-Pauling (SP) curve was plotted for all the compounds (Fig. 21). It shows the change of the mean magnetic moment as a function of the electron number per atom in the materials [99]. This curve is usually a broken line that goes up from the beginning of the 3d row of elements and goes down towards the end [100]. Many experimental pieces of data for 3d alloys lie on this curve, though there are some deviations from it. The spin magnetic moment per atom of a transition metal alloy is usually described within the rigid-band model (which assumes the s- and d-bands to be rigid in shape) as

$$\mu_S = (10 - n_d)\mu_B, \tag{3.1}$$

where $n_d = n_d^{\uparrow} + n_d^{\downarrow}$ is the d-band population [99]. The small orbital contribution is not included in this model.

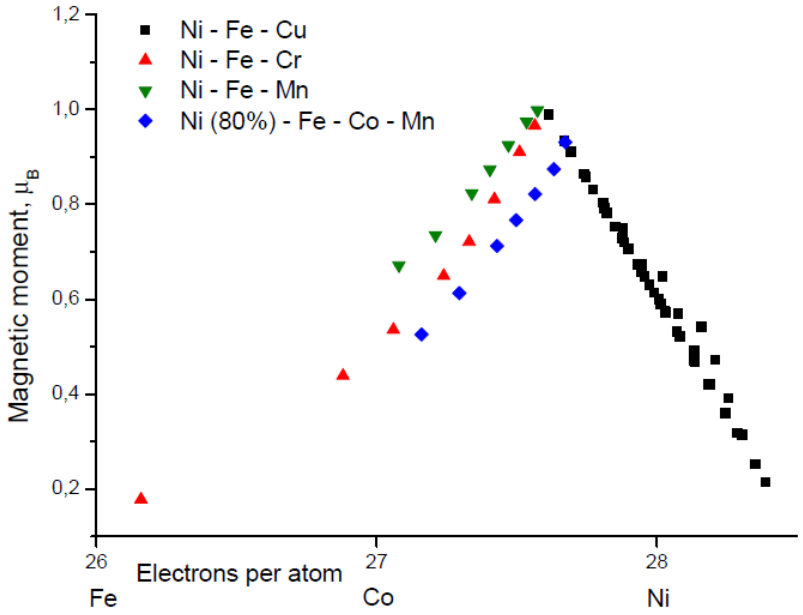

Fig. 21 The theoretical Slater-Pauling curve for $(Ni_{1-x}Fe_x)_{1-y}Z_y$, *(Z=Cu, Cr, Mn, Rh)* compounds

For strong ferromagnets, Equation (3.1) is a straight line with the slope equal to -1, and that is what can be seen in the curve plotted for $(Ni_{80}Fe_{20})_{1-x}Cu_x$ (Fig. 21, black squares). Table 6 shows the magnetic moments for Fe, Ni, and Cu sites, all of which have the same sign. If the data points are approximated by a straight line, at $e/a = 26$ that line reaches the magnetic moment equal to 2.55 μ_B which is close to the value of 2.7 μ_B (the magnetic moment of fcc γ-Fe).

For the rest of the alloys ($(Ni_{80}Fe_{20})_{1-x}Mn_x$, $(Ni_{80}Fe_{20})_{1-x}Cr_x$, and $(Ni_{80}Fe_{10}Co_{10})_{1-x}Mn_x$), however, the magnetic moment increases with the number of electrons per atom – this usually happens with the transition of an alloy to antiferromagnetism.

Table 6 The electron number per atom, mean magnetic moment, and magnetic moment pet each atom type for $(Ni_{80}Fe_{20})_{1-x}Cu_x$

x	0	0.2	0.4	0.5	0.7	0.8
e/a	27.6	27.88	28.16	28.3	28.58	28.72
$\mathbf{M_{tot}}$	1	0.75	0.54	0.44	0.22	0.11
$\mathbf{M_{Fe}}$	2.612	2.623	2.655	2.66	2.619	2.536
$\mathbf{M_{Ni}}$	0.597	0.507	0.447	0.401	0.231	0.066
$\mathbf{M_{Cu}}$	0.033	0.023	0.022	0.021	0.008	-0.004

Table 7 The electron number per atom, mean magnetic moment, and magnetic moment pet each atom type for $(Ni_{80}Fe_{20})_{1-x}Mn_x$

x	0.01	0.025	0.05	0.075	0.1	0.15	0.2
e/a	27.574	27.535	27.47	27.405	27.34	27.21	27.08
$\mathbf{M_{tot}}$	0.999	0.975	0.925	0.874	0.824	0.735	0.67
$\mathbf{M_{Fe}}$	2.62	2.61	2.59	2.56	2.53	2.47	2.39
$\mathbf{M_{Ni}}$	0.612	0.61	0.59	0.56	0.53	0.48	0.42
$\mathbf{M_{Mn}}$	-0.43	-0.34	-0.27	-0.21	-0.16	-0.05	0.09

Indeed, the values of magnetic moments per different sites (Table 7, Table 8, and Table 9) show that the dopant's magnetic moment (Mn and Cr) are directed opposite to the moments of Ni, Fe, and Co.

Table 8 The electron number per atom, mean magnetic moment, and magnetic moment pet each atom type for $(Ni_{80}Fe_{20})_{1-x}Cr_x$

x	0.01	0.025	0.05	0.075	0.1	0.15	0.2	0.4
e/a	27.56	27.51	27.42	27.33	27.24	27.06	26.88	26.16
$\mathbf{M_{tot}}$	0.966	0.91	0.81	0.72	0.65	0.54	0.439	0.178
$\mathbf{M_{Fe}}$	2.603	2.588	2.551	2.508	2.462	2.362	2.248	1.66
$\mathbf{M_{Ni}}$	0.593	0.578	0.535	0.486	0.44	0.355	0.278	0.082
$\mathbf{M_{Cr}}$	-1.922	-1.809	-1.616	-1.368	-1.108	-0.716	-0.493	-0.152

In ferromagnetic 'pure' Fe_xNi_{1-x} (without Cu, Mn or Cr), according to the results of neutron scattering measurements [99], the site-resolved magnetic moment of Fe increases from 2.2 μ_B to 2.6 μ_B, while the magnetic moment of Ni decreases from 1.0 μ_B to 0.6 μ_B with the increase in e/a. The same trend can be noted in the values of the magnetic moments of Fe and Ni in the ferromagnetic alloy $(Ni_{80}Fe_{20})_{1-x}Mn_x$, but it becomes opposite for Fe in $(Ni_{80}Fe_{20})_{1-x}Z_x$ (Z=Mn, Cr).

Table 9 The electron number per atom, mean magnetic moment, and magnetic moment pet each atom type for $(Ni_{80}Fe_{10}Co_{10})_{1-x}Mn_x$

x	0,01	0,025	0,05	0,075	0,1	0,15	0,2
e/a	27.673	27.633	27.565	27.498	27.43	27.295	27.16
$\mathbf{M_{to}}$	0,931	0,874	0,822	0,767	0,713	0,613	0,526
$\mathbf{M_{Fe}}$	2,5917	2,5925	2,5805	2,5653	2,5483	2,516	2,483
$\mathbf{M_{Ni}}$	0,608	0,605	0,584	0,556	0,527	0,466	0,405
$\mathbf{M_{Co}}$	1,668	1,67	1,656	1,637	1,616	1,573	1,527
$\mathbf{M_{Mn}}$	2,796	-0,546	-0,489	-0,451	-0,416	-0,345	-0,268

Comparison to experimental data

We also compared the CPA calculations with experimental data available for $(Ni_{80}Fe_{20})_{100-x}Cu_x$ [87]. The magnetic properties and magnetization of the films of the permalloy-Cu alloys were obtained using a vibrating sample magnetometer (VSM).

Fig. 22 shows the experimental data for the magnetization and the Curie temperature [87]. The data obtained numerically for different Cu concentrations is given in Fig. 23.

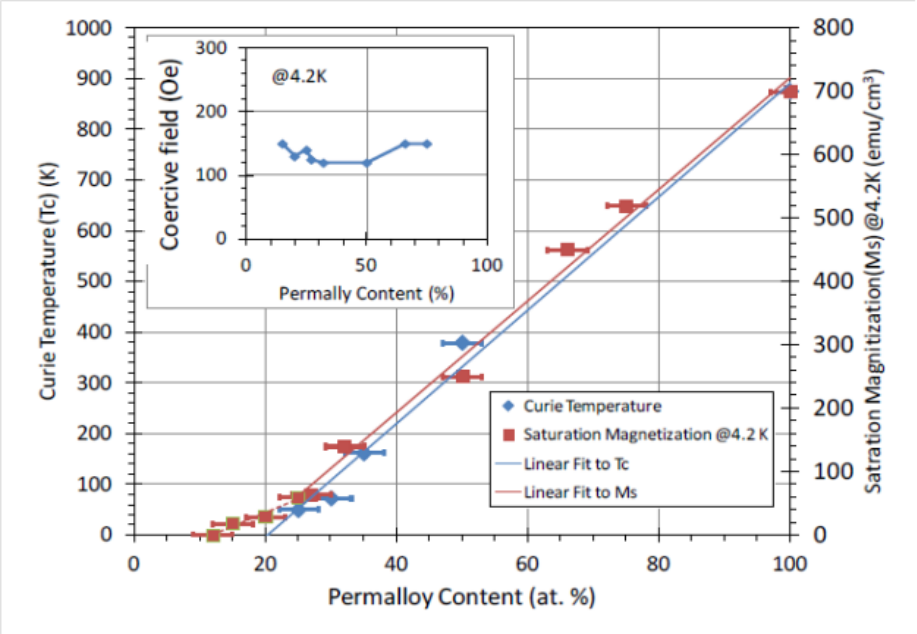

Fig. 22 The Curie temperature (T_c), saturation magnetization (M_s) at 4.2 K, and coercive field (H_c) dependencies on the permalloy content of $Cu_{1-x}(Ni_{80}Fe_{20})_x$ films.

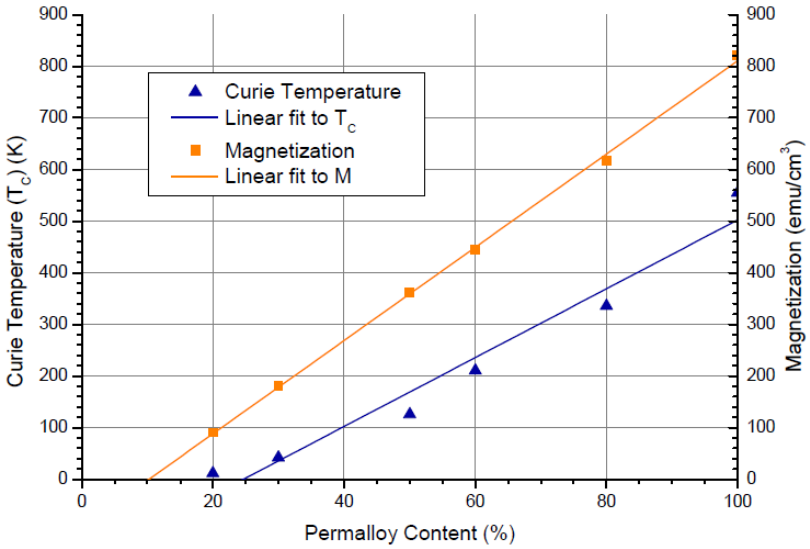

Fig. 23 The Curie temperature (T_c) and magnetization (M) dependencies on permalloy content of $Cu_{1-x}(Ni_{80}Fe_{20})_x$ obtained by CPA calculations.

The calculated magnetization tracks the experimental values reasonably well, though it is somewhat larger. The discrepancy with the experiment most

likely originates from the LDA's neglect of spin fluctuations, and it causes M to be overestimated [102].

The discrepancy in the value of the Curie temperature between measured and calculated values is a consequence of the fact that our estimate does not consider longitudinal spin fluctuations that reduce the magnetic moment in itinerant magnets. Indeed, in elemental Ni, for example, the average local moment approaches zero as $T \rightarrow T_c$, and only a rapidly fluctuating moment survives.

Apart from the experimental results for Cu-permalloy, we have some data for Cr-permalloy alloys [103]. Let's see how well our computational results compare to those. Fig. 24 shows the measured values of the quasistatic saturation magnetization of the Nb/Ru/$(Ni_{80}Fe_{20})_{100-x}Cr_x$/Ru/Nb films using a vibrating sample magnetometer for the samples of two different film thicknesses (2.5 nm and 11 nm) and two different temperatures (10 K and 300 K), as well as the experimentally-measured Curie temperature for various Cr concentrations. Theoretical calculations are also presented there.

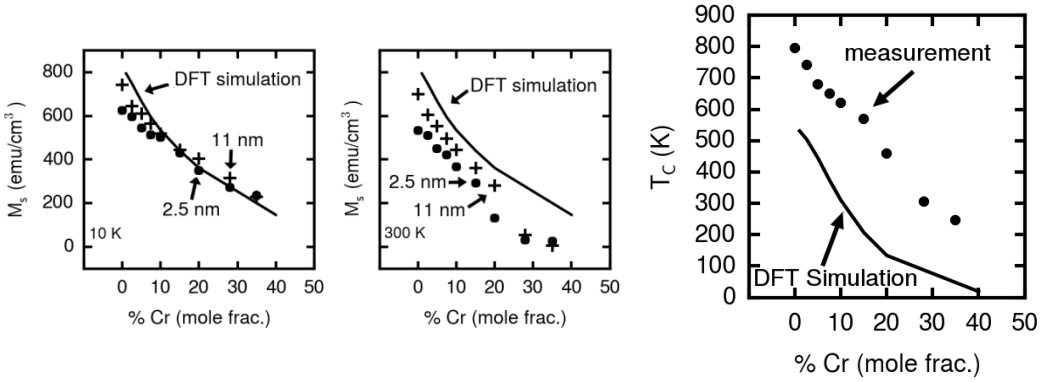

Fig. 24 Measured values for the quasistatic saturation magnetization of the Nb/Ru/$(Ni_{80}Fe_{20})_{100-x}Cr_x$/Ru/Nb films (a) and their Curie temperature dependence on the concentration of Cr (b). The lines represent CPA calculations [103].

As expected, the calculated magnetization (which is done for a model bulk material at 0 K) is in relatively good agreement with the data for the thicker 11 nm films measured at the lowest temperature of 10 K.

Just like Cu-permalloy, the calculated T_c has the same trend as the experimental result. However, the line itself is constantly below the experiment. This discrepancy is again attributed to the neglect of spin fluctuations and other dynamic effects not taken into account in our CPA calculations when using the Heisenberg model.

Here for Cr-permalloy, we have some lifetime experimental data for making comparisons as well (see Fig. **25**).

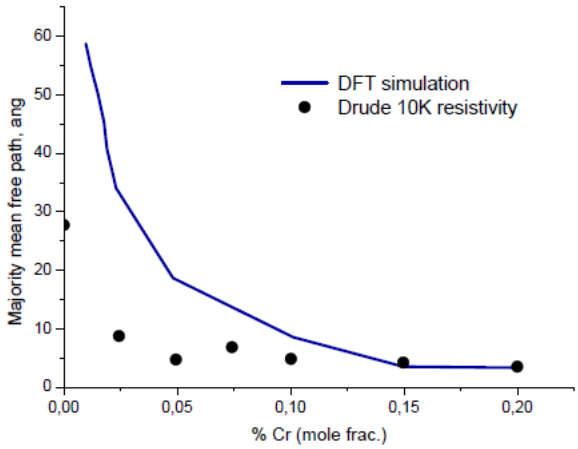

Fig. 25 Experimental values for majority carrier mean free paths with the values predicted using CPA [103].

Experimental values for the majority mean free path were calculated from the measured resistivities and the lattice constant using the Drude model [103,104]. Fig. **25** compares the experimental majority mean free paths with the

one calculated using the CPA. We can see good agreement at higher levels of the Cr content ($x > 0.15$), but not at lower levels where the calculations predict considerably longer MFP. This is surprising since the earlier studies have found alloy scattering to dominate in the scattering process in permalloy.

We also have some results for the carrier lifetime in Ni, Cu, and permalloy that we can calculate from the MFP and velocity at the FS obtained by angle-resolved photoemission in [97]: $\tau_{Ni} = 7\times10^{-15}\,\text{sec}$, $\tau_{Cu} = 1.58\times10^{-15}\,\text{sec}$, and $\tau^{\downarrow}_{Ni_{80}Fe_{20}} = 1.9\times10^{-15}\,\text{sec}$, $\tau^{\uparrow}_{Ni_{80}Fe_{20}} = 4.1\times10^{-15}\,\text{sec}$ for spin down and spin up respectively. The results we got for $(Ni_{80}Fe_{20})_{100-x}Cu_x$ seem to be of the order of these lifetimes.

Analysis and Conclusion

To summarize this chapter, we would like to stress the following points:

We used CPA to look into the magnetic properties of the permalloy alloyed with Cu, Mn, Rh, and Cr. We were trying to determine which one has the smallest magnetic moment and the Curie temperature along with the minimum alloy scattering for both minority and majority spin channels.

By comparing the experimental data for Cu-permalloy and Cr-permalloy, we can say that the CPA calculations seem to well represent the trend in the magnetic moment and the Curie temperature with some constant shifts due to the spin fluctuations not considered by the method used by us. However, it gives us confidence to use CPA for alloys in order to propose the better candidates to look into experimentally.

In terms of maximum quenching the magnetic moment, the best choice is Cr followed by Mn+Co, Mn, Cu, and Rh. We have almost the same sequence to minimize the T_c (only Mn and Mn+Co seem to have the same T_c).

We looked into the Rh-permalloy alloy in the hope to minimize the scattering due to alloy components. Indeed, it does have the longest MFP for the minority carriers and comparatively good one for the minority carriers. However, it will still require a large concentration to take down the magnetic moment, and that seems to make it less useful for the purpose.

The Cr-permalloy quenches the moment faster than the rest of the alloys. Hence, we need a smaller amount of Cr to decrease the moment to the same number, and smaller x means longer MFP, even though it has the shortest minority carriers' MFP; the majority MFP here seems to decrease faster than in other alloys. Judging by the improvement in the minority MFP due to the replacement of some of the Fe with Co, we would advise others to do it to the Cr-doped permalloy to further improve the minority MFP.

Mn-doping is not as good as doping with Cr, although it does improve the MFP a little. A good idea here again was to replace some of the Fe with Co to improve the minority MFP and further quench the magnetic moment.

With all the analysis done above, Cr-permalloy alloys seem to be the best choice for the experimental demands, especially if there is a way to replace some of the Fe with Co.

Cu- and Cr-permalloy calculations were partially compared to the experimental data and seem to be in reasonably good agreement with it. Most of

the discrepancies can be attributed to the fact that our CPA analysis does not consider spin fluctuations and other dynamic effects.

Chapter 4. Magnetic exchange and Susceptibility

Magnetic exchange interactions

One of the main reasons for using Green's functions is a straightforward way of obtaining response functions (e.g. susceptibility, exchange, etc) from them. They are especially useful while calculating susceptibility as it is just a product of two GFs.

The magnetic susceptibility of a material is a quantity that measures its response to an applied magnetic field. It is defined as [113]:

$$\vec{M} = \chi \vec{H} \tag{4.1}$$

where $\vec{M}$ is the magnetic moment per unit volume (magnetization density) and $\vec{H}$ is the applied field. Susceptibility is a scalar for magnetically isotropic materials and a tensor for anisotropic materials.

In a crystal in terms of the Heisenberg model, when we consider the crystal to be a system of localized rigid spins, the exchange integrals J_{ij} are the coefficients in the exchange Hamiltonian:

$$H = -\sum_{ij} J_{ij} \hat{S}_i \hat{S}_j \tag{4.2}$$

where $S_{i,j}$ are the operators of spins, i and j refer to the sites of a lattice; for spin $s = 1/2$ they are Pauli matrices. Hence, J_{ij} represent the energy required to turn a

spin with respect to another. The knowledge of exchange interaction parameters is quite important when describing the properties of magnets. There are several approaches for evaluating these parameters [107, 108, 109, 110]. The use of multiple scattering theory (MST) in a rigid spin approximation (RSA) for calculating J_{ij} becomes especially convenient if Green's functions are used. For the collinear magnetic structures ($S \parallel z$), we need to use the following formula [111,112]:

$$J_{ij} = \frac{1}{\pi} \int^{\varepsilon_F} d\varepsilon \, \mathrm{Im}\,\mathrm{Tr}\left\{ p_i T_{ij}^{\uparrow} \, p_j T_{ji}^{\downarrow} \right\} \tag{4.3}$$

for a two-site rotation. Here T_{ij} is Green's function and p_i is the potential parameter generated in LMTO (see Chapter 1). Since the formula includes Green's functions, the values of the exchange should be affected by its calculation in the relativistic case. For a one-site rotation, we have:

$$J_i = \frac{1}{\pi} \int^{\varepsilon_F} d\varepsilon \, \mathrm{Im}\,\mathrm{Tr}\left\{ p_i T_{ii}^{z} + p_i T_{ii}^{\uparrow} \, p_i T_{ii}^{\downarrow} \right\}. \tag{4.4}$$

The equation for susceptibility is even easier to implement, since in this case it is just a product of two Green's functions, at least for the case of the spin-spin part of susceptibility.

Magnetic exchange calculation in CPA

Vertex

In the CPA case, the formulas we are using to calculate exchange interactions must change [85, 86]. Let's look at the formula for pair-exchange, but

for the two atoms types *a* and *b* at the sites *i* and *j* (configuration average of the exchange interaction):

$$J_{ij}^{ab} = \frac{1}{4\pi}\,\mathrm{Im}\int^{\varepsilon_F} w_{ij}^{ab}\,dz = \frac{1}{4\pi}\,\mathrm{Im}\int^{\varepsilon_F} dz\,\mathrm{Tr}\left[\left(p^{\uparrow}-p^{\downarrow}\right)_i^a g_{ij}^{ab\uparrow}\left(p^{\uparrow}-p^{\downarrow}\right)_j^b g_{ji}^{ba\downarrow}\right]. \qquad (4.5)$$

In this case, g_{ij}^{ab} is a conditionally averaged Green's function of this kind of system. To use the real space representation of Green's function for the homogeneous CPA medium g_{ij} ($g(\mathbf{k}) = \left[p - S(\mathbf{k})\right]^{-1}$), we should replace g_{ij}^{ab} with

$$g_{ij}^{ab\sigma} = \left[1 + g_{ii}^{\sigma}\left(p_i^{a\sigma} - p_i\right)\right]^{-1} g_{ij}^{\sigma}\left[1 + \left(p_j^{b\sigma} - p_j\right) g_{jj}^{\sigma}\right]^{-1} \qquad (4.6)$$

g_{ii} is an on-site Green's function.

If we substitute Equation (4.6) with Equation (4.5) and factorize the expression, one will get

$$J_{ij}^{ab} = \frac{1}{4\pi}\,\mathrm{Im}\int^{\varepsilon_F} d\varepsilon\,\mathrm{Tr}\left\{\gamma_{ai}^{\downarrow\uparrow} g_{ij}^{\uparrow}\gamma_{bj}^{\uparrow\downarrow} g_{ji}^{\downarrow}\right\} \qquad (4.7)$$

with

$$\gamma_{ai}^{\sigma\rho} = \left[1 + \left(p_{ai}^{\sigma} - p_i^{\sigma}\right) g_{ii}^{\sigma}\right]^{-1}\left(p_i^{a\uparrow} - p_i^{a\downarrow}\right)\left[1 + g_{ii}^{\sigma}\left(p_{ai}^{\rho} - p_i^{\sigma}\right)\right]^{-1}. \qquad (4.8)$$

For convenience, it can also be rewritten as

$$\gamma_{ai}^{\sigma\rho} = \left(g_{ii}^{\sigma}\right)^{-1} g_{ai}^{\sigma}\left(p_i^{a\uparrow} - p_i^{a\downarrow}\right) g_{ai}^{\rho}\left(g_{ii}^{\rho}\right)^{-1} \qquad (4.9)$$

if we use $g_{ii} = \left(p_i - \Omega_i\right)^{-1}$ and $g_{ai} = \left(p_i^a - \Omega_i\right)^{-1}$, where g_{ai}^{σ} is Green's function for the atom *a*. These formulas are valid for the collinear case only.

Vertex for a non-collinear case

Non-collinearity of spins might be quite important due to the spin-orbit coupling [114] and spin-spin interactions in the non-relativistic case [115,116]. In the non-collinear case, we have to use all $g^{\sigma\gamma}$ with $\sigma,\gamma=\uparrow,\downarrow$, not only $g^{\uparrow\uparrow}$ and $g^{\downarrow\downarrow}$. The terms p_x and p_y are also required, not only $p_z=\frac{1}{2}\left(p^{\uparrow}-p^{\downarrow}\right)$. Hence, we will need terms of the form

$$w_{abij}^{\sigma\gamma nm,\alpha\beta}=\mathrm{Tr}\,p_{ai}^{\alpha}\left[1+g_{ii}^{\sigma\gamma}\left(p_{ai}^{\sigma\gamma}-p_{i}^{\sigma\gamma}\right)\right]^{-1}g_{ij}^{\sigma\gamma}\left[1+\left(p_{aj}^{\sigma\gamma}-p_{j}^{\sigma\gamma}\right)g_{jj}^{\sigma\gamma}\right]^{-1}p_{bj}^{b}\cdot \left[1+g_{jj}^{mn}\left(p_{bj}^{mn}-p_{j}^{mn}\right)\right]^{-1}g_{ji}^{mn}\left[1+\left(p_{ai}^{mn}-p_{i}^{mn}\right)g_{ii}^{mn}\right]^{-1}, \tag{4.10}$$

where $\alpha,\beta=x,y,z$. Separating the *i*- and *j*-terms again, we get

$$w_{abij}^{\sigma\gamma mn}=\mathrm{Tr}\,\gamma_{ai}^{n\sigma}g_{ij}^{\sigma\gamma}\gamma_{bj}^{\gamma m}g_{ji}^{mn}, \tag{4.11}$$

with

$$\gamma_{ai}^{\sigma\gamma mn,\alpha}=p_{ai}^{\alpha}\left[1+g_{ii}^{\sigma\gamma}\left(p_{ai}^{\sigma\gamma}-p_{i}^{\sigma\gamma}\right)\right]^{-1}\left[1+\left(p_{ai}^{mn}-p_{i}^{mn}\right)g_{ii}^{mn}\right]^{-1}, \tag{4.12}$$
$$\gamma_{bj}^{\sigma\gamma mn,\beta}=\left[1+\left(p_{bj}^{\sigma\gamma}-p_{j}^{\sigma\gamma}\right)g_{jj}^{\sigma\gamma}\right]^{-1}p_{bj}^{\beta}\left[1+g_{jj}^{mn}\left(p_{bj}^{mn}-p_{j}^{mn}\right)\right]^{-1}.$$

Results

After implementing the Dirac equation, we can see how much it affects the results (see Table 10). Again, same as in Chapter 2, we can see that it changes the exchange integrals for the light elements only slightly, but seems to be quite important for the heavy ones and in the CPA case.

Table 10 One-site exchange coupling constants (4.4) calculated with the Dirac solver compared to the non-relativistic case (including SO coupling)

Material	J_{nonrel}, mRy	J_{Dirac}, mRy
Ni	3.443	3.544
Fe	9.103	9.385
FePt	**Fe** 4.003 **Pt** 6.217	**Fe** 5.761 **Pt** 5.205
$(Ni_{80}Fe_{20})_{80}Cu_{20}$	**Fe** 8.662 **Ni** 2.510 **Cu** 0.096 **alloy** 3.011	**Fe** 10.744 **Ni** 4.282 **Cu** 0.537 **alloy** 4.567

Conclusions

We used the Green's functions calculated in the relativistic case (the method described in Chapter 2) to compute the exchange integrals and susceptibility. The formulas for exchange interactions, given in [111,112], were rewritten for both relativistic and CPA cases. It was demonstrated that consideration of relativistic effects while calculating those response functions affects their values considerably.

Chapter 5. Spin-wave lifetime

Calculation

To finalize our analysis of the materials from the previous chapter, we would like to look into one more quantity, namely the spin-wave lifetime. We would like to know if it is shorter and hence more important than the scattering lifetime. Another reason for calculating the lifetime is that it can be constructed using the Green's functions and potential parameters mentioned before, and since we now have the relativistic versions of both, we can calculate the lifetime more carefully. The method of describing spin-wave decay is given in [105]. We will follow the same route, but unlike the case in [105] we will consider the potential parameters to be complex numbers as they are in our calculations.

One should start with the expression for exchange parameters:

$$J_{ij} = \frac{1}{\pi}\int^{\varepsilon_F} d\varepsilon \,\mathrm{Im}\,\mathrm{Tr}\left\{ p_i T_{ij}^{\uparrow} p_j T_{ji}^{\downarrow} \right\}, \tag{5.1}$$

see Chapter 4 and [118,119] for the notations.

The poles of the T-matrix ($\varepsilon = \varepsilon_\nu$) define the spectrum of a system [105]. It is imaginary and the real parts can be written as

$$\mathrm{Im}\,T_{ij}^{\sigma} = -\pi \sum Z_{ij}^{\nu\sigma} \delta\left(\varepsilon - \varepsilon_{\nu\sigma}\right); \tag{5.2}$$

$$\mathrm{Re}\,T_{ij}^{\sigma} = \sum \frac{Z_{ij}^{\nu\sigma}}{\varepsilon - \varepsilon_\nu}, \tag{5.3}$$

where Z is a matrix over L,L'; the second formula is the Kramers-Kronig relation. We need to express the imaginary part of the product $p_i T_{ij}^{\uparrow} p_j T_{ji}^{\downarrow}$ in terms of the real and imaginary parts of p and T. The term we are interested in is:

$$\left(\mathrm{Re}\, p_i \,\mathrm{Re}\, p_j - \mathrm{Im}\, p_i \,\mathrm{Im}\, p_j\right)\left(\mathrm{Re} T_{ij}\,\mathrm{Re} T_{ji} - \mathrm{Im} T_{ij}\,\mathrm{Im} T_{ji}\right). \tag{5.4}$$

Let's rewrite Equation (5.1) by using expressions (5.2) and (5.3)

$$\begin{aligned} J_{ij} = \sum_{\nu\nu'} \mathrm{Tr}\left(p_i Z_{ij}^{\nu\uparrow} p_j Z_{ji}^{\nu'\downarrow}\right) \int^{\varepsilon_F} d\varepsilon \left\{ \frac{\delta(\varepsilon - \varepsilon_{\nu'\downarrow})}{\varepsilon_{\nu\uparrow} - \varepsilon} + \frac{\delta(\varepsilon - \varepsilon_{\nu\uparrow})}{\varepsilon_{\nu'\downarrow} - \varepsilon} \right\} = \\ \sum_{\nu\nu'} \mathrm{Tr}\left(\mathrm{Re}\, p_i(\varepsilon_{\nu\uparrow}) Z_{ij}^{\nu\uparrow}\, \mathrm{Re}\, p_j(\varepsilon_{\nu'\downarrow}) Z_{ji}^{\nu'\downarrow}\right) \frac{f_{\nu\uparrow} - f_{\nu'\downarrow}}{\varepsilon_{\nu'\downarrow} - \varepsilon_{\nu\uparrow}}. \end{aligned} \tag{5.5}$$

where $f_{\nu\sigma}$ is the Fermi distribution function. In the case of frequency dependence, it has been shown [117] that to find the spin-wave spectrum, we need the Fourier transform of the exchange integral:

$$\begin{aligned} J(\mathbf{q},\omega) = \sum_{nn'} \sum_{k} \frac{f_{n\uparrow}(\mathbf{k}) - f_{n'\downarrow}(\mathbf{k}+\mathbf{q})}{\varepsilon_{n'\downarrow}(\mathbf{k}+\mathbf{q}) - \varepsilon_{n\uparrow}(\mathbf{k}) + \omega + i0} \mathrm{Tr} \times \\ \left(p(\varepsilon_{n\uparrow}(\mathbf{k})) Z^{n\uparrow}(\mathbf{k})\, p(\varepsilon_{n'\downarrow}(\mathbf{k}+\mathbf{q})) Z^{n'\downarrow}(\mathbf{k}+\mathbf{q}) \right). \end{aligned} \tag{5.6}$$

In the equation of motion, the imaginary part leads to the appearance of spin-wave decay; it corresponds to the decay of magnons into electron-hole pairs [105]. The imaginary part of Equation (5.6) at $T = 0$ becomes

$$\begin{aligned} \mathrm{Im}\, J_{ij} = -\pi\omega\, \mathrm{Tr}_L \left(\mathrm{Re}\, p_i(\varepsilon_F)\, \mathrm{Im}\, T_{ij}^{\uparrow}(\varepsilon_F)\, \mathrm{Re}\, p_j(\varepsilon_F)\, \mathrm{Im}\, T_{ij}^{\downarrow}(\varepsilon_F) - \right. \\ \left. \mathrm{Im}\, p_i(\varepsilon_F)\, \mathrm{Re} T_{ij}^{\uparrow}(\varepsilon_F)\, \mathrm{Im}\, p_j(\varepsilon_F)\, \mathrm{Re} T_{ij}^{\downarrow}(\varepsilon_F) \right). \end{aligned} \tag{5.7}$$

Results

Let us present some of the SW lifetime results for the alloys on which we concentrated in the previous chapter.

Table 11 Spin-wave lifetime calculated for Fe and Ni as well as several alloys

Material	**SW lifetime,** $\times 10^{-15}$ sec
Ni	5
Fe	4.22
$(Ni_{99}Fe_{01})$	3.5
$(Ni_{80}Fe_{20})$	1.86
$(Ni_{80}Fe_{20})_{80}Cu_{20}$	0.28

We have some experimental results for the spin-flip scattering lifetime in Ni and Fe from [106]: $\tau_{Ni} = 3 \cdot 10^{-15}$ sec, $\tau_{Fe} = 1.5 \cdot 10^{-15}$ sec, and they seem to be reasonably close to the calculated ones. The lifetime is shorter for the alloys which makes us confident that the calculations are correct there.

Conclusions

We have implemented the calculation of the spin-wave lifetime for the case of CPA. We can see that the results of our calculations are reasonably close to the experimental ones. However, we have found experimental values for two materials only. For $(Ni_{80}Fe_{20})_{100-x}Cu_x$, the spin-wave lifetime seems to be of the order of the lifetime due to scattering calculated in **Chapter 3**.

Chapter 6. Final-state scattering (in ARPES) and FS of Fe

GW

The ground-state properties of various systems have been thoroughly investigated since the appearance of the DFT (for these, see the Introduction). Excited state properties, however, were studied rather poorly until the 1980s when the first practical implementation of Hedin's equations was accomplished [120,121,122].

The Hamiltonian for the system of electrons and nuclei has the following form of (1.1). The main difficulty here lies in the Coulomb interaction, which is pairwise, making it impossible to solve the Schrödinger equation until some simplifications are made. The most common way to do it is by replacing (1.1) with a single-particle Hamiltonian for an electron moving in effective external potential that accounts for the nuclei and the remaining electrons:

$$H = \sum_i h(\mathbf{x}_i) + \frac{1}{2}\sum_{i\neq j} v(\mathbf{x}_i, \mathbf{x}_j) + V_{nuc}, \qquad \mathbf{x} = (\mathbf{r}, \xi)$$
$$\text{where} \quad h(\mathbf{x}_i) = -\frac{\nabla_i^2}{2m_i} - \sum_I v(\mathbf{x}_i, \mathbf{R}_I), \quad v(\mathbf{x}_i, \mathbf{x}_j) = \frac{e^2}{|\mathbf{r}_i - \mathbf{r}_j|} \tag{6.1}$$

where $h(\mathbf{x}_i)$ includes the kinetic energy of an electron and its interaction with the nuclei, $v(\mathbf{x}_i, \mathbf{x}_j)$ represents the interaction between electrons, and $\mathbf{x}$ is the coordinate that includes spin.

To construct the effective potential, we use a complete set of one-particle orbitals $\psi_i(\mathbf{x})$ by making the Slater determinant $|\Psi\rangle = N^{-1/2}\det|\psi_i(\mathbf{x}_k)|$. We then use the variational principle to vary $\psi_i(\mathbf{x})$ until E is minimum. This procedure generates the following effective one-body Hamiltonian:

$$\begin{aligned} H &= h + V_H + V_x, \\ V_H(\mathbf{x}) &= \int v(\mathbf{x},\mathbf{x}')\rho(\mathbf{x}')d\mathbf{x}', \\ V_x(\mathbf{x},\mathbf{x}') &= -v(\mathbf{x},\mathbf{x}')\rho(\mathbf{x},\mathbf{x}'). \end{aligned} \tag{6.2}$$

Here the density and density matrix have the form $\rho(\mathbf{x}) = \sum_{i=1}^{N}\psi_i^*(\mathbf{x})\psi_i(\mathbf{x})$ and $\rho(\mathbf{x},\mathbf{x}') = \sum_{i=1}^{N}\psi_i^*(\mathbf{x})\psi_i(\mathbf{x}')$. We can also rewrite the Hamiltonian in terms of the creation and annihilation operators a_k^+ and a_k:

$$\begin{aligned} H &= \sum_{kl} h_{kl}a_k^+a_k + \frac{1}{2}\sum_{k_1k_2k_3k_4} v_{k_1k_2k_3k_4}a_{k_1}^+a_{k_2}^+a_{k_3}a_{k_4} + V_{nuc} \\ h_{kl} &= \int d\mathbf{x}\psi_k^*(\mathbf{x})\psi_l(\mathbf{x}) \\ v_{k_1k_2k_3k_4} &= \int d\mathbf{x}d\mathbf{x}'\psi_{k_1}^*(\mathbf{x})\psi_{k_2}^*(\mathbf{x}')v(\mathbf{x},\mathbf{x}')\psi_{k_3}(\mathbf{x})\psi_{k_4}(\mathbf{x}'). \end{aligned} \tag{6.3}$$

Let us define the field operators: $\psi(\mathbf{x}) = \sum_k a_k\psi_k(\mathbf{x})$, $\psi^+(\mathbf{x}) = \sum_k a_k^+\psi_k(\mathbf{x})$ and write the Hamiltonian in the following form:

$$H = \sum_{kl}\psi^+(\mathbf{x})h(\mathbf{x})\psi(\mathbf{x})d\mathbf{x} + \frac{1}{2}\int\psi^+(\mathbf{x})\psi^+(\mathbf{x}')v(\mathbf{x},\mathbf{x}')\psi(\mathbf{x})\psi(\mathbf{x}')d\mathbf{x}d\mathbf{x}' + V_{nuc}. \tag{6.4}$$

In the Heisenberg picture, the field operator's time-evolution has the form

$$\psi(\mathbf{x},t) = e^{iHt}\psi(\mathbf{x})e^{-iHt} \tag{6.5}$$

and therefore the Schrödinger equation becomes

$$i\frac{\partial}{\partial t}\psi(\mathbf{x},t)=\Big[h(x)+\int v(\mathbf{r},\mathbf{r}')\psi^{+}(\mathbf{x}',t)\psi(\mathbf{x}',t)d\mathbf{x}'\Big]\psi(\mathbf{x},t). \tag{6.6}$$

The matrix element coupling the ground $|N\rangle$ state and an eigenstates ν of $N-1$ electrons $|N-1,\nu\rangle$ is

$$\langle N-1,\nu|\psi(\mathbf{x},t)|N\rangle=\langle N-1,\nu|e^{iHt}\psi(\mathbf{x})e^{-iHt}|N\rangle=f_{\nu}(\mathbf{x})e^{-i\varepsilon_{\nu}t}, \tag{6.7}$$

where $\varepsilon_{\nu}=E(N)-E(N-1,\nu)$, and $f_{\nu}(\mathbf{x})=\langle N-1,\nu|\psi(\mathbf{x})|N\rangle$. From the Schrödinger equation (6.6), we have

$$\varepsilon_{\nu}f_{\nu}(\mathbf{x})=h(\mathbf{x})f_{\nu}(\mathbf{x})+\int v(\mathbf{r},\mathbf{r}')\langle N-1,\nu|\psi^{+}(\mathbf{x}')\psi(\mathbf{x}')\psi(\mathbf{x})|N\rangle d\mathbf{x}'. \tag{6.8}$$

By definition, one-particle Green's functions have the following form

$$G(\mathbf{x}t,\mathbf{x}'t')=-i\langle N|T\big[\psi(\mathbf{x},t)\psi^{+}(\mathbf{x}',t')\big]|N\rangle. \tag{6.9}$$

For $t>t'$, such a function describes the propagation of a particle created at the point $(\mathbf{x}',t')$ and annihilated at $(\mathbf{x},t)$. T is the time-ordering operator. In Heisenberg picture, it has the following form:

$$\begin{aligned}&G(\mathbf{x}t,\mathbf{x}'t')=-i\langle N|\psi(\mathbf{x})e^{-i(H-E_n)(t-t')}\psi^{+}(\mathbf{x}')|N\rangle\theta(t-t')+\\&i\langle N|\psi^{+}(\mathbf{x}')e^{+i(H-E_n)(t-t')}\psi(\mathbf{x})|N\rangle\theta(t-t')\quad\text{or}\end{aligned}$$

$$\begin{aligned}&G(\mathbf{x},\mathbf{x}',\tau)=\sum_{s}f_{s}(\mathbf{x})f_{s}^{*}(\mathbf{x}')\exp(-i\varepsilon_{s}\tau)\\&\times\big[\theta(\tau)\theta(\varepsilon_{s}-\mu)-\theta(-\tau)\theta(\mu-\varepsilon_{s})\big]\qquad\tau=t-t'.\end{aligned} \tag{6.10}$$

To work in the frequency domain, we take the Fourier transform of the Green's function which gives (see the definition of the GF (1.29))

$$G(\mathbf{x},\mathbf{x}',\tau)=\sum_{s}\frac{f_{s}(\mathbf{x})f_{s}^{*}(\mathbf{x}')}{\omega-\varepsilon_{s}+i\,\mathrm{sgn}(\varepsilon_{s}-\mu)\delta} \tag{6.11}$$

If we define the spectral weight as $A(\mathbf{x},\mathbf{x}',\omega)=\sum_s f_s(\mathbf{x})f_s^*(\mathbf{x}')\delta(\omega-\varepsilon_s)$, the relations between A and G are

$$\begin{aligned} A(\mathbf{x},\mathbf{x}',\omega) &= \frac{1}{\pi}\left|\mathrm{Im}\,G(\mathbf{x},\mathbf{x}',\omega)\right| \\ G(\mathbf{x},\mathbf{x}',\omega) &= \int_C \frac{A(\mathbf{x},\mathbf{x}',\omega')d\omega'}{\omega-\omega'}. \end{aligned} \tag{6.12}$$

We can also define a two-particle Green's function that describes the propagation of two particles (1) and (2) created at $(r_1',\xi_1',t_1')=(1')$ and $(r_2',\xi_2',t_2')=(2')$ and annihilated at (1) and (2):

$$G(1,2,1',2')=-i^2\left\langle N\left|T\left[\psi(1)\psi(2)\psi^+(2')\psi^+(1')\right]\right|N\right\rangle. \tag{6.13}$$

As for the 1-particle Green's function, we can write the equation of motion (EOM) for the 2-particle Green's function:

$$\begin{aligned} &\left[i\frac{\partial}{\partial t}-h(\mathbf{x})\right]G(\mathbf{x}t,\mathbf{x}'t')+i\int v(\mathbf{r},\mathbf{r}'')\left\langle N\left|T\left[\psi^+(\mathbf{x}'',t)\psi(\mathbf{x}'',t)\psi(\mathbf{x}',t')\psi^+(\mathbf{x}',t')\right]\right|N\right\rangle \\ &=\delta(\mathbf{x}-\mathbf{x}')\delta(t-t'). \end{aligned} \tag{6.14}$$

This equation contains a new Green's function, G_2. Writing the EOM for G_2 produces another one, etc. There are different methods to break that infinite chain of equations to be able to solve it. One of the methods was suggested by Schwinger. It requires adding an external potential, ϕ, that should then be set equal to zero at the end of the calculations. The derivative $\delta G/\delta\phi$ then generates G_2, etc. It was shown by Schwinger that

$$\frac{\delta G}{\delta\phi}=G(1,2)G(3,3^+)-G_2(1,2,3,3^+). \tag{6.15}$$

Using (6.15), EOM (6.14) can be transformed to the form

$$\left[i\frac{\partial}{\partial t} - h - \phi - V_H \right] G(1,2) + i\int v(1,3)G(1,4)\frac{\delta G^{-1}(4,5)}{\delta\phi(3)}G(5,2)d(345) = \delta(1,2) \tag{6.16}$$

If we define the self-energy as $\Sigma(1,2) = -i\int v(1,3)G(1,4)\frac{\delta G^{-1}(4,2)}{\delta\phi(3)}d(34)$, the EOM becomes

$$\left[i\frac{\partial}{\partial t} - h - \phi - V_H \right] G(1,2) - i\int \Sigma(1,5)G(5,2)d(5) = \delta(1,2), \tag{6.17}$$

which consists of two parts, a 'non-interacting' (first term on the left-hand side) part and an 'interacting' part (second term); hence, Σ contains information about the interactions. Using the chain rule, we can represent self-energy in a different way:

$$\begin{aligned} &\Sigma(1,2) = -i\int W(1,3)G(1,4)\Gamma(4,2,3)d(34), \\ &\Gamma(4,2,5) = \frac{\delta G^{-1}(4,2)}{\delta V(5)}, \quad \frac{\delta V(5)}{\delta\phi(3)} = \varepsilon^{-1}(5,3), \quad W(1,3) = -i\int v(1,2)\varepsilon^{-1}(2,3)d2. \end{aligned} \tag{6.18}$$

Now, it is possible to express the following five quantities in terms of each other

$$\begin{aligned} &P(1,2) = -i\int d(34)G(1,3)\Gamma(3,4;2)G(4,1^+) && \text{polarizability} \\ &W(1,2) = v(1,2) + \int d(34)v(1,3)P(3,4)W(4,2) && \text{Dyson eqn.} \\ &\Sigma(1,2) = i\int d(34)G(1,3^+)W(1,4)\Gamma(3,2;4) && \text{Self-energy} \\ &G(1,2) = G_0(1,2) + \int d(34)G_0(1,3)\Sigma(3,4)G(4,2) && \text{Dyson eqn.} \\ &\Gamma(1,2;3) = \delta(1,2)\delta(2,3) + \int d(4567)\frac{\delta\Sigma(1,2)}{\delta G(4,5)}G(4,6)G(7,5)\Gamma(6,7;3) \end{aligned} \tag{6.19}$$

G_0 is a Green's function corresponding to $\Sigma = 0$ (direct propagation from 1 to 2 without any exchange correlation interaction). In practical application [120], G_0

corresponds to $H_0 = H^{Hartree} + V^{xc}$. These equations can be solved iteratively as a power series in *W*. GW (G stands for the Green's function and W for the screened coulomb interaction) approximation replaces all these expressions by the following ones:

$$\begin{aligned} &\Sigma = iG_0W \\ &P = -iP_0P_0 \\ &W = \left(1 - Pv\right)^{-1} v = \varepsilon^{-1}v \\ &G = G_0 + G_0\Delta\Sigma G \quad \text{where} \quad \Delta\Sigma = \Sigma - V^{xc} \end{aligned} \tag{6.20}$$

It corresponds to replacing the bare Coulomb interaction υ by a screened interaction, *W*. After the Fourier transform, self-energy has the following form:

$$\Sigma\left(\mathbf{r},\mathbf{r}',\omega\right) = \frac{i}{2\pi}\int d\omega' G\left(\mathbf{r},\mathbf{r}',\omega+\omega'\right)W\left(\mathbf{r},\mathbf{r}',\omega'\right). \tag{6.21}$$

Quasi-particle self-consistent GW

One of the important problems in condensed matter physics is solving the Schrödinger equation (SE). It is used to describe the electronic states of an atom in independent-particle approximation, which is an approach to a many-particle system where each electron is assumed to move in effective potential that accounts for the nuclear field and the field of other electrons. One of the most common ways of solving SE is the local density approximation (see **Chapter 1**). Nevertheless, LDA has several limitations and often gives unsatisfactory results even for weakly correlated materials [122,124]. The GW approximation has been used for a long time, especially after it is shown that the use of LDA to generate self-energy improves the result of GW [125]. Still this approach is not always

satisfactory. Its result depends strongly on the quality of the LDA starting point and constructs *G* and *W* adequately for a limited number of cases only.

A new approach to GW has been introduced lately – the quasiparticle self-consistent GW (QSGW) method [126]. This method suggests optimization of the effective one-body Hamiltonian H_0 through the minimization of its perturbation. QSGW provides a way to determine the optimum one-body Hamiltonian $H_0 = -\frac{\nabla^2}{2m} + V^{\text{eff}}$: V^{eff} is chosen self-consistently in such a way that it minimizes the norm

$$M\left[V^{\text{eff}}\right] = \text{Tr}\left[\Delta V \delta\left(\omega - H^0\right)\left\{\Delta V\right\}^{\dagger}\right] + \text{Tr}\left[\left\{\Delta V\right\}^{\dagger}\delta\left(\omega - H^0\right)\Delta V\right], \qquad (6.22)$$

which actually amounts to minimization of the difference between the time evolution determined by H_0 and the one determined by $H(\omega)$ [124]. *Tr* is for space, spin, and ω. This minimization occurs when

$$V^{xc} = \frac{1}{2}\sum_{ij}\left|\Psi_i\right\rangle\left\{\text{Re}\left[\sum\left(\varepsilon_i\right)\right]_{ij} + \text{Re}\left[\sum\left(\varepsilon_j\right)\right]_{ij}\right\}\left\langle\Psi_j\right|, \qquad (6.23)$$

where $\left\{\varepsilon_i, \Psi_i(\mathbf{r})\right\}$ correspond to H^0 [122]. It gives a direct way of calculating new V^{eff}: $V^{\text{eff}} \to V^{\text{GW}}(\omega) \to V^{\text{eff}}$, since for a given V^{eff} it becomes possible to calculate V^{xc} via $\Sigma(\omega)$ in GWA. Together with V^H (calculated for G^0), it gives a new potential, V^{eff}.

Solutions to H^0 are defined as 'bare QP' interacting via the bare υ [124]. The 'dressed QP' consists of the central bare QP and the induced polarized clouds by other bare QPs.

Let us now compare the results obtained by using QSGW to the ones calculated in LDA and the experimental data for ferromagnetic iron.

ARPES and de Haas-van Alphen data for Fe

There is a large number of experimental work on the electronic band structure and the Fermi surface (FS) in ferromagnetic iron, such as de Haas-van Alphen (dHvA) [127,128], magnetoresistance [129,130,131] measurements, and rather recent high-resolution angle-resolved photoemission (ARPES) [34] experiments. These results are a good reference to test different methods of electron structure calculations. We compared the Fermi surface of Fe and the cyclotron data available to QSGW and LDA calculations to estimate their validity; we also compared those approximations. Iron has been chosen because high-resolution spectroscopy data is limited for transition metals, but ARPES results are available for it because of the relative simplicity of growing iron films [132].

LDA and dynamical mean-field theory (DMFT) calculations in Fe have been carried by J. Callaway and C.S. Wang [133] and J. Sánchez-Barrida [134] respectively. However, neither describes ARPES data well.

Fermi surface

We calculated the Fermi surface of iron in QSGW and LDA to compare them to each other and also put it against the experimental data. **Fig. 26** compares

the results obtained by LDA (grey line for the majority-spin pieces, light green for the minority-spin pieces), QSGW (black and dark green lines for majority and minority spins respectively), and the experimental data from dHvA and magnetoresistance experiments [127-131] (red lines). The dHvA and magnetoresistance results can be adequately interpreted using two models – one suggested by Gold et al. [128], **Fig. 26** (a), and another drawn by Lonzarich [131], **Fig. 26** (b). Experiments do not provide a conclusive choice regarding the model, which is why we will compare our numerical results with both of them.

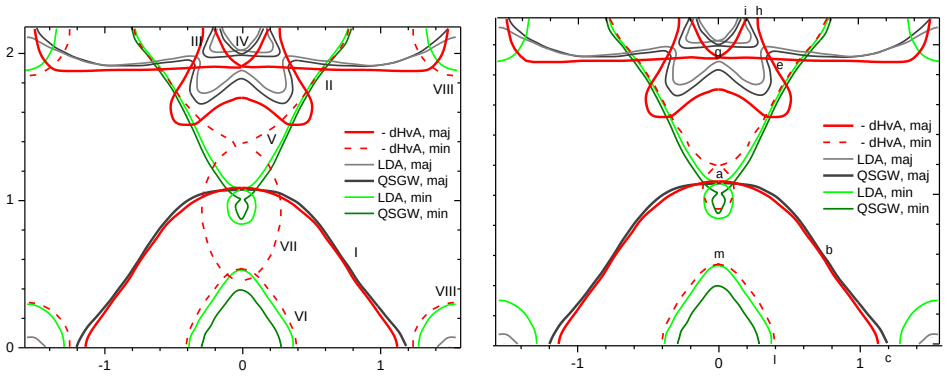

Fig. 26 dHvA/magnetoresistance data (two possible experimental data interpretations as suggested by Gold a/b) [128,129,131] for the Fermi surface of Fe with LDA and QSGW calculations.

In Fig. 27, the numerical calculation of the Fermi surface is compared with the experimental ARPES data [132]. The top left figure shows the experimental result from [132] for the Fermi surface of iron at the Brillouin zone (BZ) central plane ($h\nu = 139$ eV), with the DFT calculations being performed by the authors; the top right figure shows the numerical result by LDA and QSGW; the bottom figure has both experimental data (ARPES – background; dHvA – red lines) and

numerical calculations (the colours are given in the same way as in **Fig. 26**). We also use the labelling of FS sheets first used by Callaway and Wang [133].

Let's compare all the pieces of FS:

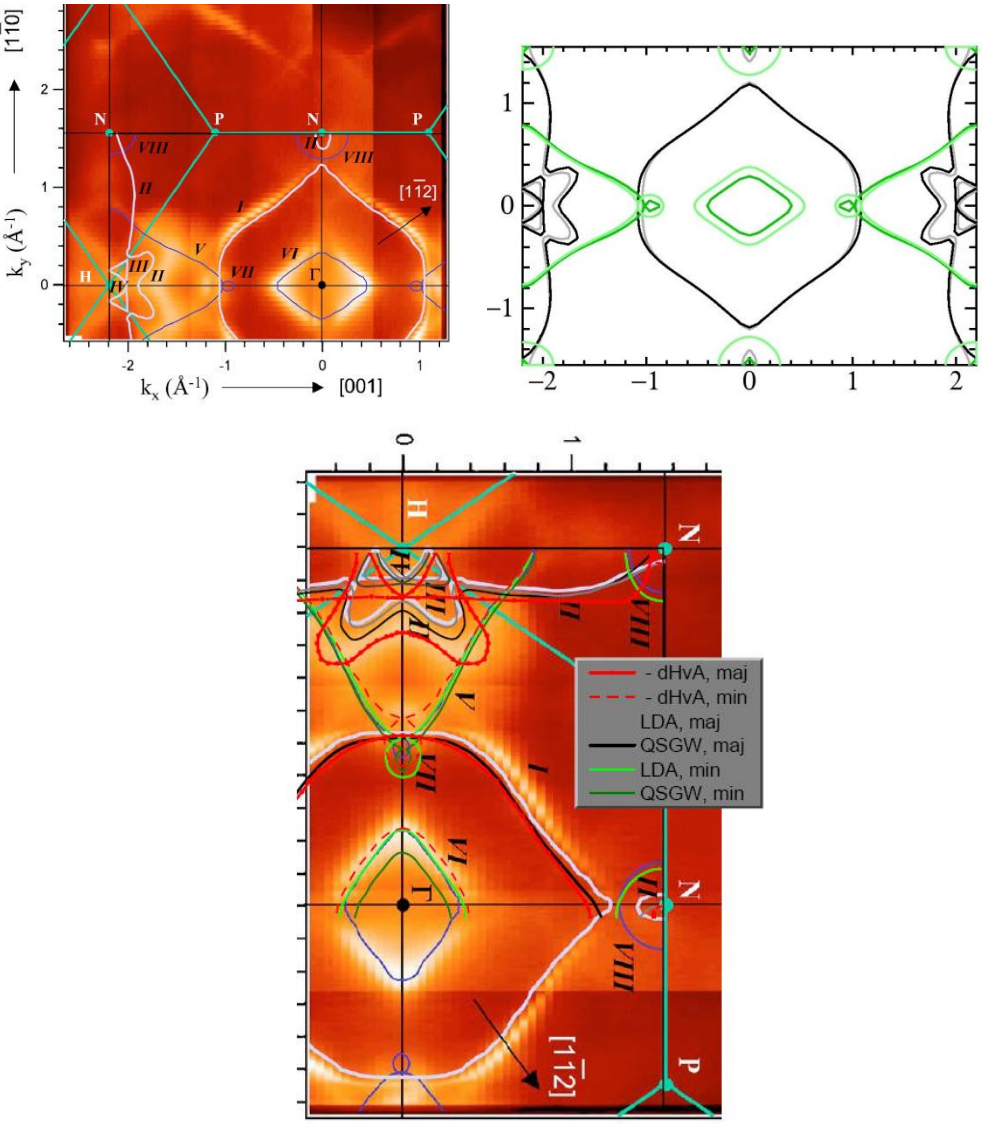

Fig. 27 Top, left: ARPES data [132]; top, right: calculated the Fermi surface, for the colours, see the text above; bottom: experimental data compared to numerical results

I. The large spin-up electron surface centred at Γ. Both QSGW and LDA calculations are in good agreement with both ARPES and de dHvA data for this piece (see **Fig. 26** and Fig. 27).

II. The large spin-up hole surface around H. The topology of the piece near the point N is still subject to uncertainty [129]. Both QSGW and LDA results for this surface are uniformly smaller than the experimental data (even though QSGW is a little larger and hence closer to experiment). Agreement in the shape between theory and experiment is fairly good.

III and IV. The intermediate and small spin-up hole pockets at H. Here the calculated cross-sections are again smaller than the ones attributed to them by dHvA measurements. QSGW gives a curve slightly closer to experimental data.

V. The large spin-down hole surface around H, VII The electron ball along Δ. There is strong disagreement between the two models describing dHvA and magnetoresistance experimental data [128] for these two cross-sections (see **Fig. 26**) (a,b). Both our calculations predict a small ball (VI) (QSGW gives a smaller shape here) touching the hole octahedron (V), which is in fairly good agreement with the second model suggested by Lonzarich [131] (see **Fig. 26**) (b). It also seems to be close to ARPES data.

VI. The spin-down central electron surface about Γ. In terms of the shape, QSGW results for the cross-section of this surface are in good agreement with both dHvA/magnetoresistance and ARPES data however are a little smaller.

VIII. The spin-down hole pockets around N. The topology near the point N is still subject to uncertainty in the interpretation of dHvA and magnetoresistance

data [129]. The second model by Lonzarich, which seems to describe the surfaces V and VII better, also predicts the smaller pockets around N that is in good agreement with QSGW calculations, while LDA gives the much larger ones (see **Fig. 26**) (b).

You can see the numbers for the FS dimensions in Table 12 (k-vectors found in the dHvA experiment and obtained by QSGW and LDA calculations) for an easier comparison.

Table 12. Principal Fermi-surface dimensions in units of $2\pi / a$: in the columns from left to right: experimental data by Baraff [127], QSGW, and LDA calculations (for majority and minority spin). The point notations are shown in Fig. 26 (b)

Identification	dHvA D.R. Baraff [127]	QSGW (maj)	LDA (maj)	QSGW (min)	LDA (min)
Γ-a	0.514	0.507	0.473		
Γ-b	0.432	0.439	0.470		
Γ-c	0.495	0.533	0.549		
Γ-1	0.189			0.122	0.243
Γ-m	0.242			0.176	0.243
H-e	0.187	0.134	0.108		
H-g	0.110	0.071	0.055		
H-h	0.126	0.800	0.798		
H-i	0.089	0.068	0.057		

Final-state scattering

Hence, we can see that even though QSGW FS is in good agreement with ARPES data, there are certain discrepancies, especially along the Γ-H line. We will try to explain these discrepancies by accounting for the final state scattering in the experimental data.

In QSGW, energy bands $E(\boldsymbol{k})$ are associated with the peaks in the spectral function $A(\boldsymbol{k},\omega)$ [135]. In the Fermi liquid (FL) regime, ARPES spectra $I((\boldsymbol{k},\omega)$ are

usually directly compared to the spectral function. However, even in the FL regime, ARPES data does not actually give $A(\mathbf{k},\omega)$ due to the presence of final-state scattering. Let us assume a one-step model [136] of the photoemission process when the initial and final states are coupled through Fermi's golden rule [136,137], and therefore, the ARPES spectra is written as:

$$I(\mathbf{k},\omega) \propto \int dk_{\perp} \left|T_{fs}\right|^2 \left|M_{fi}(\mathbf{k}_{\perp})\right|^2 A_f(\mathbf{k}_{\perp}) A(\mathbf{k},\omega). \tag{6.24}$$

The final-state spectral function here is broadened by the scattering of photoelectrons approaching the surface [138]:

$$A(k_{\perp}) = \frac{\Delta k_{\perp} / 2\pi}{(\Delta k_{\perp} / 2)^2 + \left(k_{\perp} - k_{\perp}^0\right)^2}. \tag{6.25}$$

T_{fs} stands for the final-state surface transmission amplitude; M_{fi} is the photoexcitation matrix element ($\left|T_{fs}\right|^2$ and $\left|M_{fi}(\mathbf{k}_{\perp})\right|^2$ are assumed to be constant and k-independent [139]); $k_{\perp}$ is a surface-perpendicular momentum component that is no longer a conserved quantity due to the existence of a surface [138]. So, the $A(k_{\perp})$ is characterized by the Lorentzian distribution $k_{\perp}$ in at $k_{\perp}^0$ of the final-state Bloch wave with the width $\Delta k_{\perp}$ [138]. The initial state in our case in an undamped Bloch function with the energy-broadening ΔE calculated by using the QSGW spectral function. $\Delta k_{\perp}$ can be obtained from the inverse of the electron MFP. For the photon energy within the range 100-130 eV $\Delta k_{\perp} \approx 0.2$ Å^{-1} [140,141].

Apart from broadening $I(\omega)$ final-state scattering shifts the peaks in it as well. The most significant discrepancy between ARPES data and our calculation is the FS piece V (see Fig. 27). Let's try to estimate the shift this effect should give it.

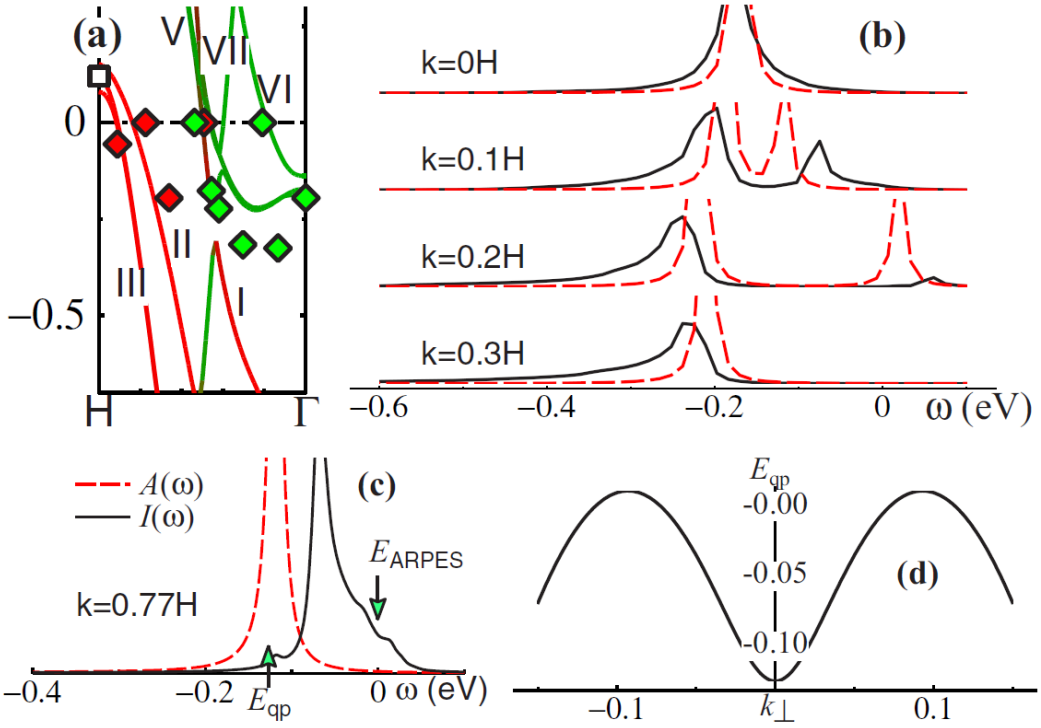

Fig. 28 Comparison between QSGW and ARPES band structures. **(a)** The Γ-H line of the QSGW band structure (solid lines) and the ARPES spectra (diamonds); **(b)** The QSGW spectral function $A(k,\omega)$ (dashed line) for various points on the $\Gamma(k = 0)$ - $H(k = 1)$ line. The solid line is $A(\omega)$ modified according to Eq. (6.24) **(c)** The analogue of (b) at $k = 0.77 \times H$, where the II-band crosses E_F. E_{QP} indicates the QSGW quasiparticle level and E_{ARPES} the experimental ARPES peak at 0.77H. **(d)** Dispersion in the QSGW II band on the line $k_\perp + [0,0,0.77H]$ is normal to the film surface [135].

Fig. 28 (b) shows both QSGW spectral functions $A(\boldsymbol{k},\omega)$ and $I(\boldsymbol{k},\omega)$ being calculated by using the formula (6.24). We can estimate the peak shift from $\delta\bar{\omega} = \int d\omega\omega I / \int d\omega I - \int d\omega\omega A / \int d\omega A$. At Γ, it is $\delta\bar{\omega} < 0.01\,\text{eV}$ and increases to about 0.06 eV for k between 0.1H and 0.3H, which is indeed very close to the

discrepancy between the V_m band and the ARPES data for $0.1H < k < 0.3H$. We can perform the same analysis for the II_m band near $k = 0.77 \times H$; at crossing $E_{F,}$ QSGW is deviated from the ARPES peak by almost 0.15 eV. However, if we use Equation (6.24) the calculated result is much closer to the experimental data, see Fig. 28 (c). Hence, we attribute most of the discrepancy in the Fermi surface crossing for band II_m to the effect of final-state scattering.

Table 13. de Haas-van Alphen measurements of extremal areas on the [110] and [111] FS, in $Å^{-2}$. ΔE_F is an estimate of the error in the QP level (eV); (bottom of the table): cyclotron masses.

FS piece	dHvA [110]			dHvA [111]		
	QSGW	exp. [127]	ΔE_F	QSGW	exp. [127]	ΔE_F
I	3.355	3.3336	0.01	3.63	3.5342	0.04
II				3.694		
III	0.2138	0.3190	0.05	0.1627	0.2579	0.06
IV	0.0897	0.1175	0.04	0.0846	0.1089	0.02
VI	0.3176	0.5559	−0.13	0.2799	0.4986	−0.14
VII	0.0148	0.0405	0.04			
	m^*/m [110]			m^*/m [111]		
	QSGW	LDA	exp. [142]	QSGW	LDA	exp. [142]
I	2.5	2.0	2.6			
V				−1.7	−1.2	−1.7
VI				2.0	1.5	2.8

We can also compare our QSGW results to de Haas-van Alphen (dHvA) and magnetoresistance measurements that provide the extremal areas of FS cross-sections to a high precision. Areas normal to [110] and [111] are given in Table 13 along with areas calculated by QSGW. As mentioned before, QSGW FS resembles closely the one suggested by Lonzarich (Version 2) [131], apart from the small VIII pocket at N, as its tiny area is sensitive to computational details. Instead of discrepancies in the extremal areas, it is more sensible to operate with the change ΔE_F at the Fermi level to make the QSGW area agree with dHvA measurements. This amounts to the average error in the QSGW QP levels if we assume that the bands shift rigidly. This assumption is well verified for all pieces of FS, except for the small VI piece owing to strong electron-phonon coupling.

We have also compared our results to the cyclotron data for effective masses also available [142], which are expected to be more reliable than ARPES data. To find the cyclotron mass, we used the formula

$$\frac{m^*}{m} = \left(\frac{\hbar^2}{2\pi m} \right) \frac{\partial A}{\partial E} \tag{6.26}$$

for which we had to find the derivative by varying E a little and noting the change in area. We can see very good agreement with the experimental data (bottom of Table 13), except for the small VI pocket.

Conclusion

We can summarize this chapter with the following points:

We compared the results of dHvA, magnetoresistance, and ARPES experiments for Fe with the data obtained numerically by using the QSGW approximation.

Even though overall the numerical results are in good agreement with experimental data, some of the QSGW calculations for small Fermi surface pieces seem to be uniformly smaller than the dHvA experimental data. To account for that discrepancy, we suggested considering the final-state effects, such as the scattering of electrons as they move to the surface from the excitation point, and corrected our results according to it. After the correction, we found that QSGW QP levels at E_F have an error of ~0.05 eV, and effective masses are well described. The QSGW *d* bandwidth falls in close agreement with ARPES and is approximately 0.75 times that of the LDA. So, in the case of ferromagnetic iron QSGW is capable of closely reproducing the Fermi surface.

Conclusions

The main goal of this study was to enable the electronic structure code Questaal [53] to account for relativistic effects by replacing the Schrödinger equation used at some point of the calculations by the Dirac equation. Different solutions of this problem have been proposed by many authors: a single site problem was first solved by S. Doniach and C. Sommers, who derived the corresponding coupled radial Dirac equation [45]. This problem was then considered in more detail by Feder et al. [46] and by Strange et al. [47]. The relativistic development was then introduced to other band-structure schemes such as KKR [46,48], LMTO [21], and ASW [49]. Additional details can be found in the works of Solovyev et al. [50,51,52]. We modified the scalar-relativistic version of the code to the fully relativistic (FR) LMTO scheme (using the Dirac equation) by using the procedure similar to that of Ebert [21].

For the core states, we implemented the method proposed by Ebert [21] which involves solving of the Dirac equation both inwards and outwards and matching the reliable parts by minimizing the function of the gaps between two solutions. We also constructed a similar way for solving the equation for the valence states with the difference in the way initial conditions are chosen for the integration inwards and a function of the gaps constructed differently.

Calculations performed for various materials show us that relativistic corrections can be important even for light elements (3d metals) and alloys.

The changes made for the relativistic case affect many quantities and methods of calculating them. We especially considered the Green's functions and the quantities made of them, such as susceptibility, magnetic exchange interactions, and the spin-wave lifetime. The method of calculating those was described with specific attention paid to the CPA case. Here we also demonstrated the importance of the relativistic effects by demonstrating how much the values for heavier elements differ if considered relativistically.

We outlined the changes required for the CPA to be treated in the relativistic case. We also used the said approximation to look into $(Ni_{1-x}Fe_x)_{1-y}Z_y$, *Z=Cu, Cr, Mn,* and *Rh* alloys. Here we intended to determine the one with the lowest possible magnetization and Curie temperature, as well as the minimum alloy scattering, which is required for the experimental applications outlined in the text. We established the Cr-permalloy alloys to be the best choice for it and suggested minimization of the scattering by replacing some of the Fe in the alloys with Co.

As a separate matter, we considered the data of ARPES and magnetoresistance experiments for iron by comparing it with the FS and cyclotron masses calculated by using QSGW. A way to account for the final scattering effects in ARPES was suggested as well – with this, the calculations seem to be in good agreement with the experiment.

We would like to outline several cases where using the fully relativistic calculations might be important.

Possible future implementations of the method

Magnetic anisotropy. Relativistic calculations are extremely important when looking at magnetic anisotropy (MA). Even though it possesses a small energy scale, magnetic anisotropy is responsible for a large number of important phenomena that can have a vast number of applications. A large group of systems with this property also has a uniaxial magnetic symmetry (magnetization is directed along a particular axis). These systems are quite important due to the recent search for permanent magnetic materials without rare earth elements [143-145].

For such systems to be practical, they should have a uniaxial magnetic symmetry in the temperature region at least between 0 and 200 ºC. It can be extremely useful to stabilize magnetization around and above room temperature – it can be achieved by doping and changing other relevant parameters.

One of the main difficulties here lies in the fact that there is no general analytical theory explaining magnetic anisotropy. It is known that the source of it lies in the crystal field effects and relativistic interactions (usually spin orbital coupling), but it can be also strongly affected by band filling, magnetization, and temperature effects. The decay of the absolute value of anisotropy with temperature has been predicted in several localized spin models, which, however, do not explain the other observed phenomena like improvements of anisotropy or

coercivity at finite temperatures. The situation is even worse with a description of the anisotropy as a function of the electron or hole doping.

While no analytical theories describe magnetic anisotropy, it is possible to address the matter with electronic structure methods that are capable of calculating such quantities as magnetization, Curie temperature, etc. Studying magnetic anisotropy in disordered substitutional magnetic alloys might be a convenient way to address the dependence of anisotropy on doping, while all other relevant parameters (such as spin orbit coupling, hybridization, structure) are relatively fixed and do not affect the anisotropy.

There are several methods of calculating magnetic anisotropy, such as magnetic force theorem [146] and the DFT calculation of the energy difference for different magnetization axes [147].

Spin-flip scattering at metallic interfaces. The discovery of giant magnetoresistance (GMR) [148] attracted much attention to spin-dependent transport across interfaces. GMR is the change of the resistance of a ferromagnetic/normal metal multilayer, as its spin configuration is changed from parallel to anti-parallel by the external magnetic field.

The effect depends on interface scattering and spin-diffusion lengths of the materials [149]. Spin-flip scattering is usually assumed to be small and is neglected. However, the measurements carried out by the Michigan State University group [149,151] suggested surprisingly large probabilities of spin-flip transmissions at interfaces, both between two normal metals (such as Pt/Cu) and between a ferromagnet and a normal metal (such as Co/Ag).

Within the fully-relativistic LMTO method and CPA, it might be possible to study the spin-flip transmission probabilities for metallic interfaces such as Ag/Cu, Pd/Au, Pt/Cu, Co/Ag, etc. Here the same relativistic corrections should be applied to the layer Green's functions technique.

Hence, we hope that the adjustments made to the code will be useful for further research.

Bibliography

1. R.G. Parr, D.P. Craig, I.G. Ross, *J. Chem. Phys.* **18**, 1561 (1950)
2. T.C. Chen, *J. Chem. Phys.* **23**, 2200 (1955)
3. D.R. Hartree, *Proc. Cambridge Phil. Soc.* **24**, 98 (1928)
4. V. Fock, *Z. Phys.* **61**, 126 (1930)
5. E.P. Wigner and F. Seitz, *Phys. Rev.* **43**, 804 (1933)
6. E.P. Wigner and F. Seitz, *Phys. Rev.* **46**, 509 (1934)
7. R.M. Martin, '*Electronic Structure: Basic Theory and Practical Methods'*, Cambridge University Press, Cambridge (2008)
8. W.M.C. Foulkes, L. Mitas, R.J. Needs, G. Rajagopal, *Rev. Mod. Phys.* **73**, 33 (2001)
9. W.G. Aulbur, L. Jönsson, J.W. Wilkins, *Solid State Phys.* **54**, 1 (2000)
10. A. Georges, G. Kotliar, W. Krauth, M.J. Rozenberg *Rev. Mod. Phys.* **68**, 13 (1996)
11. M. Born and J.R. Oppenheimer, *Ann. Physic* **84**, 457 (1927)
12. D.I. Blokhincev, '*Basics of quantum mechanics'*, Science, Moscow (1976)
13. R. O. Jones and O. Gunnarsson, *Rev. Mod. Phys.* **61**(3), 689 (1989).
14. R.G. Parr and W. Yang, '*Density-Functional Theory of Atoms and Molecules*', OUP, Oxford (1989)
15. J. Callaway and N.H. March, *Solid State Phys*. **38**, 135 (1984)

16. P. Hohenberg and W. Kohn, *Phys. Rev.* **136**, B864 (1964)
17. N.D. Mermin, *Phys. Rev.* **137**, A1441 (1965)
18. W. Kohn and L. J. Sham, *Phys. Rev.* **140**, A1133 (1965)
19. N.M. Temme, '*Special Functions: An introduction to the classical functions of mathematical physics*', 2nd ed., Wiley, New York (1996)
20. O.K. Andersen, '*Computational Methods in Band Theory'*, Plenum, New York (1971)
21. H. Ebert, *Phys. Rev. B* **38**, 9390 (1988)
22. O.K. Andersen, *Phys. Rev. B* **12**, 3060 (1975)
23. E.U. Condon and G.H. Shortley, '*Theory of Atomic Spectra*', Cambridge University Press, New York (1935)
24. J.A. Gaunt, *Phil. Trans. Roy. Soc. (London)* **228**, 151 (1929)
25. H.L. Skriver, '*The LMTO method: muffin-tin orbitals and electronic structure*', Springer, Berlin (1984)
26. J. Kübler and V. Eyert, '*Electronic and Magnetic Properties of Metals and Ceramics'*, VCH-Verlag, Weinheim (1992)
27. O.K. Andersen, A.V. Postnikov, and S.Yu. Savrasov, *MRS Proceedings*, **253**, 37 (1991)
28. M. César, *thesis*, McGill University Montréal, Québec, Canada (2017)
29. J. Korringa, *Physica* **13**, 392 (1947)
30. W. Kohn and N. Rostocker, *Phys.Rev*. **94**, 1111 (1954)
31. A. Gonis, '*Green Functions for Ordered and Disordered Systems*', North Holland/Elsevier, Amsterdam (1992)

32. A. Gonis and W.H. Butler, '*Multiple Scattering in Solids*', Springer, New York (2000)
33. I. Mertig, E. Mrosan. and P. Ziesche, '*Multiple Scattering Theory for Point Defects in Metals: Electronic Properties'*, Teubner-Verlag, Leipzig (1987)
34. N. Papanikolaou, R. Zeller, and P.H. Dederichs *J.Phys.: Condens. Matter*, **14**, 2799 (2002)
35. R. Zeller, P. H. Dederichs, B. Újfalussy, L. Szunyogh, and P. Weinberger *Phys. Rev. B* **52**, 8807 (1995)
36. E.N. Economou, '*Green's functions in quantum physics'*, 2nd ed., Springer-Verlag, Berlin (1992)
37. A. Klein, '*Theory of Normal Fermion Systems'*, in: Lectures on the Many-body Problem, vol. 1, Academic Press, New Your (1962)
38. B. Újfalussy, L. Szunyogh, P. Bruno, and P. Weinberger, *Phys. Rev. Lett*. **77**, 1805 (1996)
39. J. Banhart and H. Ebert, *Europhys. Lett*. **32**, 517 (1995)
40. '*Magnetic interactions and spin transport*', edited by A. Chtchelkanova, S. Wolf, and Y. Idzerda, Springer-Science and Business Media, New York (2003)
41. J. Callaway and C.S. Wang, *Phys. Rev. B* **7**, 1096 (1973)
42. F. Rosicky, P. Weinberger, and F. Mark, *J. Phys. B* **9**, 2971 (1976)
43. H. Gollisch and L. Fritsche, *Phys. Status Solidi B* **86**, 145 (1978)

44. E. van Lenthe, E.J. Baerends, and J.G. Snijders, *J. Chem. Phys.* **101**, 9783 (1994)
45. S. Doniach and C. Sommers, *'Valence Fluctuations in Solids*', North-Holland, Amsterdam (1981)
46. R. Feder, F. Rosicky, and B. Ackermann, *Z. Phys. B* **52**, 31 (1983)
47. P. Strange, J. B. Staunton, and B. L. Gyorffy, *J. Phys. C* **17**, 3355 (1984)
48. P. Strange, H. Ebert, J. B. Staunton, and B. L. Gyorffy, *J. Phys. Condens. Matter* **1**, 2959 (1989)
49. B.C.H. Krutzen and F. Spingelkamp, *J. Phys. Condens. Matter* **1**, 8369 (1989)
50. V. Solovyev, A.B. Shick, V.P. Antropov, A.I. Liechtenstein, V.A. Gubanov, and O. K. Andersen *Fizika Tverd. Tela* **31 (**8), 13 (1989); [*English translation: Sov. Phys. - Solid State **31**, 1285 (1989)*]
51. A.B. Shick, I.V. Solovyev, V.P. Antropov, A.I. Liechtenstein, and V.A. Gubanov, *Fizika Met. Metalloved.* **1**, 61 (1992)
52. V. Solovyev, A.I. Liechtenstein, V.A. Gubanov, V.P. Antropov, and O.K. Andersen, *Phys. Rev. B* **43**, 14414 (1991)
53. https://www.questaal.org/about/questaal/. See also Dimitar Pashov, Swagata Acharya, Walter R. L. Lambrecht, Jerome Jackson, Kirill D. Belashchenko, Athanasios Chantis, Francois Jamet, Mark van Schilfgaarde, https://arxiv.org/abs/1907.06021
54. P. Weinberger, '*Electron Scattering Theory for Ordered and Disordered Matter*', Clarendon Press, Oxford (1990)

55. H. Ebert, *J. Phys.: Condens. Matter* **1**, 9111 (1989)

56. S. H. Vosko, L. Wilk, and M. Nusair, *Can. J. Phys*. **58**, 1200 (1980)

57. J. P. Perdew and A. Zunger, *Phys. Rev. B* **23**, 5048 (1981)

58. R.O. Jones and O. Gunnarsson, *Rev. Mod. Phys.* **61**(3), 689 (1989)

59. W. Koch, M.C. Holthausen, '*A Chemist's Guide to Density Functional Theory*', 2nd ed., Wiley VCH Verlag GmbH, Weinheim (2001)

60. J.P. Perdew, J.A. Chevary, S.H. Vosko, K.A. Jackson, M.R. Pederson, D.J. Singh, and C. Fiolhais, *Phys. Rev. B* **46**(11), 6671, (1992)

61. M.E. Rose, '*Relativistic Electron Theory'*, Wiley, New York (1961)

62. A.B. Shick, V. Drchal, J. Kudrnovský, and P. Weinberger, *Phys. Rev. B* **54**, 1610 (1996)

63. J.C. Butcher, '*Numerical Methods for Ordinary Differential Equation'*, John Wiley&Sons, New York (2008)

64. W.R. Johnson, '*Atomic Structure Theory. Lectures on Atomic Physics*', Springer-Verlag, Berlin (2007)

65. C. Godreche, *J. Magn. Magn. Mater*. **29**, 262 (1982)

66. N.E. Christensen, *Int. J. Quantum Chem*. **25**, 233 (1984)

67. J.M. Franse, R. Gersdorf, H.P.J. Wijn, '*Magnetic Properties of Metals 3d, 4d and 5d Elements, Alloys and Compounds'*, Landolt–Bornstein New Series, Group III, vol. 19 (2001) [*Springer-Verlag, Berlin (1986)*]

68. D.M. Ceperley and B.J. Alder, *Phys. Rev. Lett*. **45**, 566 (1980)

69. J.C. Slater, *Phys. Rev.* **51**, 846 (1937)

70. I. di Marco, *thesis*, Radboud Universiteit, Nijmegen, Netherlands (2009)

71. R. Shankar, '*Principles of Quantum Mechanics*', Plenum Publishing, New York (1980)
72. J.D. Jackson '*Classical Electrodynamics*', Wiley, New York (1962)
73. A. Messiah, '*Quantum Mechanics'*, vol. I, Wiley, New York (1964)
74. O. K. Andersen, Z. Pawlowska, and O. Jepsen, *Phys. Rev. B* **34**, 5253 (1986)
75. I. Turek, V. Drchal, J. Kudrnovsky, M. Sob, and P. Weinberger, '*Electronic structure of disordered alloys, surfaces and interfaces'*, Springer Science+Business Media, New York (1997)
76. P. Soven, *Phys. Rev.* **156**, 809 (1967)
77. B. Velicky, S. Kirkpatrick, and H. Ehrenreich, *Phys. Rev.* **175**, 747 (1968)
78. M. Lax, *Rev. Mod. Phys.* **23**, 287 (1951)
79. J. L. Beeby *Phys. Rev.* **135**, A130 (1964)
80. G.M. Stocks, W.M. Temmerman, and B.L. Gyorffy, *Phys. Rev. Lett.* **41**, 339 (1978)
81. J. Kudrnovsky, V. Drchal, and J. Mašek, *Phys. Rev. B* **35**, 2487 (1987)
82. R.J. Elliott, J.A. Krumhansl, and P.L. Leath, *Rev. Mod. Phys*. **46**, 465 (1974)
83. J.S. Faulkner, *Prog. Mater. Sci.* **27**, 1 (1982)
84. A. Gonis, '*Green Functions for Ordered and Disordered Systems*', NorthHolland, Amsterdam, (1992)
85. M. Ondráček, O. Bengone, J. Kudrnovský, V. Drchal, F. Máca, and I. Turek, *Phys. Rev. B* **81**, 064410 (2010)

86. P. Bruno, J. Kudrnovský, V. Drchal, and I. Turek, *Phys. Rev. Lett.* **76**, 4254 (1996)

87. M.A. Qader, A. Vishina, L. Yu, C. Garcia, R.K. Singh, N.D. Rizzo, M. Huang, R. Chamberlin, K.D. Belashchenko, M. van Schilfgaarde, and N. Newman, *JMMM* **442**, 45 (2017)

88. D.C. Ralph, M.D. Stiles, *JMMM* **320**, 1190 (2008)

89. M.A. Qader, R.K. Singh, S. Galvin, L. Yu, J.M. Rowell, and N. Newman, *Appl. Phys. Lett.* **104**, 022602 (2014)

90. B. Baek, W.H. Rippard, S.P. Benz, S.E. Russek, and P.D. Dresselhaus, *Nat. Commun.* **5**, 3888:1-6 (2014)

91. T.I. Larkin, V.V. Bol'ginov, V.S. Stolyarov, V.V. Ryazanov, I.V. Vernik, S.K. Tolpygo, and O.A. Mukhanov, *Appl. Phys. Lett*. **100**, 222601 (2012)

92. O. K. Andersen and O. Jepsen, *Phys. Rev. Lett.* **53**, 2571 (1984)

93. N.D. Rizzo, M. DeHerrera, J. Janesky, B. Engel, J. Slaughter, and S. Tehrani, *Appl. Phys. Lett.* **80**, 2335 (2002)

94. O.K. Andersen, Z. Pawlowska, and O. Jepsen, *Phys. Rev. B* **34**, 5253 (1986)

95. H.E.H. Stremme, *Phys. Lett. A* **46**, 126 (1973)

96. P.E. Mijnarends, S. Sahrakorpi, M. Lindroos, and A. Bansil, *Phys. Rev. B* **65**, 075106 (2002)

97. D.Y. Petrovykh, K.N. Altmann, H. Höchst, M. Laubscher, S. Maat, G.J. Mankey, and F. J. Himpsel, *Appl. Phys. Lett.* **73**, 3459 (1998)

98. A.I. Liechtenstein, M.I. Katsnelson, V.P. Antropov, and V.A. Gubanov, *JMMM* **67**, 65 (1987)

99. R.C. O'Handley, '*Modern Magnetic Materials: Principles and Applications*', Wiley, New York (2000)

100. V.A. Gubanov, A.I. Liechtenstein, A.V. Postnikov, '*Magnetism and the Electronic Structure of Crystals*', Springer-Verlag, Berlin (1992)

101. S. Mathias *et al*., *Proc. Natl. Acad. Sci. USA* **109**, 4792 (2012)

102. A. Aguayo, I.I. Mazin, and D.J. Singh, *Phys. Rev. Lett.* **92**, 147201 (2004)

103. A. Devonport, A. Vishina, R.K. Singh, M. Edwards, K. Zheng, J. Domenico, N.D. Rizzo, C. Kopas, M. van Schilfgaarde, and N. Newman, *JMMM* **460**, 193 (2018)

104. N.W. Ashcroft and N.D. Mermin, '*Solid State Physics',* Harcourt, Orlando (1976)

105. V.P. Antropov, M.I. Katsnelson, and A.I. Liechtenstein, *Physica B* **237–238**, 336 (1997)

106. V. Kambersky, *Can. J. Phys.* **48**, 2906 (1970)

107. T. Oguchi, K. Terakura, and N. Hamada, *J. Phys. F: Met. Phys.* **13**, 145 (1983)

108. T. Moriya, H. Hasegawa, *J. Phys. Soc. Jpn*. **48**, 1490 (1980)

109. C.S. Wang, R.E. Prange, and V. Korenman, *Phys. Rev. B* **25**, 5766 (1982)

110. A.I. Liechtenstein, M.I. Katsnelson, and V.A. Gubanov, *J. Phys. F: Met. Phys.* **14**, L152 (1984)

111. V.P. Antropov, M.I. Katsnelson, and A.I. Liechtenstein, *Physica B: Cond. Matt.* **237-238**, 336 (1997)

112. V.P. Antropov, B.N. Harmon, and A.N. Smirnov, *JMMM* **200**, 148 (1999)

113. J.M. Ziman, '*Principles of the Theory of Solids'*, Cambridge University press, London (1969)

114. L. Nordstrom and D. Singh, *Phys. Rev. Lett.* **76**, 4420 (1996)

115. O. Ivanov and V. Antropov, *J. Appl. Phys*. **85**, 4821 (1999)

116. T. Oda, A. Pasquarello, and R. Carr, *Phys. Rev. Lett*. **80**, 3622 (1998)

117. V.Y. Irchin and M.I. Katsnelson, *Sov.Phys. Uspechi* **164**, 705 (1994)

118. A.I. Liechtenstein *et al.*, *J. Phys. F: Met. Phys*. **14**, L125 (1984)

119. V.P. Antropov, M.I. Katsnelson, B.N. Harmon, M. van Schilfgaarde, and D. Kusnezov, *Phys. Rev. B* **54**, 1019 (1996)

120. T. Valet and A. Fert, *Phys. Rev. B* **48**, 7099 (1993)

121. M.S. Hybertsen and S.G. Louie, *Phys. Rev. B* **34**, 5390 (1986)

122. T. Kotani, M. van Schilfgaarde, and S.V. Faleev, *Phys. Rev. B* **76**, 165106 (2007)

123. Lecture by M. van Schilfgaarde, *'GW Theory. Hand-on Course*'. Berlin, July 2014

124. M. van Schilfgaarde, T. Kotani, and S. Faleev, *Phys. Rev. Lett*. **96**, 226402 (2006)

125. M.S. Hyberstsen and S.G. Louie, *Phys. Rev B.* **34**, 5390 (1986)

126. S.V. Faleev, M. van Schilfgaarde, and T. Kotani, *Phys. Rev. Lett.* **93**, 126406 (2004)

127. D.R. Baraff, *Phys. Rev. B* **8**, 3439 (1973)

128. A.V. Gold, *J. Low Temp. Phys.* **16**, 3 (1974)

129. R.V. Coleman, W.H. Lowrey, and J.A. Polo Jr., *Phys. Rev. B* **23**, 2491 (1981)

130. R.V. Coleman, R.C. Morris, and D.J. Sellmyer, *Phys. Rev. B* **8**, 317 (1973)

131. G.G. Lonzarich, *'Electrons in Metals*', Cambridge University Press, Cambridge (1980)

132. J. Schäfer, M. Hoinkis, E. Rotenberg, P. Blaha, and R. Claessen, *Phys. Rev. B* **72**, 155115 (2005)

133. C. S. Wang and J. Callaway, *Phys. Rev. B* **15**, 298 (1977)

134. J. Sánchez-Barriga, J. Fink, V. Boni, I. Di Marco, J. Braun, J. Minár, A. Varykhalov, O. Rader, V. Bellini, F. Manghi, H. Ebert, M.I. Katsnelson, A.I. Lichtenstein, O. Eriksson, W. Eberhardt, and H.A. Dürr, *Phys. Rev. Lett*. **103**, 267203 (2009)

135. L. Sponza, P. Pisanti, A. Vishina, D. Pashov, C. Weber, M. van Schilfgaarde, S. Acharya, J. Vidal, and G. Kotliar, *Phys. Rev. B* **95**, 041112(R) (2017)

136. J.B. Pendry, *Surf. Science* **57**, 679 (1976)

137. R. Matzdorf, *Surf. Science Rep*. **30**, 153 (1998)

138. V.N. Strocov, *J. Elec. Spect. Rel. Phenomena* **130**, 65 (2003)

139. V.N. Strocov, R. Claessen, G. Nicolay, S. Hüfner, A. Kimura, A. Harasawa, S. Shin, A. Kakizaki, P.O. Nilsson, H.I. Starnberg, and P. Blaha, *Phys. Rev. Lett*. **81**, 4943 (1998)

140. P.J. Feibelman and D. E. Eastman, *Phys. Rev. B* **10**, 4932 (1974)

141. S. Tanuma, C. J. Powell, and D. R. Penn, *Surface and Interface Anal*. **21**, 165 (1994)

142. A.V. Gold, L. Hodges, P.T. Panousis, and D.R. Stone, *Int. J. of Magnetism* **2**, 357 (1971)

143. E. Lottini *et al*., *Chem. Mater*. **28** (12) 4214 (2016)

144. M. Pousthomis *et al*., *JMMM* **424**, 15 (2017)

145. E. Anagnostopoulou, *Nanoscale* **8**, 4020 (2016)

146. H.J.F. Jansen, *Phys. Rev. B* **59**, 4699 (1999)

147. O. Vekilova *et al*., Phys. Rev. B **99**, 024421 (2019)

148. M.N. Baibich *et al*., *Phys. Rev. Lett.* **61**, 2472 (1988)

149. T. Valet and A. Fert, *Phys. Rev. B* **48**, 7099 (1993)

150. J. Bass and W.P. Pratt, *J. Phys.: Condens. Matter* **19**, 183201 (2007).

151. H.Y.T. Nguyen, R. Loloee, W.P. Pratt, and J. Bass, *Phys. Rev. B* **86**, 064413 (2012)

152. D. Pashov, S. Acharya, W.R.L. Lambrecht, J. Jackson, K.D. Belashchenko, A. Chantis, F. Jamet, M. van Schilfgaarde *arXiv:1907.06021* (2019)

Appendix

Following the examiners' remarks Table 1 has been amended when revisiting the issue after the dissertation was completed. The differences between the values of magnetic and orbital moments for SR and FR cases were connected with the differences in implementation, not the true differences between SR and FR cases.

Two main problems were addressed:

- Parametrization of potential function *P*, in particular the way it includes SO coupling, was revisited by the authors of [152]; the details can be found in Section 2.16 of [152]. This problem is a shortcoming in the SR case, where the matrix form of the small parameter *p* (which turns the second order potential function into a third order one) is ignored. The FR treatment does not have this difficulty. It was found that adding the third order parametrization worsens the agreement between SR and FR cases, while the FR case compares well to SR band calculations of the spin and orbital moments
- Linearization energies were frozen to avoid the ambiguities in the boundary conditions. E_ν were taken from the SR case. In the SR case there are two E_ν for each *l* (for spin-up and spin-down). For

mapping these to the FR case the average of two $(E_{\nu 1} + E_{\nu 2})/2$ was taken to compare SR and FR values.

New values for some of the materials from Table 1 are given in Table 14 below. To evaluate the effect of the full Dirac equation we choose the simplest Hamiltonian to make SR and FR treatments as similar as possible. We use second order parameterization to avoid ambiguities in the spin orbit contribution to *p*, and single E_ν the different treatment of boundary conditions as noted above. SR and FR spin and orbital magnetic moments now differ by no more than a few percent.

Table 14 Spin and orbital magnetic moments (in μ_B) calculated with the Dirac solver compared to the scalar-relativistic method, including spin-orbit coupling.

Material	M_{Dirac}	M_{nonrel}	L_{Dirac}	L_{nonrel}
Ni	0.62779	0.63177	-0.05234	-0.05018
Fe	2.23931	2.22368	0.05175	0.04877
Co	1.58712	1.58402	0.07952	0.07579
FePt	3.22149	3.18960	Fe: 0.07316 Pt: 0.04862	Fe: 0.07177 Pt: 0.05158